Instituto Química Física Rocasolano
Statistical Mechanics and Condensed Matter Group

Reverse Monte Carlo modeling and Monte Carlo simulations of adsorption processes on zeolites

Vicente Sánchez Gil

A thesis presented for the degree of Doctor of Physics

PhD thesis under the supervision of:
Dr. Eva González Noya
Dr. José María Guil Pinto

Agradecimientos

Me gustaría agradecer en primer lugar a Eva G. Noya su inestimable ayuda para la realización de esta tesis. Su paciencia conmigo, su dedicación, su vocación docente. Por contagiar su entusiamo por la ciencia y por su trabajo no sólo a mí, sino también a todos los miembros del grupo. Por ser ejemplo de esfuerzo, ilusión y voluntad en tiempos de austeridad.

A José María Guil, imagen viviente de la vieja escuela, por enseñarme la dificultad que entraña conseguir unas buenas medidas experimentales.

Mención especial merece Enrique Lomba por su generosa tutela durante el primer año de mi doctorado. Por las fructíferas discusiones y los muchos consejos que a lo largo de estos más de cuatro años han ido surgiendo. Por su disponibilidad y cercanía para resolver todas mis preguntas.

A Noé G. Almarza por conjugar perfeccionismo y rigurosidad en todo lo que hace, alguien de quien aprender escuchando sus provechosas opiniones, siempre aliñadas con su característico sentido del humor.

También me gustaría agradecer a Cecilia Bores, compañera de fatigas, su disposición para ayudar siempre con una sonrisa, por facilitarme todo aquello en lo que ella ya sabía más que yo.

No me puedo olvidar de Claudio Martín, compañero de despacho hasta su jubilación, por responder a cada una de mis dudas cuando, recién llegado, los programas no hacían lo que les pedía.

Conjuntamente agradezco a mis tres mentores en mis estancias en el extranjero, Nigel Wilding, Marcia Barbosa y Laszlo Pusztai, por su amabilidad, su tiempo invertido en mí y su calurosa acogida.

Por último, no me gustaría acabar los agradecimientos sin mencionar a mi familia y amigos, destacando entre todos ellos, especialmente a Cuca.

List of publications

Publications considered in this thesis:

V. Sánchez-Gil, E.G. Noya, E. Lomba, *Reverse Monte Carlo modeling in confined systems*; J. Chem. Phys. **140**, 024504 (2014).

V. Sánchez-Gil, E. G. Noya, L. Temleitner and L. Pusztai, *Reverse Monte Carlo modelling: the two distinct routes of calculating the experimental structure factor*; J. of Mol. Liq. **207**, 211 (2015).

V. Sánchez-Gil, E. G. Noya, J. M. Guil, E. Lomba and S. Valencia, *Adsorption of argon on pure silica MEL. Volumetric experiments and grand canonical Monte Carlo simulations*; Micro. Meso. Mat. **222**, 218-225 (2016).

V. Sánchez-Gil, E. G. Noya, J. M. Guil, E. Lomba, S. Valencia, I. da Silva, L. Pusztai and L. Temleitner, *Evidences of a Structural Change in Pure-Silica MEL upon the Adsorption of Argon*; J. Phys. Chem. C (**submitted**).

V. Sánchez-Gil, E. G. Noya, A. Sanz, S.J. Khatib, J. M. Guil, E. Lomba, R. Marguta and S. Valencia, *Stepped adsorption of toluene on pure silica MEL zeolite*; J. Phys. Chem. C (**submitted**).

Others publications:

D. J. Ashton, V. Sánchez-Gil, N. B. Wilding, *Monte Carlo methods for estimating depletion potentials in highly size-asymmetrical hard sphere mixtures*; J. Chem. Phys. **139**, 144102 (2013).

E. Lomba, C. Bores, V. Sánchez-Gil, E. G. Noya, *A three dimensional integral equation approach for fluids under confinement: Argon in zeolites*; J. Chem. Phys. **143**, 164703 (2015).

Contents

Sinopsis

Las zeolitas son materiales porosos, ampliamente utilizados en la indsutria petroquímica, formados por redes de canales interconectados entre sí. Existen una gran variedad de zeolitas, tanto presentes en la naturaleza como sintetizadas artificialmente. De entre todas ellas, nuestro estudio se centra en la zeolita pura sílice MEL porque, pese a ser una zeolita estructuralmente bien caracterizada, no ha sido suficientemente estudiada. En la zeolita MFI, estructuralmente muy similar a la zeolita MEL, hay evidencias experimentales de que al adsorber diferentes moléculas en sus poros, aparecen uno o varios saltos en las isotermas volumétricas y calorimétricas cuya explicación y origen están lejos de ser conocidos [1, 2].

Con el objetivo de arrojar luz en el asunto, en la presente tesis se han estudiado en profundidad los procesos de adsorción en la zeolita MEL de dos tipos específicos de adsorbatos: átomos de argón y moléculas de tolueno. Para ello, se han combinado tanto medidas experimentales de adsorción, difracción de neutrones y rayos X, así como simulaciones computacionales Monte Carlo (MC) y Reverse Monte Carlo (RMC).

Primeramente, se han realizado experimentos de adsorción (calorimetría y volumetría) con la zeolita MEL, comprobando así que los saltos observados en la zeolita MFI también aparecen en las medidas de adsorción en la zeolita MEL. Para proporcionar una explicación microscópica del fenómeno, se han llevado a cabo dos estrategias conjuntas. La primera ha consistido en implementar simulaciones MC en la colectividad macrocanónica, considerando distintos modelos de potencial tanto para el argón [3] como para el tolueno [4] que describan su distribución espacial en los poros de la zeolita.

Por otro lado, se han medido los patrones de difracción para la adsorción de ambos adsorbatos con la intención de caracterizar la estructura del sistema antes y después del salto observado en la isoterma experimental. Para poder interpretar estas medidas de difracción, hemos desarrolado una variante del algoritmo RMC, denominado N-RMC, que sortea la dificultad que entraña la baja difusión de adsorbatos en medios de alto confinamiento, como el que se da en este tipo de zeolitas [5, 6]. Combinando las medidas de diffración con el nuevo algoritmo de simulación, hemos podido conocer en detalle la estructura de los adsorbatos compatible con los cambios observados en el espectro de difracción [7, 4].

Al utilizar ambas aproximaciones de forma conjunta, hemos podido realizar un estudio comparativo de los resultados obtenidos por medio de ambos métodos computacionales, pudiendo detectar pequeños cambios estructurales en la zeolita MEL que justifican, tanto el salto abrupto en la isoterma de adsorción, como la aparición de nuevos picos de diffracción.

Part I

Introduction

Zeolites

Zeolites are microporous materials made from interlinked alumina (AlO_4) and silica (SiO_4) tetrahedra . They form a three dimensional framework of interconnected channels and cavities where many different kind of molecules (adsorbates) can be adsorbed. Its crystalline character has made them attractive targets for the synthesis of new materials and potential use in a diverse set of applications. For example, they are widely used as catalysts in pharmaceutical drugs and in the petrochemical industry. There are more than 200 known types of zeolites, 40 naturally occurring, exhibiting many different crystalline structures and pore sizes. As they have very different pore sizes and shapes, they can also be used as shape-selective filters [8].

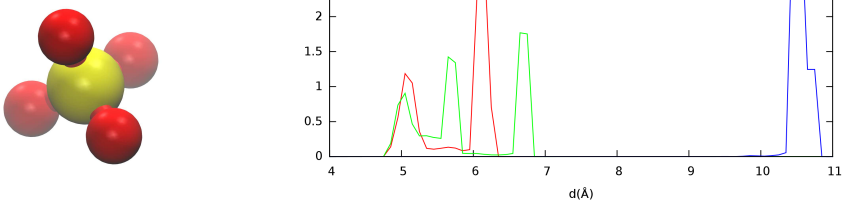

(a) (b)

Figure 1: a) SiO_4 tetrahedra, with four oxygen atoms (red) and the central silicon atom (yellow) in silicalite zeolites. b) Pore size distribution histogram for the three considered zeolites [9].

In this work, we have considered only silicalite type zeolites, this means that they are exclusively made from SiO_4 tetrahedral units, as shown in Fig. 1 a).

Despite this thesis is mainly focused on MEL zeolite framework, three different structures have been considered: MFI, MEL and FAU frameworks. Their unit cell parameter and characteristic values of their porous structure for the three crystals can be seen in Table 1. Figure 1 b) shows the pore size distribution for each of these zeolite types.

Table 1: Characteristic parameters for the three considered zeolites.

	MFI [10]	MEL [11]	FAU [12]
a (Å)	20.07	20.06	24.345
b (Å)	19.92	20.06	24.345
c (Å)	13.42	13.403	24.345
Pore limiting diameter (Å)	4.6	4.63	6.69
Maximum pore diameter (Å)	6.2	6.76	10.70
Accessible surface area (Å^2)	335.21	371.50	1740.48

MEL type zeolites ($I-4m2$ space group) present a 3D porous structure formed by the intersection of straight channels parallel to a and b axes, with a pore size diameter of about 5Å and intersections with a diameter of 6.76Å [11, 9]. The channel

on MEL, also known as ZSM-11 when some of the silicon atoms are replaced by aluminum active centers, are formed by 10-membered rings as shown in Fig. 2 (a).

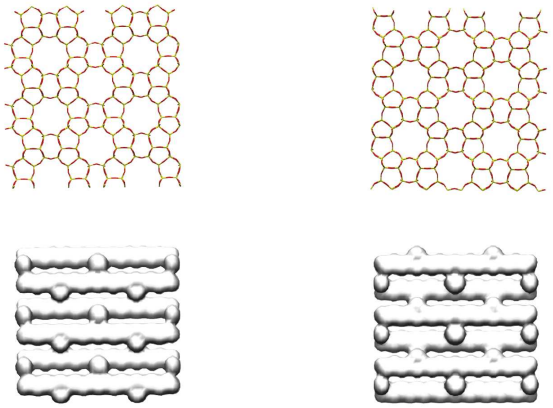

(a)

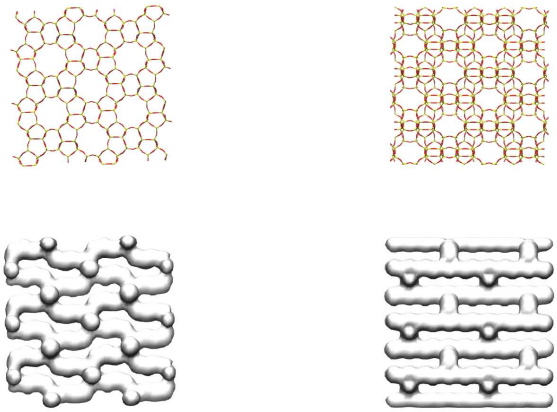

(b)

Figure 2: Structure of a) MEL , b) MFI zeolites. The two top figures show two different views of the zeolite atomic structures. The two bottom figures show the volume accessible to the adsorbates (calculated using the argon atomic diameter).

MFI zeolite, also known as ZSM-5 when some of the silicon atoms are replaced by aluminum active centers, has been considered because it is structurally very similar to MEL zeolite and its adsorption properties are much better characterized than those of MEL, providing a guidance to the study of adsorption on MEL. In contrast to MEL, MFI 3D porous network is formed by the intersection of straight an sinusoidal channels (see Fig. 2 (b)) [10]. The estimated pore size of its channels is between 4.7Å and 6.36Å for the inner cavities [12].

Finally, FAU zeolite presents relatively large pores and cavities in comparison to MFI and MEL with diameters of about 10.5Å respectively [9]. Hence, it has been used to study the effect of different levels of confinement, tight for MEL and MFI zeolites and not so tight for FAU. The faujasite framework (see Fig. 3 (c)) has $Fd3m$ space group and consists of sodalite cages connected through hexagonal prisms.

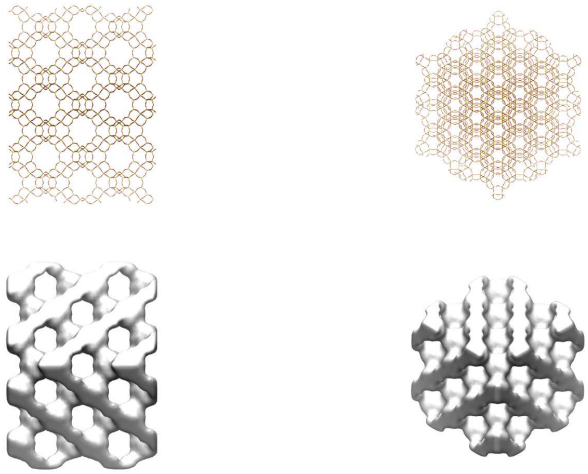

Figure 3: Structure of FAU zeolite. The two top panels show two different views of the MEL atom structure. The two bottom panel show the volume accessible to the adsorbates.

Motivations

For simple gases, such as argon, krypton and nitrogen adsorption on MFI zeolite it was observed a sub-step in their corresponding experimental adsorption isotherms (see Fig. 4). Some authors attribute this sub-step to a structural change of the zeolite framework and others to a phase transition of the adsorbate from a fluid-like to a solid-like phase [1, 2]. In addition to that, their corresponding isosteric heats of adsorption are extremely different as can be seen in Fig . 4. Despite this problem has been studied for decades, a definitive explanation of the origin of sub-steps in the adsorption has not been provided yet.

On the other hand, there are experimental evidences of structural changes in zeolites when the temperature increases or molecules are adsorbed. For example, MFI zeolite is orthorhombic and its space group is $Pnma$ [14] at high temperatures (ORTHO), but a reversible phase transition to the monoclinic space group $P2_1/n.1.13$ occurs at 380 K (MONO) [15]. A new configuration, called PARA, has been also observed, which exhibits a space group $P2_12_12_1$, when p-xylene is adsorbed [16]. Therefore, there could be a relation between the experimental sub-step and a structural change of the zeolite framework.

The aim of this work is to study the adsorption behavior on MEL zeolite that it is structurally similar to MFI but somewhat simpler. The adsorption properties of this relatively new zeolite have not been deeply investigated yet, and given its structural simplicity, it can be a good starting point for unraveling the adsorption of simple molecules in MFI and MEL zeolites.

With this general objective in mind, we have studied the adsorption of two representative molecules: argon (as example of a simple gas) and toluene (as example of an aromatic molecule) in pure silica MEL zeolite. Adsorption of the two different adsorbates has been studied by means of volumetric and calorimetric, neutron and X-rays diffraction measurements, as well as Monte Carlo (MC) and Reverse Monte Carlo (RMC) simulations.

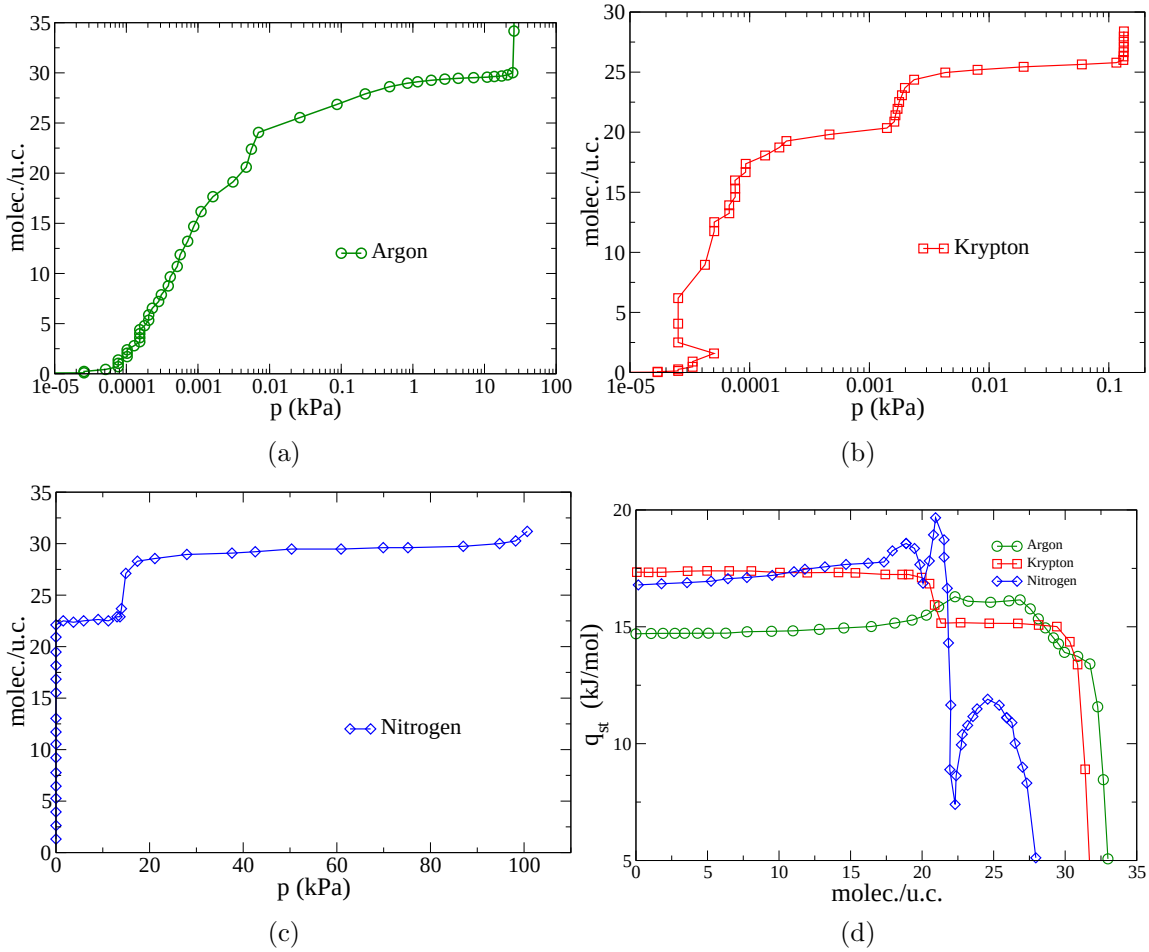

Figure 4: Experimental adsorption isotherms of (a) argon [this work], (b) krypton [this work] and (c) Nitrogen [13] in pure silica MFI. In the bottom right corner, their isosteric heats of adsorption are shown [1, 2].

Firstly, looking for a mathematical expression for estimating the experimental diffracted peaks intensities for an adsorption process, we have compared the effect of using two different routes for the structure factor calculation and their application limits for systems of increasing order and complexity [6].

Secondly, we have developed a new extension of the well established Reverse Monte Carlo method which deals more efficiently than the usual implementation with adsorbates under tight confinement [5]. The method was tested using as target an structure factor provided by a GCMC simulation, obtaining a good agreement on the microscopic structure up to the level of three-body correlations.

Once we tested the N-RMC extension with a model system, we applied it to real experimental diffraction data, concretely, time of flight neutron and powder X-rays diffraction measurements for argon and toluene adsorption on pure silica MEL, respectively.

At the same time, Monte Carlo simulations in the grand canonical ensemble (GCMC) have also been implemented using different potential models. The advantage of molecular simulations is that they provide detailed information of the microscopic structure of the system, but it depends on the goodness of the model potentials used to describe the interactions in the system. This way, a complete

study of the adsorption processes on MEL can be done to shed light on this matter.

This thesis consists of experimental measurements and computer simulations. In both parts, the PhD candidate took an active part. The PhD candidate participated in the diffraction measurements performed at ISIS spallation facilities and at ALBA synchrotron. Apart from the sample preparation, done by Dr. J.M. Guil, the diffraction data were collected by him in collaboration with Dr. Eva G. Noya and A. Sanz Parra.

Regarding computational simulations, all GCMC and RMC simulations have been performed using home-made programming codes written by Dr. Eva G. Noya and the PhD candidate Additionally, a home-made parallel code written in CUDA programming language has been developed by the PhD student in collaboration with Dr. E. Lomba.

Part II

Theory and simulations

Chapter 1

Monte Carlo modeling

1.1 Monte Carlo method

Monte Carlo is a computational algorithm based on the use of random numbers for generating configurations compatibles with a given statistical ensemble.

From a given initial state α, Monte Carlo method consists of generating a chain of configurations, called Markov chain, according to Boltzmann distribution probability. The transition probability from that initial state α to a final state β, denoted as $\pi(\alpha \to \beta)$, is mathematically described by

$$\pi(\alpha \to \beta) = \rho(\alpha) a(\alpha \to \beta) P_{acc}(\alpha \to \beta) \tag{1.1}$$

where $\rho(\alpha)$ is the probability of finding the system at α state, $a(\alpha \to \beta)$ is the element of the transition matrix that correspond to the probability of generating a configuration β from α state and $P_{acc}(\alpha \to \beta)$ is the acceptance probability of this proposed random transition.

For doing that, once the equilibrium of the system is reached, Markov chain does not leave it, microscopic reversibility must be fulfilled. Assuming this microscopic reversibility, the Markov chain follows the so called *detailed balance*: at equilibrium, each elementary process is equilibrated by its reverse process. For a given transition between two different states α and β *detailed balance* is simply defined as

$$\pi(\alpha \to \beta) = \pi(\beta \to \alpha). \tag{1.2}$$

As was proposed by Metropolis *et al.* [17], if we assume that the transition matrix a is symmetric, it can be deduced the ratio of the acceptance probabilities for a given transition $\alpha \to \beta$ which according to Eq. 1.1 satisfies

$$\frac{P_{acc}(\alpha \to \beta)}{P_{acc}(\beta \to \alpha)} = \frac{\rho(\beta)}{\rho(\alpha)} \tag{1.3}$$

From all possible solutions that fulfill the Eq. 1.3, the Metropolis Monte Carlo algorithm [17] yields a very efficient acceptance criteria for generating a sequence of random states that follow the Boltzmann distribution probability, defined by

$$P_{acc}(\alpha \to \beta) = min\left[1, \frac{\rho(\beta)}{\rho(\alpha)}\right] \tag{1.4}$$

where $P_{acc}(\alpha \rightarrow \beta)$ is the acceptance probability for the proposed transition $\alpha \rightarrow \beta$ and $\rho(\beta)/\rho(\alpha)$ is the ratio between probability densities of α and β states in a given ensemble.

The canonical ensemble (NVT), represents a system in thermal equilibrium with a heat bath. In this ensemble the number of particles N, volume V and temperature T are constant. The statistical properties of the system are mathematically described by the canonical partition function $Z(N, V, T)$, which is given by

$$Z(N, V, T) = \frac{1}{\Lambda^{3N} N!} \int dr^N e^{-\beta U(r^N)} \tag{1.5}$$

and the probability density of finding configuration r^N is proportional to

$$\rho(r^N) \propto e^{-\beta U(r^N)}. \tag{1.6}$$

where $\beta = 1/k_B T$ is the thermodynamic beta , $\Lambda = \sqrt{h^2/(2\pi m k_B T)}$ is the thermal de Broglie wavelength and $U(r^N)$ is the total energy for a given set of coordinates r^N.

Therefore, according to Eq. 1.4, the acceptance probability for a randomly chosen translation of a particle in the canonical ensemble is defined as

$$P_{acc}(\alpha \rightarrow \beta) = min\left[1, e^{-\beta \Delta U}\right]. \tag{1.7}$$

where ΔU is the energy difference after and before the translation trial.

From a practical point of view, the Metropolis Monte Carlo algorithm is implemented as follows:

1) A random move is proposed from state α to state β. To do this, a randomly chosen particle is translated to a new position applying a random displacement.

2) The energy difference, ΔU, between the current α state and the proposed state β is evaluated.

3) If $U(\beta) < U(\alpha)$, the move automatically is accepted. Otherwise, the acceptance probability for the proposed movement, $P_{acc}(\alpha \rightarrow \beta)$, is compared with a random number $\epsilon \in (0, 1)$. Only if $\epsilon < P_{acc}(\alpha \rightarrow \beta)$ the move is accepted.

Note that, although the equilibrium properties sampled by MC correspond to the real equilibrium properties of the system, Monte Carlo method does not mimic the real dynamics of the system. Following the above described procedure, the Metropolis sampling method implies that the estimation of the mean value of a given thermodynamic property A , namely $\langle A \rangle$, can be written as the simple arithmetic mean of the numerical values of each observation A_i divided by the total number of observations M

$$\langle A \rangle = \frac{1}{M} \sum_{i=1}^{M} A_i. \tag{1.8}$$

1.1.1 Grand canonical Monte Carlo

The grand canonical ensemble describes a constant-volume system (V) that can exchange both heat and particles with a reservoir at temperature T and chemical potential μ. This is the most suitable ensemble for simulating an adsorption process

because the system can exchange energy and particles with a reservoir of adsorbates at temperature T. Thus, particles can access narrow pores without facing diffusion problems.

For a system in thermal and chemical equilibrium with an external reservoir, the partition function is given by [18]

$$Z(\mu, V, T) = \sum_{N=0}^{\infty} \frac{e^{\beta\mu N} V^N}{\Lambda^{3N} N!} \int dr^N e^{-\beta U(r^N)} \tag{1.9}$$

where μ, V, T are the three fixed thermodynamic variables in grand canonical ensemble, $\Lambda = \sqrt{h^2/(2\pi m k_B T)}$ is the thermal de Broglie wavelength and r^N is the set of coordinates for the N particles in the simulation box. Hence, the corresponding probability density is proportional to

$$\rho(r^N; N) \propto \frac{e^{\beta\mu N} V^N}{\Lambda^{3N} N!} e^{-\beta U(r^N)}. \tag{1.10}$$

There are three different movements in grand canonical ensemble: insertions, deletions and translations trials. For an insertion of a particle in a randomly chosen position, the acceptance probability is given by the ratio between the probability densities from state N to $N+1$, according to Eq. 1.3

$$P_{acc}(N \to N+1) = \frac{V}{\Lambda^3 (N+1)} e^{\beta\mu} e^{-\beta(U_{N+1} - U_N)} \tag{1.11}$$

where $U_{N+1} - U_N$ is the total energy difference after and before the insertion trial.

In the same way, the acceptance probability for a deletion of a randomly chosen particle is given by the probability density quotient of N and $N-1$ states

$$P_{acc}(N \to N-1) = \frac{\Lambda^3 N}{V} e^{-\beta\mu} e^{-\beta(U_{N-1} - U_N)} \tag{1.12}$$

where $U_{N-1} - U_N$ is the total energy difference after and before the proposed deletion attempt.

Lastly, for a particle i translation from r_i to a randomly chosen position $r_i + \Delta r$, where the number of particles in the simulation box remains constant as in canonical ensemble, the acceptance probability can also be estimated from the ratio between the Boltzmann factors

$$P_{acc}(r_i \to r_i + \Delta r) = e^{-\beta \Delta U} \tag{1.13}$$

where ΔU is the total energy difference between the current position r_i and the proposed position $r_i + \Delta r$ as in Eq. 1.7.

1.1.2 Potential energy functions

The potential energy calculation for a given set of coordinates is a essential part in a Monte Carlo simulation and it is usually the most computationally demanding part. The energy difference ΔU for a proposed transition $\alpha \to \beta$ can be evaluated using model potential energy functions. These functions, offenly calibrated to experimental results and quantum mechanical calculations, reproduce physical properties measurable by experiments. Although results obtained with potential energy

functions are approximate, they provide a reasonably good compromise between accuracy and computational efficiency.

In general, a potential energy function of N interacting particles can be calculated as follows

$$U(r) = \sum_i u_1(r_i) + \sum_i \sum_{j>i} u_2(r_i, r_j) + \sum_i \sum_{j>i} \sum_{k>j>i} u_3(r_i, r_j, r_k) + ... \tag{1.14}$$

where u_1 represents the effect of an external force field and u_2 and u_3 are the two- and three-body correlations energy terms respectively.

A large number of potential functional forms are available in literature for modeling many different systems. Details of the potential models used in this thesis are given in section 1.3.

1.2 Implementation details

In this section, some relevant computational tricks used for a system under tight confinement are briefly described. These improvements applied to the GCMC simulations increase substantially the efficiency of the method.

1.2.1 PBC and MIC

For all simulations performed in this thesis, periodic boundary conditions (PBC) and minimum image convention (MIC) have been used.

Periodic boundary conditions [18], an extended computational trick, are used for having a closer representation of a real macroscopic system without using an extremely large simulation box. As illustrated in Fig. 1.1, when using periodic boundary conditions, the simulation box is replicated throughout space to form an infinite three-dimensional lattice. Then, when a particle crosses the right boundary, it is automatically replaced by a particle entering the left (and vice versa). This way, the total number of particles in all identical boxes is always conserved and the undesirable surface effects are avoided.

Simultaneously, when PBC are applied to a system the minimum image distance convention is also typically used. This convention implies that for each particle of the system, we only consider the shortest distance between the given particle and any of the remaining infinite particle replicas [19, 18].

1.2.2 Cells and linked list

For short range potentials, the interaction between two particles becomes smaller when the distance between them increases. As a consequence, a limited distance range determined by the cutoff distance r_{cutoff}, is considered in simulations. This means that for a central particle only the particles within a sphere of radius $r = r_{cutoff}$ contribute to the global potential energy and obviously the effect of the remaining particles can be neglected or incorporated approximately through long-range corrections. This means that, in order to evaluate the energy of a given particle, we do not need to calculate the distance to all the particles of the system.

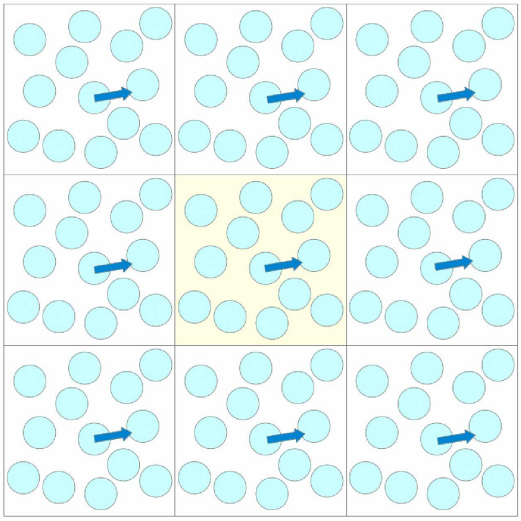

Figure 1.1: Schematic two-dimensional representation of periodic boundary conditions.

It is enough to calculate it to those that are likely to be within the interaction range of the central particle.

For large systems (the typical number of particles in the GCMC simulation box in this thesis is about ∼4000 atoms), an important efficiency improvement can be done dividing the simulation box into a regular lattice of cubic cells of side $l_{cell} \geq r_{cutoff}$. Thus, for a given central particle i, only the distances between i and any j neighboring particles within the same cell and its 26 neighbor cells are calculated. Therefore, many time consuming distance evaluations can be avoided [18].

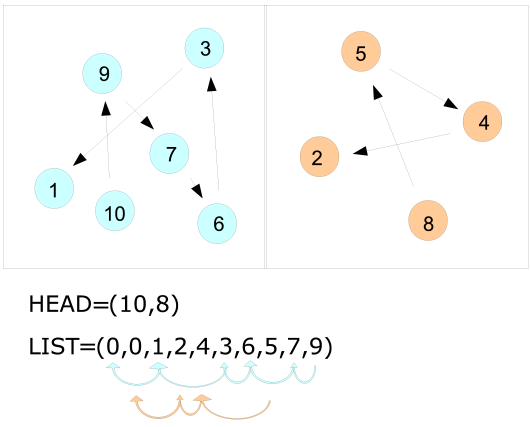

Figure 1.2: Schematic representation of linked list algorithm for a two cells system. The corresponding HEAD and LIST arrays are shown below.

A second enhancement also implemented in the GCMC program code is the

linked list algorithm [19]. As can be seen in Fig. 1.2, two different arrays are continuously updated along the simulation. The first one, called HEAD, holds the index of the first atom for each cell. The second one, called LIST, contains the 'link' to the next atom in that cell, in other words, the atom index to which the i-th atom points. Following the indices in LIST array, we track all atoms in the cell. When the last atom index in a given cell is read, a zero is written in LIST. Then we move to the next element in the HEAD array to explore the next cell and so on until all neighbors cells are tracked. In contrast to a conventional list cell, the linked list algorithm deals more efficiently with insertions or deletions of elements in the list due to the fact that data are not stored contiguously on disk.

1.2.3 Energy interpolation

In all GCMC simulations with a rigid zeolite framework, the energy contribution of the adsorbate-zeolite term has been interpolated using the energy values of a three dimensional cubic lattice of side $\Delta x = \Delta y = \Delta z = 0.08$Å.

Thus, we calculated the adsorbate-zeolite term only at the start of the simulation and for every movement attempt, the energy is just evaluated by means a trilinear interpolation. The adsorbate-zeolite contribution at one given position, illustrated in Fig. 1.3, is calculated from the energy values of the closest eight points on the surrounding cube.

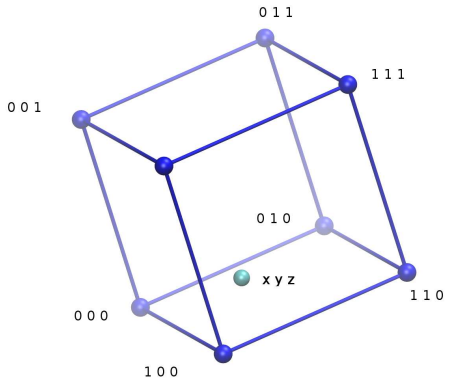

Figure 1.3: Graphical representation and notation used for the eight points on the surrounding cube and the position of interest. The i j k indices correspond to the x_i, y_j and z_k positions.

First of all, we define three new coordinates using the eight corners on the surrounding cube

$$\begin{aligned} x_d &= (x - x_0)/(x_1 - x_0) \\ y_d &= (y - y_0)/(y_1 - y_0) \\ z_d &= (z - z_0)/(z_1 - z_0) \end{aligned} \tag{1.15}$$

where x_0 and x_1 are the closest lattice points below and above x respectively (same for y and z axis).

Secondly, we interpolate along the x-axis

$$\begin{aligned} c_{00} &= U(x_0, y_0, z_0)(1 - x_d) + U(x_1, y_0, z_0)x_d \\ c_{10} &= U(x_0, y_1, z_0)(1 - x_d) + U(x_1, y_1, z_0)x_d \\ c_{01} &= U(x_0, y_0, z_1)(1 - x_d) + U(x_1, y_0, z_1)x_d \\ c_{11} &= U(x_0, y_1, z_1)(1 - x_d) + U(x_1, y_1, z_1)x_d \end{aligned} \tag{1.16}$$

where $U(x_0, y_0, z_0)$ is the energy value stored at lattice point (x_0, y_0, z_0).
Afterward, we interpolate these values along the y-axis

$$\begin{aligned} c_0 &= c_{00}(1 - y_d) + c_{10}y_d \\ c_1 &= c_{01}(1 - y_d) + c_{11}y_d \end{aligned} \tag{1.17}$$

Finally, the interpolated energy at point (x, y, z), $U(x, y, z)$ can be calculated from the linear interpolation along z-axis

$$U(x, y, z) = c_0(1 - z_d) + c_1 z_d \tag{1.18}$$

1.2.4 Biased insertion

For systems with particles under tight confinement, where most of the simulation box is occupied by the porous material atoms, an important efficiency improvement can be done via biased insertion. First of all, before starting the GCMC simulation, we divide the simulation box in a three-dimensional grid. Then we calculate the accessible volume, V_{acc} according to [20]

$$V_{acc} = V \frac{N_{acc}}{N_{total}} \tag{1.19}$$

where V is the volume of the simulation box and N_{acc}/N_{total} is the ratio between the number of accessible points, in which the test particle do not overlap with any atom of the microporous material, and the total number of points of the three-dimensional grid.

According to this, we only try insertions in those accessible positions in which adsorbates do not overlap with the zeolite framework. Hence, the total volume of the simulation box, V, in the insertion and the deletion acceptance probability must be replaced by the calculated accessible volume V_{acc} (see Eq. 1.11 and 1.12) [19, 18]

$$P_{acc}(N \to N + 1) = \frac{V_{acc}}{\Lambda^3(N + 1)} e^{\beta\mu} e^{-\beta(U_{N+1} - U_N)} \tag{1.20}$$

$$P_{acc}(N \to N - 1) = \frac{\Lambda^3 N}{V_{acc}} e^{-\beta\mu} e^{-\beta(U_{N-1} - U_N)} \tag{1.21}$$

This way, we do not attempt insertions in places occupied by the zeolite framework and, consequently, the computational time to reach equilibration is considerably reduced.

	ϵ/k_B (K)	σ (Å)
Ar-Ar	124.07	3.380
Ar-O	114.81	3.1265

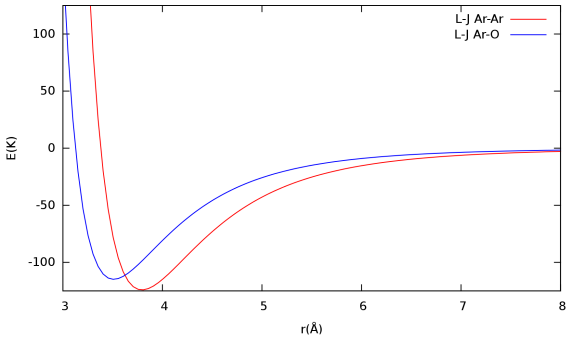

Table 1.1: Lennard-Jones parameters used for the argon adsorption in the pure silica MEL zeolite [21]. In the right hand side, the graphical representation of the two components of Lennard-Jones potential are shown.

1.3 Potential models

1.3.1 Adsorbate-Adsorbate and Adsorbate-Zeolite interactions

Once the Monte Carlo method has been briefly depicted, the potential models used to mimic the interactions between the atoms involved in the adsorption process are described in this section.

Argon adsorption in pure silica MEL

Lennard-Jones potential has been widely used for modeling noble gases, as argon, neon or krypton, as well as simple gases as methane. Thus, adsorbate-adsorbate and adsorbate-zeolite interactions for argon adsorption in pure silica MEL are modeled by an atom-atom Lennard-Jones potential (L-J) which is defined by:

$$U_{LJ}(r_{ij}) = 4\epsilon \left[\left(\frac{\sigma}{r_{ij}} \right)^{12} - \left(\frac{\sigma}{r_{ij}} \right)^{6} \right] \tag{1.22}$$

where ϵ is the depth of the potential well, σ is the distance at which the L-J potential is equal to zero and r_{ij} is simply the distance between two given particles i and j.

If charges are not taken in account, silicon atoms can be effectively considered because their contribution is screened by the four surrounding oxygen neighbors which form the tetrahedral unit (see Fig. 1) and their effect is included in the adsorbate-oxygen interaction [20]. Whereas the Ar-O Lennard-Jones parameters have been chosen to fit the experimental adsorption isotherm at low pressures, the parameters for the Ar-Ar interaction, taken from Ref. [21], were fitted to the experimental liquid-vapour curve. In table 1.1, L-J parameters, ϵ and σ, used in GCMC simulations and a graphical representation the Ar-Ar and Ar-O interactions are shown. Both L-J potentials are truncated and shifted at $r_{cutoff} = 12$Å.

	ϵ/k_B (K)	σ (Å)	q (e)
C	35.247	3.550	-0.115
CH_3	85.599	3.800	0.115
H	15.106	2.420	0.115
C-O	73.553	3.007	-
CH_3-O	80.317	3.364	-
H-O	49.056	2.604	-

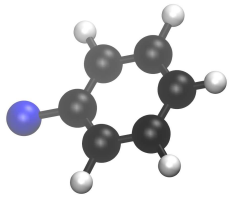

Table 1.2: Lennard-Jones parameters and electrostactic charges used for the toluene adsorption in the pure silica MEL zeolite [21]. In the right hand side, the geometry of the toluene potential model is shown.

Toluene adsorption on pure silica MEL

Electrostatic charges play and important role in the asorption process on zeolites of polyatomic molecules as toluene. Therefore, in the case of the toluene adsorption, the potential model consist of a Lennard-Jones potential, similarly to argon adsorption, and a coulombic potential that takes in account the electrical charges of the adsorbate+zeolite system. Thus, the total energy is given by

$$U_{total} = U_{L-J} + U_{Coulomb} \tag{1.23}$$

where U_{L-J} is the Lennard Jones interaction between toluene-toluene and toluene-zeolite atoms taken from references [22] and [23], respectively. As mentioned above, silicon atoms can be effectively considered for the L-J potential because their contribution is screened by the four surrounding oxygen atoms. The Lennard-Jones parameters used for toluene adsorption are tabulated in Table 1.2. The second term in Eq. 1.23, denotes the non-bonded coulombic potential between all pair of atoms ij of the system

$$U_{Coulomb}(r) = \frac{1}{4\pi}\frac{q_i q_j}{\epsilon_o r} \tag{1.24}$$

where ϵ_o is the vacuum permittivity of the material and q_i and q_i are the electric charges of atoms i and j, respectively.

For this term, all silicon atoms (with an charge of $+2e$) and oxygen atoms (with a charge of -1e) are considered for the total electrostatic energy calculation. Electric charges of the the atoms of toluene and its geometry are shown in Table 1.2. Finally, it is important to note that as the coulombic potential is a long-range interaction, Ewald summs are applied to estimate the electrostatic interactions using a finite simulation box (see appendix A).

1.3.2 Zeolite-Zeolite interactions

As mentioned before in the introduction, the adsorption isotherm of argon adsorption exhibits a sub-step on MEL and MFI zeolites (see Fig. 4) that can be attributed to a structural change of the adsorbent or a fluid-like to a solid-like transition of the adsorbate [16]. Furthermore, it has been observed that under tight confinement, some adsorbates can induce changes in the zeolite framework.

For this reasons, despite most of the simulations have been performed considering a non-interacting rigid zeolite, two different potentials have been also chosen to describe the flexibility of the zeolite framework. Both of them reproduce reasonably well the experimental IR spectrum of several siliceous zeolites, including MEL[24]. Firstly, we have considered a flexible model for the zeolite framework, proposed by Demontis *et al.* [25], an atom-atom potential energy in which only bond *Si-O* and bend *O-Si-O* interactions are taken in account. The second potential model, proposed by Nicholas *et al.* [26], includes bond, bend and dihedral terms as well as non-bonded Lennard Jones and electrostatic interactions.

Demontis potential

The first potential model, proposed by Demontis *et al.* [25], only includes bonding terms between *O-Si* atoms and also between the four oxygen atoms that belong to the same tetrahedra (see Fig. 1), that we will designate as *O-(Si)-O*.

The potential energy, expanded around the equilibrium bond distance r_0 in a power series up to third order, is defined as

$$U(r) = U_0 + \frac{1}{2}k_1(r - r_0)^2 + \frac{k_2}{6}(r - r_0)^6 \tag{1.25}$$

where U_0, k_1 and k_2 are three bond energy constants.

The Demontis potential, as published in Ref.[25], has been slightly modified, so that experimental MEL structure is an energy minimum by construction. This means, that instead of using a constant value for equilibrium distance r_0, we use a different value for each *Si-O* bond taken from the experimental structure provided by Terasaki *et al.* [11]. The Demontis modified potential parameters for a flexible zeolite framework are shown in table 1.3.

Table 1.3: Demontis modified potential constants used for the flexible MEL zeolite framework [25].

bond	U_0(kcal/mol)	k_1(kcal/mol)	k_2(kcal/mol)	r_0 (Å)
Si-O	-95.0	500.0	-936.586	1.565-1.623
O-(Si)-O	-5.844	100.0	-337.758	2.563-2.655

Nicholas potential

The second force field considered to model the flexibility of the MEL zeolite framework, developed by Nicholas *et al.* [26], is more sophisticated in comparison with the Demontis one described above. The total potential energy for the Nicholas model includes different terms that tune bond stretches, angle bends and torsion angles (bonded interactions) as well as Lennard-Jones and electrostatic interactions (non-bonded interactions) [26].

$$U_{total} = U_{bond} + U_{angles} + U_{torsion} + U_{Si-Si} + U_{L-J} + U_{Coulomb} \tag{1.26}$$

The first term in Eq. 1.26 U_{bond}, the *Si-O* bond interaction in the zeolite framework is simply described by a harmonic oscillator

$$U_{bond}(r) = \frac{1}{2}k_{bond}(r - r_0)^2 \tag{1.27}$$

where r is the distance between two bonded *Si-O* atoms, k_{bond} is the bonding energy term and r_0 is the equilibrium distance for those *Si-O* atoms in the experimental sample.

The second term in Eq. 1.26, U_{angles}, holds two different contributions

$$U_{angles} = U_{O-Si-O}(\theta) + U_{Si-O-Si}(\theta) \tag{1.28}$$

The angle formed by a central silicon atom and two of the four surrounding oxygen atoms of a tetrahedra, named *O-Si-O* , is tuned by harmonic oscillators according to

$$U_{O-Si-O}(\theta) = \frac{1}{2}k_\theta(\theta - \theta_0)^2 \tag{1.29}$$

where θ is the angle formed by a central silicon atom and two oxygen atoms that belong to the same tetrahedra, k_θ is the angular energy constant and θ_0 is the equilibrium angle.

For the second angular contribution, also a energy constraint is added to the angles formed by the four closest tetrahedral units (see Fig. 1). This energy term, named $U_{Si-O-Si}$, is defined by an expansion in a power series around equilibrium angles up to the fourth order

$$U_{Si-O-Si}(\theta) = \frac{1}{2}k_{\theta1}(\theta - \theta_0)^2 + \frac{1}{2}k_{\theta2}(\theta - \theta_0)^3 + \frac{1}{2}k_{\theta3}(\theta - \theta_0)^4 \tag{1.30}$$

where θ is the angle formed by the a central oxygen atom and the two closest neighbors silicon atoms, θ_0 is the equilibrium angle and $k_{\theta1}$, $k_{\theta2}$ and $k_{\theta3}$ are the three angular energy constants, respectively.

The torsional term considered by Nicholas potential, measures the coupling between *Si-O-Si-O* torsional and *Si-O-Si* angular interaction. The potential for the *Si-O-Si-O* dihedral angles is given by

$$U(\Phi) = \frac{1}{2}k_\Phi(1 + cos(3\Phi)) \tag{1.31}$$

where Φ is the dihedral angle formed by these four atoms and k_Φ is the torsional energy constant.

When *Si-O-Si* angle becomes linear, the dihedral angle containing the linear angle would not be uniquely defined, resulting in a discontinuity in the torsional energy term. This discontinuity is avoided by means of a switching function, $S(\theta)$, so that the torsional energy goes smoothly to zero as the *Si-O-Si* bond is linear. Hence, the switching function is mathematically defined as

$$\begin{cases} S(\theta) = \frac{(\theta_{off}-\theta)^2(\theta_{off}+2\theta-3\theta_{on})}{(\theta_{off}-\theta_{on})^3} \text{ if } 170^\circ \leq \theta \leq 180^\circ \\ \\ S(\theta) = 1 \text{ if } \theta < 170^\circ \end{cases} \tag{1.32}$$

where $\theta_{on} = 170^\circ$ and $\theta_{off} = 180^\circ$ and θ is the angle formed by the *Si-O-Si* bonded atoms.

Thus, the torsional energy is just the product of the dihedral energy $U(\Phi)$ and the calculated switching function, $S(\theta)$

$$U_{torsion}(\Phi,\theta) = U(\Phi)S(\theta). \tag{1.33}$$

Those silicon atoms belonging to two adjoining tetrahedra also interact via a harmonic oscillator U_{Si-Si}, which depends on the distance between these non-bonded silicon atoms r_{Si-Si}

$$U_{Si-Si}(r) = \frac{1}{2}k_{Si-Si}(r_{Si-Si} - r_0)^2 \tag{1.34}$$

where k_{Si-Si} is the energy constant and r_0 the equilibrium distance.

In addition to bond stretches and bend/torsional terms, a Lennard-Jones potential (see Section 1.3.1) is also implemented for describing non bonded interactions

$$U_{LJ}(r) = 4\epsilon\left[\left(\frac{\sigma}{r}\right)^{12} - \left(\frac{\sigma}{r}\right)^{6}\right] \tag{1.35}$$

Finally, non-bonded electrostatic interactions are modelled by a Coulomb potential according to Eq. 1.24. Electrostatic and L-J interactions are truncated at r_{cutoff}=8.85Å. For computing the long range contribution to the Coulombic potential, Ewald sums have been used. A detailed description of the Ewald summation method is written in appendix A. The different parameters used for the Nicholas modified potential, shown in Tables 1.5 and 1.4. In the same way as we did with the Demontis force field, the standard Nicholas potential has been also modified. In this case, not only the equilibrium distances, but also the equilibrium angles have been taken from the experimental structure provided by Terasaki *et al.* [11].

Table 1.4: Nicholas modified parameters used for the flexible MEL zeolite. Only the Lennard Jones parameters and the electric charges for the electrostatic interaction are shown.

	ϵ/k_B (K)	σ (Å)	q (e)
Si-Si	81.83	3.962	1.1
O-O	29.43	3.06	-0.55

Table 1.5: Nicholas modified parameters used for the flexible MEL zeolite [26]. Only the bond, bend and torsional interaction are shown.

Component	Energy constant	Equilibrium distance/angle
Si-O	k_{bond}= 597.32 $(kcal/mol\text{Å}^2)$	r_0=1.565-1.623 (Å)
O-Si-O	k_θ= 138.12 $(kcal/mol\,\mathrm{deg.}^2)$	θ_0=106.3-112.7 $(deg.)$
Si-O-Si	$k_{\theta 1}$=10.85^a ; $k_{\theta 2}$=22.72^b ; $k_{\theta 3}$=13.26^c	θ_0=144.9-172.5 $(deg.)$
Si-(O)-Si	k_{Si-Si}=54.6 $(kcal/mol\text{Å}^2)$	r_0=3.033-3.164 (Å)
Si-O-Si-O	k_Φ=-0.70 $(kcal/mol)$	-

$^a(kcal/mol\,\mathrm{deg.}^2)$ $^b(kcal/mol\,\mathrm{deg.}^4)$ $^c(kcal/mol\,\mathrm{deg.}^6)$

1.4 Properties calculation

The set of the equilibrium spacial coordinates provided by grand canonical Monte Carlo simulations can be studied by means of some properties of interest as the pair and bond angle distribution functions. In this section, the calculation and physical meaning of both functions are shortly described. Furthermore, as pressure and isosteric heat of adsorption are the two macroscopic variables measured in volumetric and calorimetric isotherms, the procedure to calculate them from the simulated data is also reported in this section.

1.4.1 Pair distribution function

Partial distribution functions (PDF) can provide useful information about the structure of adsorbates inside the zeolite channels and cavities. The PDF describes density variations, within a given spherical shell, as a function of distance from a reference particle (see Fig. 1.4).

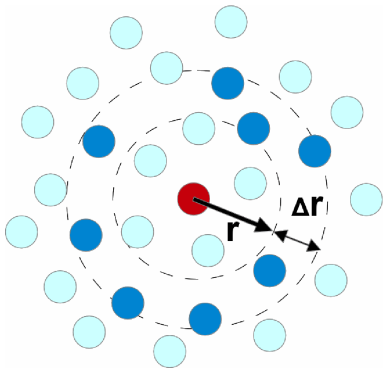

Figure 1.4: Schematic drawing of the system. Only the particles at a distance between r and $r + \Delta r$ (blue) from a reference particle (red) are considered for the $g(r+\Delta r)$ calculation. The remaining particles (cyan) do not contribute to its value.

Mathematically, the partial distribution function, $g(r)$ is defined as:

$$g_{\alpha\beta}(r) = \frac{n_{\alpha\beta}(r)}{\Delta V \rho_\alpha}, \tag{1.36}$$

where $n_{\alpha\beta}$ is the number of atoms of type β within a spherical shell between r and $r + \Delta r$ regarding a central atom of type α, ΔV is the volume of the spherical shell and ρ_α is the partial density of component α.

1.4.2 Bond angle distribution function

Another interesting function that can be calculated for unraveling the adsorbate structure is the bond angle distribution function (ADF). It describes the density variations as a function of the angle between a reference particle and two nearest neighbors within a given distance. It is quite common to analyze the first coordination shell, as can be seen in Fig. 1.5. Angular distribution function is defined

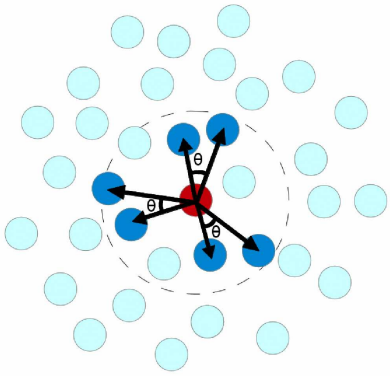

Figure 1.5: Schematic drawing of the system. Only the triplets, within the first coordination shell (dashed circle), which display an angle between θ and $\theta \pm \Delta\theta$ from a reference particle (red), contribute to the $f(\theta)$ calculation.

as the integral of the three body correlation function $g^{(3)}(r_1, r_2, \cos\theta)$ over the first coordination shell:

$$f(\theta) = 16\pi^2 \int_0^{r_c} \int_0^{r_c} r_{13}^2 dr_{13} r_{23}^2 dr_{23} g(r_{12}) g^{(3)}(r_{13}, r_{23}, \cos\theta), \tag{1.37}$$

where r_c is chosen as the distance value for the first minimum of the partial distribution function. In practice, this quantity is evaluated from the ensemble average of $\cos\theta_{132}$ histograms corresponding to the 1,3,2 triplets of particles which fulfill $r_{13} < r_c$ and $r_{23} < r_c$ (see Fig.1.5).

1.4.3 Conversion from μ to P

The experimental adsorption isotherm, also known as volumetric isotherm, relates the number of adsorbed molecules as a function of pressure. Hence, pressure has to be known for comparing the results provided by GCMC simulations with the measured isotherm. In the grand canonical ensemble, where the chemical potential is fixed, the system exchanges particles with a reservoir at the same chemical potential. That reservoir contains molecules that, in the case of ideal gas approximation, do not interact and they can be considered as a dense phase in equilibrium with a dilute vapor. This approximation can be used because at very low pressures, as the experimental ones, the adsorbate is in gas phase. Then for an ideal gas at temperature T, the relation between the chemical potential, μ, and the corresponding pressure $P_{id.gas}$ is given by

$$\beta\mu = ln(P_{id.gas}) - ln\left(\frac{k_B T}{\Lambda^3}\right) \tag{1.38}$$

where $\beta = 1/k_B T$ is the thermodynamic beta and $\Lambda = \sqrt{h^2/(2\pi m k_B T)}$ is the de Broglie wavelength.

Therefore, the pressure of the reservoir, $P_{id.gas}$, can be trivially extracted from equation 1.38

$$P_{id.gas} = \frac{k_B T}{\Lambda^3} e^{\beta\mu} \tag{1.39}$$

where μ is the fixed value of the chemical potential used in the GCMC simulation.

It is important to mention that the Peng-Robinson [27] and Redlich-Kwong equations of state [28], are commonly used for estimating the pressure. Its respective modifications proposed by Gasem *et al.* [29] and Soave *et al.* [30] are also widely used. However, it is usually assumed that at low pressures, as the ones considered in our studies, the gas ideal approximation works reasonably well.

1.4.4 Isosteric heat of adsorption

The isosteric heat of adsorption as a function of the number of adsorbed molecules, namely the experimental isosteric isotherm, can be a helpful representation to understand the endothermic or exothermic nature of the adsorption process at different loadings.

The isosteric heat of adsorption estimates the enthalpy change when a particle in the gas phase is adsorbed into the porous material. Among all approaches that can be found in the literature, we have chosen the energy/particles fluctuations route [31, 32]. The isosteric heat of adsorption, q_{st}, according to this route is given by

$$q^{st} = \frac{\langle N \rangle \langle U \rangle - \langle NU \rangle}{\langle N^2 \rangle - \langle N \rangle^2} + U^g + RT \tag{1.40}$$

where R is the ideal gas constant, T is the temperature, U_g is the potential energy of the gas phase, U is the total energy of the system (including the zeolite energy framework in the case we are considering it) and N is the number of particles in the simulation box. It is important to stress that U_g can be neglected assuming that adsorbate atoms behave as an ideal gas.

Chapter 2

Diffraction and Reverse Monte Carlo

As we are interested in the microscopic structure of the adsorbate/adsorbent system, diffraction experiments can provide us information about it. To extract this structural information from experimental diffractograms there are several computational methods. For example, Rietveld refinement is used to elucidate the atomic positions of a crystal from its diffraction pattern. A second possibility is Reverse Monte Carlo algorithm (RMC), which yields atom coordinates that are consistent with experimental diffraction data.

In this chapter, a general description of the diffraction theory is firstly provided. Moreover, the two scattering techniques used for this thesis are briefly described. Lastly, the RMC algorithm and some implementation details are shortly depicted.

2.1 Diffraction theory

Diffraction occurs when a wave is scattered by a periodic array of atoms with long-range order, producing constructive interference at specific angles. As shown in figure 2.1 (a), Bragg's law provides the required conditions for coherent scattering,in which the incident beam undergoes a change in direction without a change in wavelength, at a given peak position θ. For parallel planes of atoms, with a space d between them, constructive interference only occurs when Bragg's law is satisfied, according to [33, 34]

$$2dsin\theta = n\lambda \tag{2.1}$$

where θ is the angle formed by the incident beam and the surface of the crystal, n is an integer and λ is the wavelength of the incident beam. Therefore, Bragg's law relates observed scattered waves at angles θ to inter-planar distances d between lattice planes.

In diffraction, the momentum transfer vector $\mathbf{q}$, also known as scattering vector, is simply given by the difference between the incident and scattered wavevectors (as illustrated in Fig 2.1 (b)):

$$\mathbf{q} = \mathbf{k_{out}} - \mathbf{k_{in}}. \tag{2.2}$$

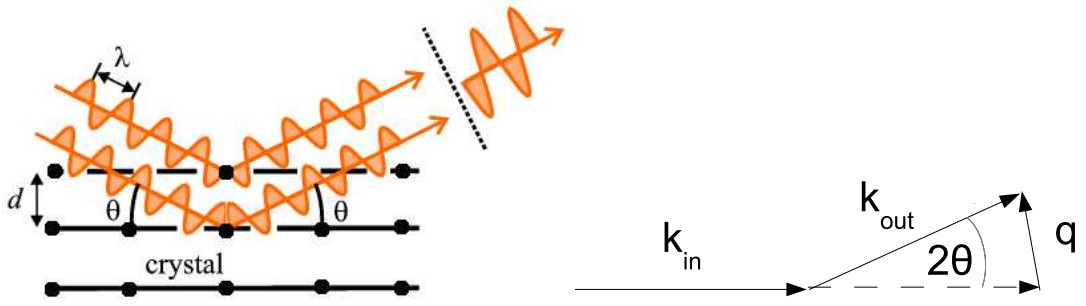

(a) (b)

Figure 2.1: (a) Constructive interference of two scattered waves by arrays of parallel atomic planes. (b) Schematic representation of the incoming (k_{in}) and the outgoing (k_{out}) wavevectors and the corresponding momentum transfer q for elastic scattering.

For elastic scattering, the wave energy is conserved and, consequently, the module of the incoming and outgoing scattered wavevectors are equal:

$$k_{in} = k_{out} = \frac{2\pi}{\lambda}. \tag{2.3}$$

Applying trigonometry to the wavevectors for elastic scattering (see Fig.2.1 (b)) it can be trivially obtained the relationship of the momentum transfer, q, and the scattering angle θ:

$$q = \frac{4\pi sin\theta}{\lambda} \tag{2.4}$$

Finally, combining Eq. 2.1 and 2.4, can be trivially deduced the relation between the momentum transfer q and the inter-planar distance d

$$q = \frac{2\pi}{d}. \tag{2.5}$$

The q-space representation for the diffraction data is commonly used for comparing the results obtained from different methods because the momentum transfer q does depend on neither the scattering technique (X-rays or neutrons) nor the incident wavelength.

Because the inter-planar distance d defines the coherent interference condition in Bragg's law (see Eq. 2.1), it is important to have an specific notation for the different atomic planes. This way, the observed diffraction peaks can be related to parallel planes of ordered atoms. Miller indices hkl label all parallel and equivalent planes by reducing intercepts on x, y, and z axes to the three smallest integers. Using this notation, the relationship between the inter-planar distance d_{hkl} and the unit cell parameters can be determined geometrically and depends on the crystal lattice. For a tetragonal crystal, as MEL type zeolite, this relationship is given by

$$\frac{1}{d_{hkl}^2} = \frac{h^2 + k^2}{a^2} + \frac{l^2}{c^2}. \tag{2.6}$$

2.1.1 Real and reciprocal lattice

Real space lattice

Unit cell is the repeating unit that uniquely defines its crystal structure. Hence, the whole crystal can be reproduced by simply repeating this unit cell in the three dimensions of space. Any crystal structure can be adequately described by using the so called Bravais lattice. The Bravais lattice concept is used to formally define a crystalline arrangement and it can be mathematically represented as an infinite array of discrete points in a three-dimensional real space with a vector $\mathbf{r}$ [33, 34]

$$\mathbf{r} = n_1\mathbf{a} + n_2\mathbf{b} + n_3\mathbf{c}, \tag{2.7}$$

where n_1, n_2 and n_3 are integers and $\mathbf{a}$, $\mathbf{b}$ and $\mathbf{c}$ are the three basic vectors of the unit cell. In other words, the volume defined by the vectors $\mathbf{a}$, $\mathbf{b}$ and $\mathbf{c}$ is the unit cell.

The unit cell can contain more than one atom. The basis of the unit cell provides a set of atomic coordinates (u_i,v_i,w_i) measured from any lattice point of each of these atoms. Then r_i, the position of an atom i, for a polyatomic unit cell, is simply given by

$$\mathbf{r}_i = (n_1 + u_i)\mathbf{a} + (n_2 + v_i)\mathbf{b} + (n_3 + w_i)\mathbf{c}. \tag{2.8}$$

Reciprocal space lattice

The diffraction pattern can be related to the crystal lattice by a mathematical construction called the reciprocal lattice. All wavevectors that produce plane waves according to the Bravais lattice are gathered in the reciprocal lattice. The unit vectors in the reciprocal space lattice can be calculated from the unit vectors in the real space lattice according to [33, 34]

$$\mathbf{a}^* = 2\pi\frac{\mathbf{b}\times\mathbf{c}}{\mathbf{a}\cdot(\mathbf{b}\times\mathbf{c})} \tag{2.9}$$

$$\mathbf{b}^* = 2\pi\frac{\mathbf{c}\times\mathbf{a}}{\mathbf{b}\cdot(\mathbf{c}\times\mathbf{a})} \tag{2.10}$$

$$\mathbf{c}^* = 2\pi\frac{\mathbf{a}\times\mathbf{b}}{\mathbf{c}\cdot(\mathbf{a}\times\mathbf{b})} \tag{2.11}$$

This new lattice is called reciprocal lattice because it can be mathematically shown that the dot product of a real lattice vector, $\mathbf{r}$, and a reciprocal lattice vector, $\mathbf{q}$ satisfies

$$\mathbf{r}\cdot\mathbf{q} = 2\pi n \tag{2.12}$$

where n is an integer.

Similar to the real space lattice (see Eq. 2.7), we can also define a reciprocal lattice vector $\mathbf{q}$, that corresponds to the momentum transfer $\mathbf{q} = \mathbf{k_{out}} - \mathbf{k_{in}}$, as a linear combination of the three reciprocal unit vectors

$$\mathbf{q} = h\mathbf{a}^* + k\mathbf{b}^* + l\mathbf{c}^* \tag{2.13}$$

where h, k and l are the Miller indices.

2.1.2 Lattice structure factor

The lattice structure factor, F_{hkl}, describes how the atomic arrangement influences the intensity of the scattered beam. For a given reflection hkl, F_{hkl} is the quantity that expresses both the amplitude and the phase of that reflection. It is mathematically defined as:

$$F_{hkl}(\mathbf{q}) = \sum_{i}^{N} f_i e^{i\mathbf{q}\cdot\mathbf{r}_i} = \sum_{i} f_i e^{2\pi i(hu_i+kv_i+lw_i)}, \tag{2.14}$$

where N is the total number of atoms in the unit cell, f_i is the atomic scattering factor, which depends on the experimental technique, and r_i and q are the lattice points of the real and reciprocal space lattice, respectively. From equations 2.8 and 2.13, the dot product of real and reciprocal vectors can be translated to a product of Miller indices hkl and atom coordinates u_i, v_i and w_i.

The lattice structure factor, F_{hkl}, is directly related to the intensity of the diffracted peaks, namely the total scattering structure factor $S(q)$, according to

$$S(q) = |F_{hkl}(\mathbf{q})|^2 \tag{2.15}$$

2.1.3 Powder diffraction

In single crystal diffraction, commonly used for precise determination of unit cell dimensions and atom positions, the experimental sample must be an individual robust crystal carefully chosen. Furthermore, as the sample has to be rotated, data collection is generally slow. In contrast, powder diffraction allows rapid diffraction analysis of multi-component systems without any extensive sample preparation. For these reasons, all diffraction measurements performed in this thesis where obtained from a powder sample, rather than from an individual crystal. In the powder sample that contains thousands of crystallites, all possible diffraction peaks should be observed, because every possible crystalline orientation is represented equally. For every set of planes, there are an equal and a statistically relevant number of crystallites that diffract.

Structure factor calculation in powder diffraction

In the case of powder Bragg diffraction, the orientationally averaged structure factor is expressed by [35]:

$$S(q) = \frac{2\pi^2}{NV\langle f\rangle^2} \sum_{\mathbf{q}'} |F_{hkl}(\mathbf{q}')|^2 \delta(q-q')/q'^2 \tag{2.16}$$

where N is the total number of atoms, V denotes the volume of the unit cell, $\mathbf{q}'$ are the allowed reciprocal lattice vectors, $\langle f\rangle$ is the average of scattering factors of the different atoms that can be found in the sample (see Sections 2.1.4 and 2.1.5) and $F_{hkl}(\mathbf{q})$, defined above in Eq. 2.14, is the lattice structure factor . The $1/q'^2$ factor stems from the angular integration over all the possible $\mathbf{q}'$ orientations in the powder sample [35] and $\delta(q-q')$ term corresponds to the experimental resolution function of the experimental technique.

2.1.4 X-rays

Introduction

X-ray photons scatter by interaction with the electron cloud surrounding each atom of the sample. As they interact with the electrons of the atomic cloud, the strength with which an atom scatters light is proportional to its number of electrons, i. e. its atomic number Z. This means that, in the presence of heavy atoms with many electrons, it might be difficult to detect light atoms by X-ray diffraction. This fact dramatically reduces the peak intensities when scattering angle 2θ increases. This angular dependence for peak intensities is incorporated with the atomic form factor $f(q)$, denoted as f_i in Eq. 2.14, which is the Fourier transform of the electron density of an atom. Assuming that the electron cloud is spherically symmetric, the atomic form factor only depends on the the scattering vector q and it can be effectively approximated by a sum of Gaussians

$$f(q) = \sum_{i=1}^{4} a_i \exp\left(-b_i \left(\frac{q}{4\pi}\right)^2\right) + c \tag{2.17}$$

where a_i, b_i and c are the tabulated constants for each element in the experimental sample, shown in Table 2.1.

Table 2.1: Atomic form factor parameters used for the different atoms adsorbed on MEL zeolite [36].

Atom	a_1	a_2	a_3	a_4	b_1	b_2	b_3	b_4	c
Si	6.2915	3.0353	1.9891	1.5410	2.4386	32.3337	0.6785	81.6937	1.1407
O	3.0485	2.2868	1.5463	0.867	13.2771	5.7011	0.3239	32.9089	0.2508
C	2.31	1.02	1.5886	0.865	20.8439	10.2075	0.5687	51.6512	0.2156

X-rays powder diffraction

In practice, an experimental X-rays powder diffractogram is a record of photon intensity versus detector angle 2θ. The detector moves on a circle centered on the sample covering 2θ range as shown in Fig. 2.2. Monochromators remove unwanted wavelengths of incoming radiation from the incident X-ray beam, and parallel plate collimators are used to limit the divergence of the incident radiation, refocusing X rays into parallel paths.

X-rays high-resolution powder diffraction measurements were performed in the materials science and powder diffraction beamline (MSPD) at ALBA synchrotron. In Appendix B, a brief description of a synchrotron source can be found.

2.1.5 Neutrons

Introduction

Neutrons have zero charge and negligible electric dipole. Thus, in contrast to X-rays which interact with the electron cloud surrounding each atom, the scattering of neutrons occurs at the atom nuclei. For this reason, neutrons are highly penetrating in comparison to X-rays. As nuclei are point scattering centers, neutron scattering

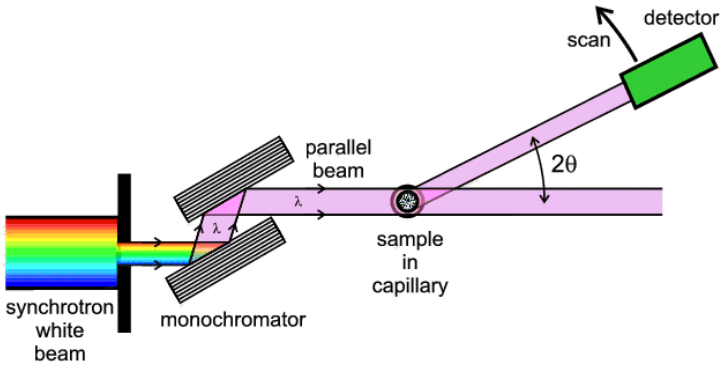

Figure 2.2: Schematic representation of the experimental setup for X-rays powder diffraction.

lengths b, which measure the strength of the neutron-nucleus interaction (denoted as f_i in Eq. 2.14), do not show an angular dependence. Most of atoms scattering lengths have similar magnitude and, for this reason, neutrons are the choice to detect light elements in combination with heavy atoms. Moreover, neutrons carries a magnetic moment, which can be used to determinate the magnetic properties of experimental samples.

In general, there are two kinds of neutron diffraction measurements. In the first one, similarly to the above described X-rays powder diffraction, a constant wavelength neutron beam is scattered and the intensity the diffracted waves are collected as a function of the scattering angle θ. Secondly, to extend the accessible q range, the time of flight of the diffracted neutrons from a incoming white neutron beam it can be also measured. This second technique is shortly described in the following section.

Time of Flight powder diffraction

In time of flight (TOF) experiments, data are collected in different banks at a constant angle $2\theta_o$, using a white neutron beam diffracted on a polycrystalline sample. Instead of measuring Bragg reflection by scanning a detector from low to high 2θ scattering angles, in the TOF technique, a neutron pattern of scattered neutrons is measured as a function of its time of flight at a fixed scattering angle, $2\theta_o$ [37]. Hence, Eq. 2.1 is written as follows

$$\lambda_{hkl} = 2d_{hkl}sin\theta_o \tag{2.18}$$

where λ_{hkl} is the wavelength of the incoming neutron and d_{hkl} the inter-planar d-spacing of the crystal. The neutron wavelength is defined, according to the de Broglie relation, as

$$\lambda = \frac{h}{m_n v} = \frac{h}{m_n L}\ TOF \tag{2.19}$$

where h is the Planck constant, v is the neutron velocity, m_n is the neutron mass, L is the total flight path and TOF the measured time of flight.

Combining above equations yields a relation between the time of flight (TOF) and inter-planar distance d :

$$TOF = \frac{2m_n sin\theta_o L}{h} \cdot d_{hkl} = DIFC \cdot d_{hkl}. \tag{2.20}$$

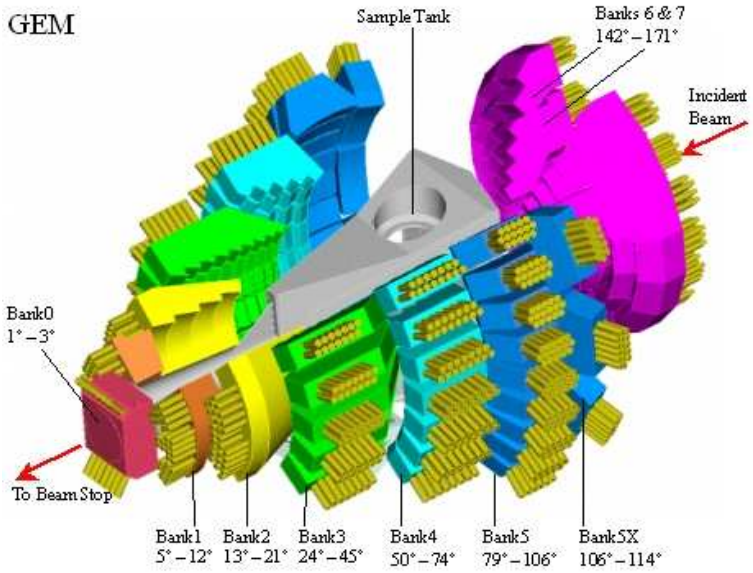

Figure 2.3: Schematic layout of the detectorbanks of the GEM detector array [38]

If we consider a real time-of-flight diffractometer, equation 2.20 should be slightly modified. Firstly, $DIFA$ diffractometer parameter accounts the fact that neutron absorption of an atom is proportional to the wavelength. The second parameter, called $ZERO$ is a shift in TOF values as a consequence of the small differences between the timing signals in the instrument data acquisition systems. According to this, the relationship between the d-spacing d_{hkl} and its TOF is given by

$$TOF = DIFA \cdot d_{hkl}^2 + DIFC \cdot d_{hkl} + ZERO, \tag{2.21}$$

where the three parameters DIFC, DIFA and ZERO are characteristic of a given counter bank on a TOF powder diffractometer.

For the study of the argon adsorption in MEL zeolite, powder diffraction neutron time-of-flight measurements were carried out in GEM diffractometer at ISIS spallation facilities. The different banks of the GEM diffractometer can be seen in Fig. 2.3 and a description of a spallation source for producing intense pulsed neutron beams is written in Appendix C. As mentioned before, this experimental technique was chosen not only because a broader q range can be measured but also because, as neutrons are highly penetrating, they can pass through the thermal bath needed to reach the experimental temperature of 77K.

2.2 Reverse Monte Carlo method

For decades, Reverse Monte Carlo algorithm (RMC) [39] has been used for unraveling the microscopic structure of different materials (liquids, glasses and crystals)

from experimental diffraction measurements [40, 41, 42].

In short, the RMC method produces sets of three-dimensional particle coordinates for which the calculated structure factor fits the input diffraction data within the estimated experimental errors. The goodness-of-fit is quantified using a χ^2-value:

$$\chi^2 = \sum_{i=1}^{N_q} \frac{(S_{calc}(q_i) - S_{exp}(q_i))^2}{\sigma^2(q_i)}, \tag{2.22}$$

where q is the modulus of the scattering vector and the sum runs over all experimental points, N_q; S_{exp} and S_{calc} are the experimental and simulated structure factors, respectively, and σ is the standard deviation for the experimental point i.

In the original RMC approach we deal only with translational or rotational trial movements. To minimize the χ^2 factor, a random movement of a randomly chose particle is attempted. If the new non-overlapping position reduces differences between experimental and calculated structure factors, the move will be accepted. Otherwise, the move is accepted according to an acceptance probability, P^{acc}, given by [39]

$$P^{acc} = \min\left(1, \exp\left(-\frac{\chi^2_{new} - \chi^2_{old}}{2}\right)\right) \tag{2.23}$$

where χ^2_{old} and χ^2_{new} are the χ factors corresponding to the initial and proposed atomic coordinates, respectively.

Finally, an exclusion core around each particle is defined, r_{cutoff}, to take in account its effective size. If the proposed position overlaps with any other particle in the simulation box, then the move will be automatically rejected.

2.2.1 *N*-RMC

One of the main objectives of this thesis is to provide a microscopic description of adsorbed fluids on zeolites. As zeolites have relatively narrow porous in comparison with the adsorbate most translational moves (and rotations in the case of molecules) will be rejected due to overlaps with the adsorbent framework. The very low diffusivity within the channels and the high anisotropy of the medium slows down considerably the efficiency of the standard RMC algorithm. To speed up the sampling, we have developed an extension of the RMC algorithm that circumvents the problem of slow difusivities in tightly confined media. In addition to the usual translational moves, also particle insertion and deletion trials [5] are attempted. In order to highlight the fact that the number of particles is variable, we named this new method as N-RMC. The number of sample particles, N_{exp}, must be known and it can be estimated from a variety of experimental sources as volumetric adsorption experiments. Therefore, the original acceptance probability (see Eq. 4.9) is modified because apart from the minimization of χ^2 factor, a constraint on the target number of adsorbed particles, N_{exp}, is also included [5]:

$$P^{acc} = \min\left(1, \exp\left(-\frac{\chi^2_{new} - \chi^2_{old}}{2} - \frac{\Delta N^2_{new} - \Delta N^2_{old}}{2}\right)\right), \tag{2.24}$$

where $\Delta N_i^2 = (N_i - N_{exp})^2/\sigma_N^2$, N being the instantaneous number of adsorbed particles and σ_N the experimental uncertainty in N_{exp}. The validity of this new method will be shown and discussed in chapter X.

2.2.2 Constraints

The performance of RMC can be considerable improved by incorporating all the information that we know about the system. For example, if we know the coordination number, a constraint can be added for considering this effect. Similarly if we are dealing with molecules of known geometries, constraints can be incorporated to avoid the deformation of the model system. In this way, to avoid deformations of the zeolite framework two kind of elastic potentials between the *O-O* and *Si-O* atoms have been added to the atoms of the MEL zeolite.

The first term, the bonding one, depends on the distance between *Si-O* atoms that form a oxygen tetrahedral unit

$$U_{bond} = \frac{(r_{Si-O} - r_0)^2}{2\sigma_{bond}^2}, \tag{2.25}$$

where r_{Si-O} is the distance between the bonded *Si-O* atoms of the zeolite framework, σ_{bond} is the weight of the bonding term with respect to the other terms in the acceptance probability and r_0 are the equilibrium distances for the experimental MEL structure provided by Terasaki *et al.* [11], as we have done for Demontis and Nicholas modified potential models.

The second term, the bending one, limits the angle of the oxygen atoms that belongs to the same tetrahedra

$$U_{bend} = \frac{(\theta_{O-Si-O} - \theta_0)^2}{2\sigma_{bend}^2}, \tag{2.26}$$

where θ_{O-Si-O} is the angle formed by a central silicon atom and two oxygen atoms that belong to the same oxygen tetrahedral unit, σ_{bend} is the weight of the bending term with respect to the other terms in the acceptance probability and θ_0 are the experimental angles of the zeolite structure taken from the literature.

Finally, k_χ factor weights the fitting of the experimental spectra in comparison with the flexibility of the zeolite. Hence, the acceptance probability for a proposed translation of an atom for the flexible zeolite is computed as

$$P^{acc} = \min\left(1, \exp\left(-k_\chi \Delta\chi - \Delta U_{bond} - \Delta U_{bend}\right)\right), \tag{2.27}$$

where $\Delta\chi$ is $(\chi^2_{new} - \chi^2_{old})/2$ according to the Eq. 4.10, whereas the two other terms, ΔU_{bond} and ΔU_{bend}, are the differences between the total bond and bend energy values for the current and the proposed position, respectively.

2.3 Implementation details

2.3.1 Diffuse scattering: super-cell approximation

For disordered media, as adsorbates in a zeolite porous, the contribution of the diffuse scattering that comes from the disorder of the system, can be also calculated using equation 7.1. However, to include correlations at longer distances, a super-cell, formed by many replicas of the unit cell, has to be used. As the evaluation of the super-cell reciprocal vectors is a time-consuming task, we applied the super-cell approach, proposed by Mellegaard *et al*, [35]. According to this approximation, the intensity of each peak is averaged, within a range of $q = 0.1\mathring{A}^{-1}$, according to

Eq. 7.1. In contrast to the Bragg scattering calculation, where only the reciprocal vectors of the unit cell are considered, the diffuse term takes in account the reciprocal vectors of the total simulation box and its corresponding volume V_{total}.

2.3.2 Renormalization

For simplicity, as numerical values of the experimental intensities can not be easily interpreted, a minimization problem is solved for each movement attempt (insertion, deletion and translation) to minimize the χ^2 factor. For the proposed movement, the new considered factor, χ'^2, is defined as [43]

$$\chi'^2 = \sum_{i=1}^{N_q} \frac{(S_{calc}(q_i) - \frac{S_{exp}(q_i) - x_1}{x_2})^2}{\sigma^2(q_i)}, \tag{2.28}$$

where x_1 and x_2 are the two calculated variables in the minimization. This χ'^2 is the factor used for the acceptance probability calculation.

2.3.3 peak shape functions

2.3.4 Biased insertion

In the same manner as we have done in GCMC simulations (see section 1.2.4), we only do insertion trials in those lattice points where the test particle do no overlap with the zeolite framework. As mentioned before, doing this bias the computing time is remarkably reduced.

X-rays peak shape functions

Some sources of error associated with the focusing circle, sample displacement and transparency yield a characteristic shape for the diffraction peaks that can be described by Pseudo-Voigt functions. Pseudo-Voigt function V_p, widely used for X-ray diffraction peak shapes profiles, is the result of a linear combination of a Gaussian $G(2\theta)$ and a Lorentzian distribution $L(2\theta)$ [44] :

$$V_p(2\theta) = \eta \cdot L(2\theta) + (1-\eta) \cdot G(2\theta) \quad with \;\; 0 < \eta < 1 \tag{2.29}$$

where $G(2\theta)$ and $L(2\theta)$ are given by

$$G(2\theta) = \sqrt{\frac{\log 2}{\pi}} \cdot \frac{1}{HWHM} \cdot e^{-\log 2 \cdot \left(\frac{2\theta - 2\theta_0}{HWHM}\right)^2} \tag{2.30}$$

$$L(2\theta) = \frac{1}{\pi} \cdot \frac{HWHM}{HWHM^2 + (2\theta - 2\theta_0)^2}. \tag{2.31}$$

where $2\theta_0$ is the scattering angle for a given peak maximum and $HWHM$ is the half width at half maximum whose 2θ dependence for X-rays was mathematically described by Caglioti *et al.* [45] with three free parameters U, V, W according to the equation:

$$HWHM = \sqrt{U \cdot \tan^2(\theta) + V \cdot \tan(\theta) + W}. \tag{2.32}$$

TOF peak shape functions

As the white neutron-pulse impose additional asymmetric broadening effects, TOF profile function, named $H(\Delta TOF)$, has a more complex functional form. One rather simple empirical TOF profile function, provided by Von Dreele *et al.* is given by a convolution of a Gaussian function with two back-to-back exponentials [46]

$$H(\Delta TOF) = N\left[e^{u} erfc(y) + e^{v} erfc(z)\right] \tag{2.33}$$

where $H(\Delta TOF)$ denotes the multiplicative factor of each of Bragg reflection for a given time-of-flight increment, ΔTOF, which is defined as the difference between the reflection position, TOF_{ph}, and the profile point TOF.

The normalization factor, N, is

$$N = \frac{\alpha\beta}{2(\alpha+\beta)} \tag{2.34}$$

and the coefficients u, v, y and z are

$$u = \frac{\alpha}{2}\left(\alpha\sigma^2 + 2\Delta T\right) \tag{2.35}$$

$$v = \frac{\beta}{2}\left(\beta\sigma^2 - 2\Delta T\right) \tag{2.36}$$

$$y = \frac{\alpha\sigma^2 + \Delta T}{\sqrt{2\sigma^2}} \tag{2.37}$$

$$z = \frac{\beta\sigma^2 - \Delta T}{\sqrt{2\sigma^2}} \tag{2.38}$$

The three coefficients α, β and the Gaussian variance, σ^2, are defined as

$$\alpha = \alpha_0 + \alpha_1/d_{hkl} \tag{2.39}$$

$$\beta = \beta_0 + \beta_1/d_{hkl}^4 \tag{2.40}$$

$$\sigma^2 = \sigma_0^2 + \sigma_1^2 \cdot d_{hkl}^2 + \sigma_2^2 \cdot d_{hkl}^4, \tag{2.41}$$

where $\alpha_0, \alpha_1, \beta_0, \beta_1, \sigma_0^2, \sigma_1^2, \sigma_2^2$ are the seven input values required for the TOF peak shape function calculation.

Unit cell refinement and Pawley profile fitting

One the one hand, a unit cell profile fitting is firstly used to estimate unit cell lattice vectors **a**, **b** and **c**. By accurately measuring peak positions with a peak search algorithm over a long range of scattering vectors q, the unit cell lattice parameters of the sample can be refined by a least-squares fitting procedure that minimizes the differences between the observed and the estimated scattering peak positions for a given set of values of the unit cell vectors.

On the other hand, as the exact peak-width function is not known *a priori*, Pawley suggested that peak shape parameters can be fitted with a least-squares minimization procedure. Assuming that a peak position is only determined by the unit cell vectors **a**, **b** and **c** and the $2\theta_0$ error, a peak width is simply determined by the resolution function parameters and the peak intensity I_{hkl}. In contrast to

Rietveld refinement, atomic positions are not needed, because, in Pawley refinement, peak intensities are simply taken from the experimental diffractogram. Then, Pawley profile fitting provide the peak shape parameters which minimize the differences between experimental and calculated structure factors. In the case of X-rays diffraction, parameters U, V and W of equation 2.32 are provided. For neutron diffraction, profile fitting yields the six parameters involve in TOF peak shape function, $\alpha_0, \alpha_1, \beta_0, \beta_1, \sigma_0^2, \sigma_1^2, \sigma_2^2$, described in section 2.2.4.

2.3.5 Parallel computing: GPU

The only structure factor definition that can be used for a system where crystal (zeolite) and disorder material (adsorbate) are presented is the called 'reciprocal space' route (see Eq. 7.1). When this route is used, as all the reciprocal vectors must be calculated, a time consuming evaluation has to be done when the simulation size or the number of particles in the simulation box increases. Because of the cosine of the dot product $\mathbf{q} \cdot \mathbf{r}_i$ in Eq. 2.14 can be independently calculated, the structure factor estimation can be easily parallelized using a graphics processing unit (GPU) together with a CPU to accelerate the RMC simulation. The evaluation of the structure factor can be up to 100 times faster when all vectors of the reciprocal space are equally distributed among the hundreds of cores available in a typical GPU in comparison with the serial RMC algorithm.

Also the peak shape functions for TOF and X-rays structure factors have been implemented in CUDA programming language. The evaluation of the time consuming exponential and complementary error functions (see Eq. 2.30 and 2.33) are independently evaluated by every available core in the GPU unit.

Part III

Results

Chapter 3

Reverse Monte Carlo modelling: the two distinct routes of calculating the experimental structure factor

J. Mol. Liq., **207**, 211-215 (2015)

Vicente Sánchez-Gil[1], Eva G. Noya[1], Laszlo Pusztai[2] and Laszlo Temleitner[2]

[1] *Instituto de Química Física Rocasolano, Consejo Superior de Investigaciones Científicas, CSIC, Calle Serrano 119, 28006 Madrid, Spain*

[2] *Institute for Solid State Physics and Optics, Wigner Research Centre for Physics, P.O. Box 49, H-1525 Budapest, Hungary*

Abstract

Two different Reverse Monte Carlo strategies, 'RMC++' and 'RMCPOW', have been compared for determining the microscopic structure of some liquid and amorphous solid systems on the basis of neutron diffraction measurements. The first, '$g(r)$ route', exploits the isotropic nature of liquids and calculates the total scattering structure factor, $S(Q)$, via a one-dimensional Fourier transform of the radial distribution function. The second, called 'crystallography' route, is based on the direct calculation of $S(Q)$ in the reciprocal space from the atomic positions in the simulation box. We describe these two methods and apply them to four disordered systems of increasing complexity. The two approaches yield structures in good agreement to the level of two- and three body correlations; consequently, it has been proven that the 'crystallography route' can also deal perfectly with disordered materials. This finding is important for future studies of liquids confined in porous media, where handling Bragg and diffuse scattering simultaneously is unavoidable.

3.1 Introduction

The Reverse Monte Carlo (RMC) method [47] is a simple tool used for decades for elucidating the detailed atomic level structure of liquids and solids from scattering measurements. Over the past 25 years, RMC has been successfully applied to a wide variety of disordered materials that display structural disorder of varying extent: simple liquids [40], molten salts [48], molecular liquids [49, 50, 51], water [52] and aqueous solutions [53], metallic [54] and covalent [55, 41] glasses. A separate class of applications has targeted 'disordered crystals' in which long range (crystalline) order and local (i.e., within the first coordination sphere) disorder are present simultaneously: examples may be crystals of silver and copper halides [42, 56] and of tetrahedral molecules [57].

It was clear early on [42] that dealing with genuine crystalline materials requires strategies different from those applicable for isotropic liquids/amorphous materials, due to the presence of long range periodic symmetries and the locally anisotropic nature of crystals. Just before the turn of the millennium, the (so far) ultimate solution was created: the RMCPOW software [35] is able to calculate Bragg- and diffuse scattering intensities directly from the particle coordinates, even for powder diffraction data obtained from laboratory X-ray sources and thermal neutron diffraction. For experimental data measured over very wide momentum transfer ranges, the RMCProfile strategy [58], that involves the separation of the Bragg profile and Fourier-transform to real space, and a subsequent modelling of the total radial distribution function and the Bragg-profile, is also frequently used. The PDFGui software [59], performing PDF-based analysis of powder diffraction data, is a powerful tool for providing structural models based on the radial distribution function of crystalline materials. This is an alternative to the strictly unit-cell based investigation of crystalline structures; on the other hand, it is not capable of dealing with genuinely disordered structures. For isotropic disordered materials the original strategy of RMC [47] may be used, i.e., from the atomic positions, first the radial distribution functions (RDF) are calculated, which later are Fourier transformed to the reciprocal space, so that primary experimental information, the total scattering structure factor (TSSF) may serve as 'target function' of RMC. Software that can realize this strategy may be RMC++ [60], RMC_POT [61] or RMCProfile [58, 62]. Details of the two strategies will be provided below; for now, it is important to state that a proper comparison between the two strategies is still missing.

The primary aim of this work is to test these strategies for several model systems. Since it is obvious that the simple route, via the calculation of the RDF, cannot be applicable for crystals, what needs to be tested is whether the more time consuming 'crystallographic' approach [35] can be used for isotropic disordered systems, such as liquids. Beyond the 'per se' interest, the timeliness of such a study lies in that a very important class of 'mixed' systems, 'fluids in pores' would require a method that can handle both perfect crystals (like zeolites) and liquids (like water) [63, 64, 5]. Note that the 'crystallographic' approach has already been proven to reproduce the atomic structure of simple adsorbed fluids (up to the level of three body correlations) in zeolites of varying pore sizes using the N-RMC method in which the number of particles is an additional adjustable parameter [5]. In that work the target structure factor was obtained by simulation rather than from experiments and the study was restricted to simple fluids. Structural investigations of such complicated materials,

that are of utmost significance in catalysis, oil industry, soil chemistry..., will not be possible until an established method of structural modelling can be proven to be applicable. Our aim now is to see whether the 'crystallographic' approach is also suitable for fitting experimental structure factors for more complex fluids.

Bearing in mind the above, the two approaches are tested on disordered one component systems of increasing complexity, from liquid argon to amorphous silicon. Liquid argon (l-Ar) is one of the simplest fluids in all respects: it can be easily described using radially symmetric pair potentials [65]. Liquid gallium (l-Ga), is a unique metallic element with possible short-lived covalent bonds that manifest in the slightly unusual shape of the main peak of the total scattering structure factor [66]. Liquid selenium (l-Se) is one of the most unusual elemental liquids, because of the twofold coordination of the atoms and the resulting chain-like structure [67]. Finally, amorphous silicon (a-Si) can be regarded as a classic example of a disordered fourfold-coordinated covalent material that, in contrast to its well-known crystalline form, lacks the long-range order [68]. In the cases of l-Ga, l-Se and a-Si, experimental data [66, 69, 70] are from neutron diffraction measurements. In the case of argon, a computer-generated model of the liquid [71] has been employed, for two reasons: (1) this way, no systematic experimental errors had to be cared for, and (2) the early experimental data [72] exhibited some residual systematic errors that made a thorough comparison of the methods somewhat cumbersome.

3.2 The two approaches for calculating the measurable total scattering structure factors within RMC

Details of the RMC method can be found in various publications [47, 58, 62, 73, 74, 60, 61] and therefore, here we will concentrate only on the parts relevant for calculating the structure factor from particle coordinates.

In short, the RMC algorithm produces sets of three-dimensional particle coordinates for which the calculated structure factor fits the input diffraction data within the estimated experimental errors. The goodness-of-fit is quantified using a χ^2-value:

$$\chi^2 = \sum_{i=1}^{N_Q} \frac{(S_{calc}(Q_i) - S_{exp}(Q_i))^2}{\sigma^2(Q_i)}, \tag{3.1}$$

where Q is the modulus of the scattering variable, the sum runs over all experimental points, N_Q; S_{exp} and S_{calc} are the experimental and simulated structure factors, respectively, and σ is the 'estimated' standard deviation for the experimental point i.

To minimize χ^2, random movements are attempted for all atoms in the simulation box. If the new non-overlapping position reduces differences between experimental and calculated structure factors, the move will be accepted. Otherwise, the move is accepted according to an acceptance probability, P^{acc}, given by

$$P^{acc} = \min\left(1, \exp\left(-\frac{\chi^2_{new} - \chi^2_{old}}{2}\right)\right), \tag{3.2}$$

where χ^2_{old} and χ^2_{new} correspond to the original and proposed atomic coordinates, respectively.

Finally, an exclusion core around each particle is defined, r_{cutoff}, to reflect its effective size. If the proposed position overlaps with any other particle in the simulation box then the move will be automatically rejected. Further constraints can be applied, for example, on the coordination number and/or nearest neighbor distances and angles [73, 74, 60, 58, 62].

The different approaches that we present here, are based on two different ways of calculating the total scattering structure factor , S_{calc}, from the particle coordinates.

3.2.1 Method I: the 'g(r) route' (RMC++)

This approach is based on the one-dimensional Fourier transformation of the radial distribution function (RDF). For one component systems, the RDF can simply be calculated from the atomic positions as

$$g(r) = \frac{n(r)}{\Delta V \rho}, \tag{3.3}$$

where $n(r)$ is the number of atoms at a distance between r and $r + \Delta r$ from a central atom, ΔV is the volume of a spherical shell between r and $r + \Delta r$ and ρ is the number density of the system.

Liquids and amorphous materials can be considered isotropic beyond nearest-neighbor distances so that for switching between the real and reciprocal space, a one-dimensional Fourier transform is widely used. Radial distribution functions can be Fourier transformed and weighted for the actual experiment thus providing the total scattering structure factor, $S(Q)$. For neutron scattering measurements and one component systems, the appropriate Fourier transform is given by

$$S(Q) = 1 + \frac{4\pi\rho\langle b\rangle^2}{Q}\int_0^\infty r[g(r) - 1]sin(Qr)dr, \tag{3.4}$$

where ρ denotes the number density of the sample, $\langle b\rangle$ is the neutron scattering length of the atom type in question, Q are the moduli of the reciprocal lattice vectors and the integral runs over atomic distances r. In practice, a discrete integration using the so called rectangular method [74] is performed with a summation whose upper limit is restricted by the half-length of the simulation box. This method is implemented in, for instance, the RMC++ [74, 60], RMC_POT [61] and RMCProfile [58, 62] software packages.

3.2.2 Method II: the 'crystallography route' (RMCPOW)

In contrast to Method I, the 'crystallography route', implemented by the software RMCPOW [35], is based on the super-cell approximation, repeating the 'unit cell' (i.e., in our case, the simulation cell) in each direction. The total scattering structure factor, $S(Q)$, is calculated using a three-dimensional Fourier transformation to the

reciprocal space from atomic coordinates. In this way, RMCPOW can deal with ordered and disordered systems because diffuse (local disorder) and Bragg scattering (crystalline, long range order) are both considered. Diffuse intensities, that are assumed to vary smoothly, are locally averaged whereas for Bragg intensities the same summation is performed without averaging (see Ref. [35] for details).

In the case of neutron diffraction, the orientationally averaged structure factor [35] is

$$S(Q) = \frac{2\pi^2}{NV < b >^2} \sum_{\mathbf{Q}'} |F(\mathbf{Q}')|^2 \delta(Q - Q')/Q'^2. \tag{3.5}$$

Where N and V are, respectively, the number of atoms and the volume of system, $\mathbf{Q}'$ are the allowed vectors in the reciprocal cell, and $\langle b \rangle$ is the average of the coherent scattering lengths. The $1/Q'^2$ factor stems from the angular integration over all the possible $\mathbf{Q}'$ orientations [35]. $F(\mathbf{Q})$ contains the correlations between scattering nuclei and is given by

$$F(\mathbf{Q}) = \sum_{j=1}^{N} b_j \exp(i\mathbf{Q}\mathbf{R}_j), \tag{3.6}$$

where $\mathbf{R}_j$ denotes the position of atom j in the unit cell.

It is important to point out that no Fourier transformation is involved in this scheme and therefore, the usual numerical problems (truncation, aliasing) in conjunction with that do not occur. Another thing to notice is that if Eq.7.1 was calculated for an isotropic system without periodical long range ordering then the vectors could be substituted by their magnitudes and the summation could be replaced by integration; that is, eventually, Eq.3.4 would be reproduced.

3.3 Calculations performed

As mentioned before, approaches I and II are tested here on disordered one component systems of increasing complexity, from liquid argon to amorphous silicon. The differences in terms of structural order can be clearly seen in Fig.4.3, where the experimental and simulated structure factors for the four systems are shown. Note that as the complexity of the test systems increases, new features of the 'diffuse' scattering appear but not any Bragg peak and therefore method I (the '$g(r)$ route') can also be used. In all cases, simulated and experimental data are from neutron diffraction 'measurements'.

For l-Ar, the simplest case, modelled data from canonical Monte Carlo simulations at 85K have been included. In this way, the target structure is accurately known and we have access to the real RDF and ADF to compare with. In the canonical Monte Carlo simulation argon atoms are modelled using Lennard-Jones interactions and the parameters of the LJ potential were taken from the literature [71].

All simulations have been performed using the RMC++ [60] and RMCPOW [35] free software packages with cubic simulation boxes of side length 32Å for l-Ga and a-Si and 50Å for l-Ar and l-Se. In table 4.1 the experimental density and the effective size of the particles for each test case are shown. For simplicity, as the aim of this work is to compare the two approaches, we have chosen a uniform value for the 'experimental' standard deviation of all Q-values, σ=0.001. As it can be seen

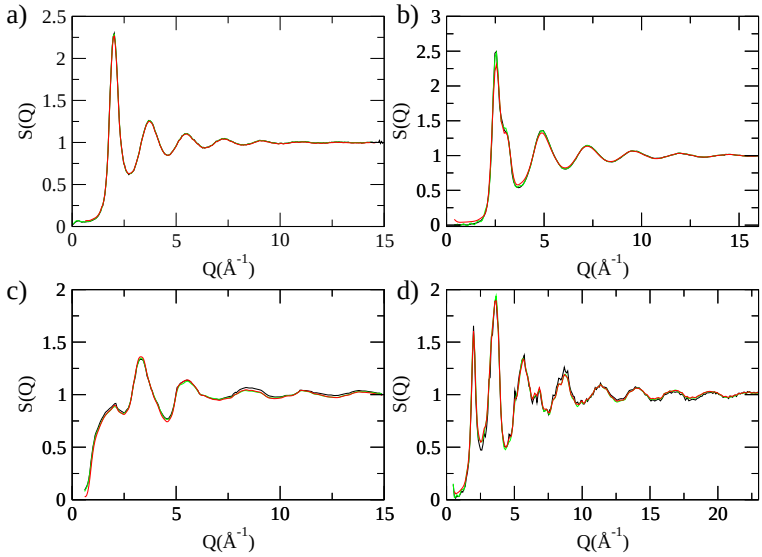

Figure 3.1: Comparison of the experimental structure factors provided by experiments (black line), RMC++ (green line) and RMCPOW (red line). From top to bottom and from left to right a) liquid argon (modelled data, from Monte Carlo simulation, see text for details) b) liquid gallium (experiment from Ref. [66]) c) liquid selenium (experiment from Ref. [69]) d) amorphous silicon (experiment from Ref. [70]).

in Fig.4.3, where target and simulated structure factors are hardly distinguishable, this value produces good quality fits.

Table 3.1: Experimental density and r_{cutoff} used for the model systems.

	ρ (atoms/Å^3)	r_{cutoff} (Å)
l-Ar	0.02125	2.7
l-Ga	0.05197	2.2
l-Se	0.0298	2.0
a-Si	0.04846	2.2

A better comparison of configurations provided by the different RMC strategies can be made by computing the radial distribution functions (RDF) and some simple three body correlation functions. Such comparison is able to reveal subtle variations of the structure that result from the different ways of calculating the total scattering structure factor. As defined above, the RDF can be determined from Eq.3.3. For three body correlations we calculate the bond angle distribution ('angular distribution function', ADF) that can be defined as the integral of the three body correlation function $g^{(3)}(r_1, r_2, \cos\theta)$ over the first coordination shell:

$$f(\theta) = 16\pi^2 \int_0^{r_c} \int_0^{r_c} r_{13}^2 dr_{13} r_{23}^2 dr_{23} g(r_{12}) g^{(3)}(r_{13}, r_{23}, \cos\theta), \tag{3.7}$$

where we chose r_c as the position of the first minimum of the radial distribution function in each test system. This function gives the distribution of angles between

pairs of nearest neighbors with respect to a central atom. The neutron scattering lengths have been taken from Ref. [75].

3.4 Results and discussion

•Liquid argon

We start by presenting results for argon using the modelled data from the canonical Monte Carlo simulation. As it can be seen in Fig.3.2, the agreement is almost perfect for RDF and ADF. Therefore it is clearly shown that for 'perfect' experimental data, and for a system with purely two body interactions, both RMC approaches reproduce the target structure to the level of two- and three-body correlations.

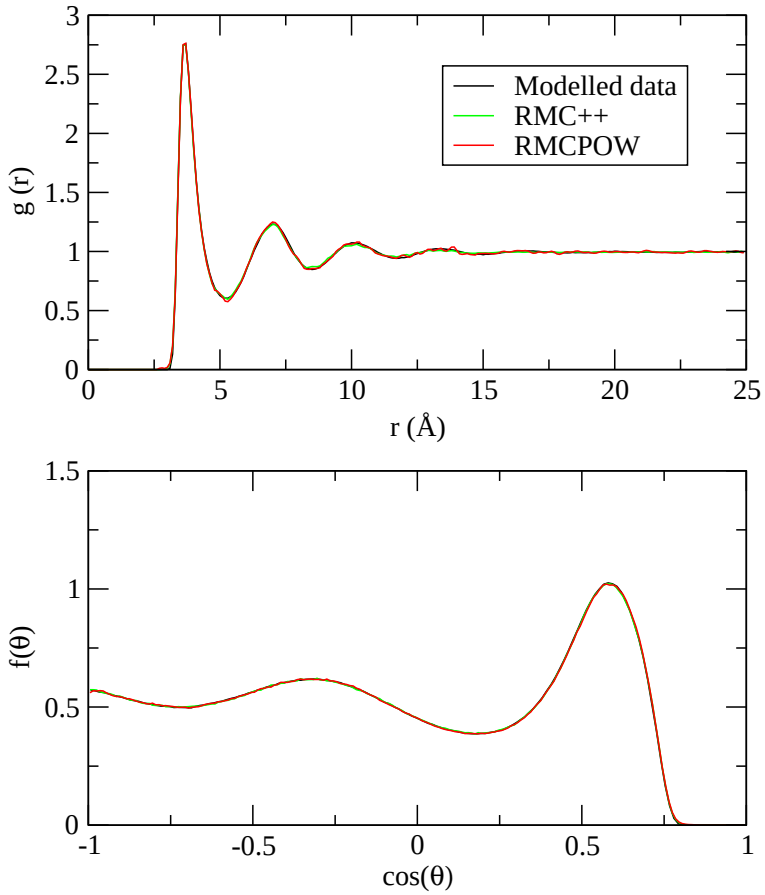

Figure 3.2: Comparison of the simulated radial distribution functions (top) and bond angle distribution functions (bottom) provided by canonical Monte Carlo simulations (black line), RMC++ (green line) and RMCPOW (red line) for liquid argon.

•Liquid gallium

In this case the agreement between the RMC++ and the RMCPOW radial distribution functions and bond angle distributions (see Fig.3.3) is almost perfect. Behind the good quality of the match of RDF-s and ADF-s one finds the considerably higher

experimental density of l-Ga in comparison with l-Ar (see table 4.1) and the wider Q range (up to 16Å^{-1}) and better quality of the neutron scattering measurement. As a consequence of the higher density for gallium, the two approaches yield smooth RDF and ADF simply using a simulation box of side 32Å.

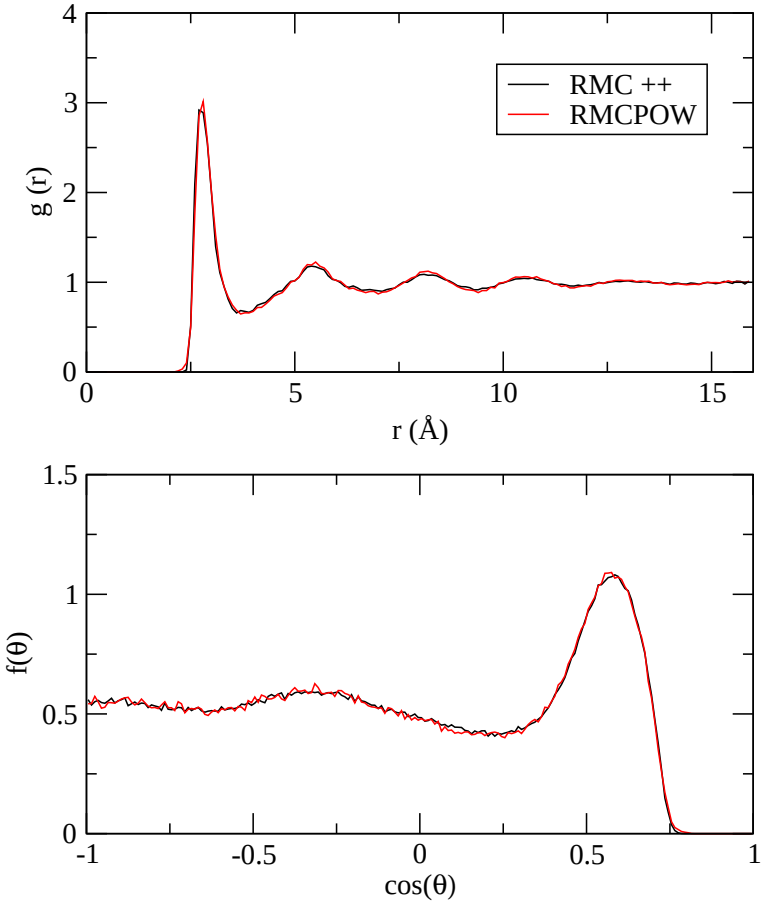

Figure 3.3: Comparison of the radial distribution function (top) and the bond angle distribution function (bottom) for liquid gallium.

•Liquid selenium

For l-Se, when comparing the radial and bond angle distribution functions in Figure 3.4, the overall good agreement is apparent, although the look of these functions is not as nice as it was for liquid gallium. A first glance at the RDF shows that the fluid is rather structured at short distance, because of the two covalent bonds of the atoms; this feature, however, does not seem to impose longer range ordering. The short period oscillations of the $g(r)$, again, are probably due to some residual systematic errors of the experimental $S(Q)$ [69].

For systems like liquid selenium, in which the short range $g(r)$ displays significant features, fine long range details of $S(Q)$ cannot be neglected. Also, the size of the simulation box affects to the accuracy of both approaches. By increasing the simulation box up to 50Åmore particle distances are included in the RDF calculation for method I and more reciprocal vectors are included in the evaluation of $S(Q)$ for

method II. This, in turn, implies both the use of a large system size that allows a finer sampling of r-space (method I) or Q-space (method II) and the inclusion of a rather long Q-range in the fitting procedure.

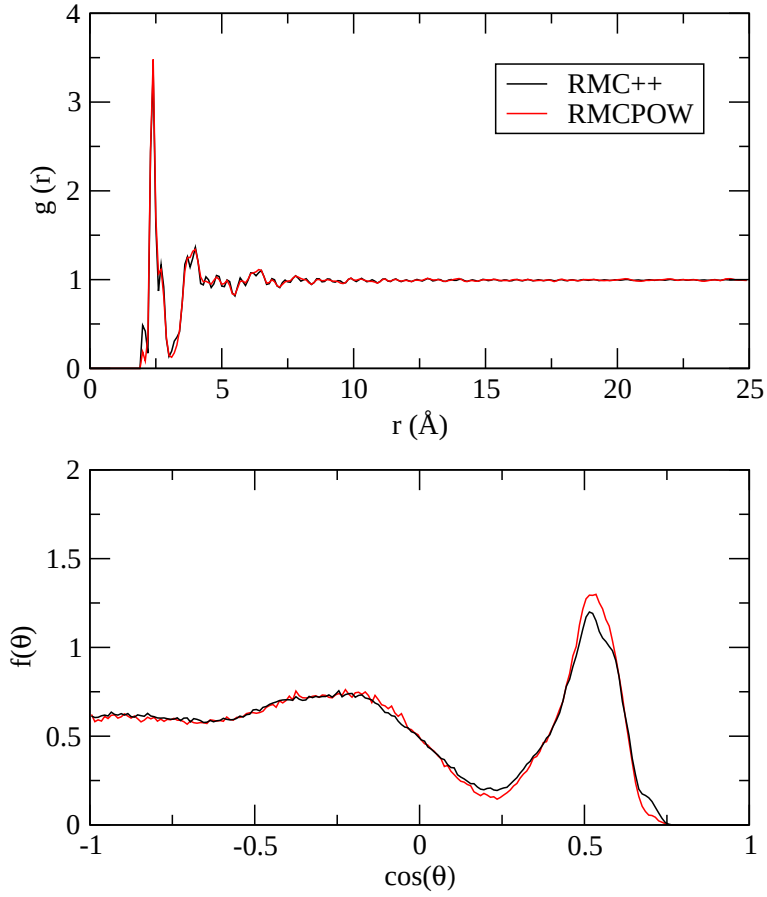

Figure 3.4: Comparison of the radial distribution function (top) and the bond angle distribution function (bottom) for liquid selenium.

The bond angle distributions are very similar, exhibiting maxima at the same angle values. The small difference for the maximum at 60 degree angle is not unexpected for a liquid with a relatively complex structure (twofold coordination and chain like structure). Only imposing some additional constrains, a reasonable good prediction for the three body correlations from a RMC simulation can be obtained for systems with this level of order.

•Amorphous silicon

The RMC++ and RMCPOW radial distribution functions (see Fig.3.5) agree very well; that is, the highest level of ordering among our test systems has not posed particular difficulties to either approaches. Interestingly, the main maximum of the RDF resulting from the '$g(r)$ route' is slightly sharper than its counterpart. Since the total scattering structure factors belonging to RMC++ and RMCPOW run together, it is not possible to assess which RDF is the 'real' one: one must accept that both (only very slightly different) $g(r)$-s are possible solutions. It would also be rather hard to consider differences in terms the ADF-s significant: it might just be

noticed that the unphysical maximum at the 60 degree angles is slightly stronger for the RMC++ solutions, whereas the 'real' maximum around the tetrahedral angle is very similar for the two approaches.

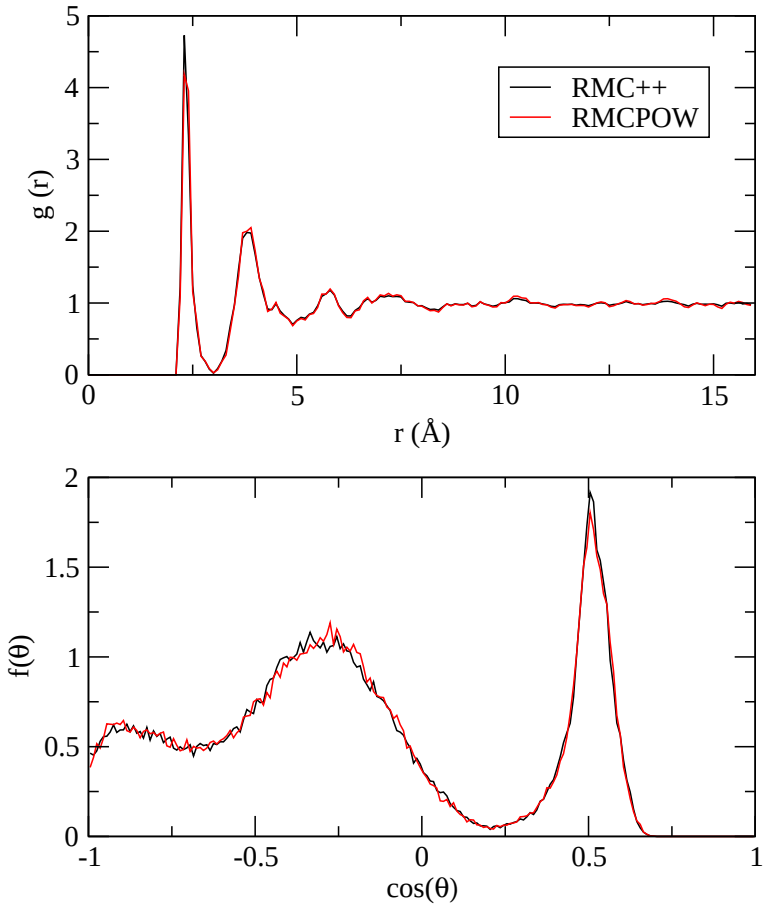

Figure 3.5: Comparison of the radial distribution function (top) and the bond angle distribution function (bottom) for amorphous silicon.

3.5 Summary and Conclusions

Two routes to the structure factor calculation implemented in the RMC++ [74, 60] and RMCPOW [35] algorithms have been considered. They have been successfully tested and compared on four model systems with different level of (dis)order. The agreement is almost perfect for simple (l-Ar) and non-covalent non-simple (l-Ga) liquids even for more ordered systems (l-Se and a-Si), only minor differences appear in terms of the RDF-s and ADF-s.

In terms of their relative efficiency, we found that the '$g(r)$ route' shows a considerably faster convergence, but it is exposed to Fourier truncation errors. Furthermore, this approach cannot be extended to deal with materials with Bragg scattering. In contrast, the 'crystallography' route can be used, at the expense of computational time, for a wide range of systems, from simple liquids to perfect crystals.

For two-phase systems of our future concern, porous crystalline materials with partially filled pores, i.e. in which crystalline and liquid/disordered phases are simultaneously present in the sample, the 'crystallography route' is the only approach. Out of the presently available software, the RMCPOW algorithm seems to be the most general choice; RMCProfile [58] may also be applicable of experimental data over extremely wide Q-range are available. This conclusion is also supported by a previous RMC study that showed that the 'crystallography route' provided an appropriate description of simple adsorbed fluids in zeolites, although in that case simulated target structure factors were used [5].

Acknowledgments

V.S.G and E.G.N. gratefully acknowledge the support from the Spanish MINECO (Ministry of Innovation and Economy) Grant No. FIS2010-15502 and FIS2013-47350-C5-4-R. V.S.G. also acknowledges the CSIC for support of his work by means of a JAE program Ph.D. fellowship. L.T. an L.P. are grateful for the financial support provided by Grant No. 083529 of the Hungarian National Basic Research Fund (OTKA).

Chapter 4

Reverse Monte Carlo modeling in confined systems

J. Chem. Phys., **140**, 024504 (2014)

Vicente Sánchez-Gil[1], Eva G. Noya[1] and E. Lomba[1]

[1] *Instituto de Química Física Rocasolano, Consejo Superior de Investigaciones Científicas, CSIC, Calle Serrano 119, 28006 Madrid, Spain*

Abstract

An extension of the well established Reverse Monte Carlo (RMC) method for modeling systems under close confinement has been developed. The method overcomes limitations induced by close confinement in systems such as fluids adsorbed in microporous materials. As a test of the method, we investigate a model system of ^{36}Ar adsorbed into two zeolites with significantly different pore sizes: Silicalite-I (a pure silica form of ZSM-5 zeolite, characterized by relatively narrow channels forming a 3D network) at partial and full loadings and siliceous Faujasite (which exhibits relatively wide channels and large cavities). The model systems are simulated using Grand Canonical Monte Carlo and, in each case, its structure factor is used as input for the proposed method, which shows a rapid convergence and yields an adsorbate microscopic structure in good agreement with that of the model system, even to the level of three body correlations, when these are induced by the confining media. The application to experimental systems is straightforward incorporating factors such as the experimental resolution and appropriate q-sampling, along the lines of previous experiences of RMC modeling of powder diffraction data including Bragg and diffuse scattering.

4.1 Introduction

Neutron and X-ray scattering techniques have been for years useful tools to gain a better understanding of adsorption processes[76, 63, 77, 78, 79], very specially in order to locate active sites and/or privileged positions for the adsorption of certain adsorbates. Given the small ratio between adsorbate/adsorbent molecules, and since in many instances the adsorbent exhibits a well defined crystalline structure, one can expect a diffraction pattern that will be dominated by long range order features. This situation recalls the problem of modeling powder diffraction data to account for lattice and magnetic disorder, which can be tackled by means of a Reverse Monte Carlo (RMC) approach by direct calculation of the structure factor[35]. As pointed out in Ref.[35], the well established Rietveld refinement for modeling crystalline systems and its variants mostly concentrate on the Bragg scattering whereas local disorder –which gives rise to diffuse scattering– is not considered. In the case of adsorption in crystalline microporous materials, the adsorbate molecules do not necessarily exhibit crystalline order. The Rietveld refinement can be applied using hand-tuning to a certain degree when the number of adsorbate particles per unit cell is relative low (see Refs.[78] and [79] for examples of hydrocarbon adsorption in Silicalite-I), and it is the approach of choice whenever the adsorbate+adsorbent sample is fully crystalline, in which case the single crystal method can be used (see e.g. Refs. [14, 80, 16, **?**]). This approach would be certainly impractical when there is a substantial degree of disorder.

In this work, we are interested in the elucidation of adsorbate structure in zeolites. These are materials with well defined microporous geometry, in which corner-sharing AlO_4 and SiO_4 tetrahedra form channels organized in 1D, 2D, and 3D networks accessible to different adsorbate molecules. The crystalline structure of standard zeolites is available from the literature[**?**], and adsorbates will induce changes in the diffraction spectra due to either modifications in the symmetry of the system or to the presence of disorder. From the discussion in the preceding paragraph, it might seem that the RMC approach of Mellegård and McGreevy [35], as implemented in the RMCPOW program[81] could be suitable to elucidate the microscopic structure of adsorbates in the present instance. There are however, a few aspects that suggest that a different approach is needed. Firstly, in many cases, the changes induced in the zeolite framework structure induced by the adsorbate are negligible (see however Refs. [14] and [16] as examples in which relatively large adsorbates modify the spatial group of the adsorbate). This implies that a substantial contribution to the structure factor remains unchanged. On the other hand, if one tries to blindly implement the standard Monte Carlo moves of ordinary RMC approaches (basically molecular translations and/or rotations, or spin rotations to model magnetic disorder[82]) to molecules under tight confinement, most of the moves will be rejected, by which the efficiency of the procedure will be extremely poor as compared with that obtained in regular fluids and glasses. The nature of our problem strongly suggests that the standard translation/rotation moves must be complemented with particle creation/annihilation attempts that allow an efficient sampling. It comes to our aid, that standard adsorption volumetry experiments[83] provide with relative accuracy estimates of the number of adsorbed molecules per unit cell of the adsorbent. Bearing in mind this information, it is possible to construct an efficient Reverse Monte Carlo procedure that can recover the microscopic structure of the adsorbed fluid

from powder diffraction spectra and adsorption volumetry experiments.

The aim of this work is to test the proposed approach, which we will denote by N-Reverse Monte Carlo (N-RMC) method for several model systems. The N-prefix underlies the fact that in this approach the number of particles, N, is one of the variables to optimize. For our testing purposes, we have generated the structure factor of ^{36}Ar adsorbed in two different zeolites, namely, Silicalite-I and siliceous Faujasite, by means of Grand Canonical Monte Carlo (GCMC) simulations at different loadings. Those systems have been studied experimentally by Llewellyn and coworkers[1, **?**] and it is known that can reliably be modeled using GCMC simulations[**?**, 84]. We will see how the proposed N-RMC approach, with the sole input of the relevant portion of the structure factor, the known zeolite structure, and an estimate of the number of adsorbate molecules per unit cell can accurately render the microscopic structure of the adsorbate in the course of a relatively short simulation run.

The rest of the paper is sketched as follows. The essentials of the method are introduced in Section 4.2. The most relevant results are commented upon in Section 4.3. Conclusions and future prospects are presented in Section 4.4.

4.2 Method

4.2.1 Implementation of the Reverse Monte Carlo method under confinement

As mentioned before, information about the microscopic structure of the adsorbed fluid can be obtained from neutron or X-ray powder diffraction measurements (see for example Ref. [63]). In the case of neutron powder diffraction, we will be dealing with an orientationally averaged structure factor[35]:

$$S(q) = \frac{2\pi^2}{NV < b >^2} \sum_{\mathbf{q}'} |F(\mathbf{q}')|^2 \delta(q - q')/q'^2 \tag{4.1}$$

where N and V are, respectively, the number of atoms and the volume of system (which in the case of a perfect crystal would reduce to those of the unit cell), $\mathbf{q}'$ are the allowed vectors in the reciprocal cell, and $< b >$ is the average of the coherent scattering lengths of the constituent atoms b_j. The $1/q'^2$ factor stems from the angular integration over all the possible $\mathbf{q}'$ orientations in the powder sample[35]. Finally, $F(\mathbf{q})$ contains the correlations between the scattering nuclei and is given by:

$$F(\mathbf{q}) = \sum_{j=1}^{N} b_j \exp(i\mathbf{q}\mathbf{R}_j) \tag{4.2}$$

where $\mathbf{R}_j$ denotes the position of the atom j in the unit cell. When dealing with real experimental data , the δ-function in Eq. (7.1) must be replaced by the instrument resolution function. As mentioned in Ref. [35] this can be any of the standard powder line shapes, e.g. a simple Gaussian distribution.

In many cases of interest the zeolite structure is hardly affected during the process of adsorption, and for practical purposes can be considered frozen. This is also a very common approximation in simulation studies[64]. Along these lines, in our calculation the positions of the zeolite constituent atoms will be kept frozen.

Consequently, its contribution to the total structure factor remains constant during the RMC simulation. From an experimental point of view, one typically measures the structure factor of the sample with and without adsorbate. Since in our case, the zeolite structure is well known, we will be working with the difference structure factor,

$$S_{diff}(q) = S_{total}(q) - S_{zeo-zeo}(q) \tag{4.3}$$

where $S_{zeo-zeo}$ is assumed to correspond to the empty sample. From Eq. (7.1) the total structure factor can be calculated in our case using the following expression:

$$S(q) = \frac{2\pi^2}{NV < b >^2} \sum_{\mathbf{q}'} \frac{1}{q'^2} \left| \sum_{j=1}^{N_{zeo}+N_{ad}} b_j \exp(i\mathbf{q}'\mathbf{R}_j) \right|^2 \delta(q - q') \tag{4.4}$$

where N_{zeo} is the number of atoms of the zeolite and N_{ad} is the number of adsorbed atoms. It is easy to see that the three partial contributions to the total structure factor can be calculated separately:

$$S_{zeo-zeo}(q) = \frac{2\pi^2}{NV < b >^2} \sum_{\mathbf{q}'} \frac{1}{q'^2} \left| \sum_{j=1}^{N_{zeo}} b_j \exp(i\mathbf{q}'\mathbf{R}_j) \right|^2 \delta(q - q') \tag{4.5}$$

$$S_{ad-ad}(q) = \frac{2\pi^2}{NV < b >^2} \sum_{\mathbf{q}'} \frac{1}{q'^2} \left| \sum_{j=1}^{N_{ad}} b_j \exp(i\mathbf{q}'\mathbf{R}_j) \right|^2 \delta(q - q') \tag{4.6}$$

$$\begin{aligned} S_{zeo-ad}(q) \;=\; & \frac{4\pi^2}{NV < b >^2} \sum_{\mathbf{q}'} \frac{1}{q'^2} \left[\left(\sum_{j=1}^{N_{ad}} b_j \cos(\mathbf{q}'\mathbf{R}_j) \right) \left(\sum_{j=1}^{N_{zeo}} b_j \cos(\mathbf{q}'\mathbf{R}_j) \right) \right. \\ & \left. + \left(\sum_{j=1}^{N_{ad}} b_j \sin(\mathbf{q}'\mathbf{R}_j) \right) \left(\sum_{j=1}^{N_{zeo}} b_j \sin(\mathbf{q}'\mathbf{R}_j) \right) \right] \delta(q - q') \end{aligned} \tag{4.7}$$

As mentioned, we will only calculate the relevant contribution S_{diff} –Eq.(4.3)– just adding Eqs.(4.6) and (4.7). Note, however, that in some cases the zeolite can undergo structural changes upon the adsorption of some molecules (usually big aromatic molecules) [80, 14, 16]. Obviously, in those cases the zeolite-zeolite contribution must be explicitly taken into account.

The core of the RMC method reduces to performing random particle moves that are accepted or rejected depending on whether the newly generated trial structure of the fluid (measured in terms of the pair distribution function, $g(r)$, or the structure factor, $S(q)$) approaches a target structure (usually an experimental $g(r)$ or $S(q)$). In the particular case that $S(q)$ is the reference property, the deviation from the target structure is measured using the statistical quantity,

$$\chi^2 = \sum_{i=1}^{N_q} \frac{(S_{calc}(q_i) - S_{exp}(q_i))^2}{\sigma^2(q_i)} \tag{4.8}$$

where the sum runs over the N_q discrete values of the wave vector q_i for which the structure factor $S(q)$ is evaluated, and $\sigma(q_i)$ is the standard deviation of $S_{exp}(q_i)$, that takes into account that experimental data carry different statistical uncertainties depending on the q-range of the measurements. In the standard RMC approach we

will be dealing with translational or rotational trial movements. Following Ref. [85], the minimization of χ^2 can be accomplished when the particle moves are accepted according to a probability given by

$$P^{acc} = \min\left(1, \exp\left(-\frac{\chi^2_{new} - \chi^2_{old}}{2}\right)\right) \tag{4.9}$$

where χ_{new} and χ_{old} are the values of χ after and before the trial move. In common with other optimization techniques such as simulating annealing and standard canonical Monte Carlo (that minimizes the system's internal energy), moves that worsen χ^2 can also be accepted as long as they comply with the probability distribution (4.9). In this way, the configurational space is adequately sampled and chances for the procedure to get trapped in local minima are greatly reduced.

Now, focusing on the problem of a system of tightly confined particles, as is the case of adsorbates in zeolite channels, an obvious problem with the scheme above described is the fact that most translational moves (and rotations in the case of molecules) will be rejected, due to overlaps with the zeolite framework. This means that, even if we are careful enough to generate an initial configuration of non-overlapping adsorbate molecules, the very low diffusivity within the channels and the high anisotropy of the medium, would render the standard RMC method inefficient. Our approach to speed up the sampling consists on starting from the empty zeolite and, in addition to the usual translational moves, also incorporate particle insertion and deletion trials. The number of sample particles can be estimated from a variety of experimental sources, for example, from volumetric adsorption experiments, and in standard RMC simulations is kept constant. In our approach, the acceptance rule is modified so that besides the minimization of χ^2, a constraint on the target number of adsorbed particles, N_{exp}, is also included:

$$P^{acc} = \min\left(1, \exp\left(-\frac{\chi^2_{new} - \chi^2_{old}}{2} - \frac{\Delta N^2_{new} - \Delta N^2_{old}}{2}\right)\right), \tag{4.10}$$

where $\Delta N^2 = (N - N_{exp})^2/\sigma_N^2$, N being the instantaneous number of adsorbed particles and σ_N the experimental uncertainty in N_{exp}.

In this work the target $S(q)$ and N_{exp} will be obtained from GCMC simulations rather than from experiments and, therefore, both the target structure factor and the number of particles are accurately known. However, we would like to explore the effect of their uncertainties on the performance of the method. For that purpose we carried out simulations for several values of σ_N and $\sigma(q_i) = \sigma_S$, $\forall i$. For simplicity, we have chosen that the uncertainty is the same for any range of q, but in real experiments this is not necessarily so. Note that the uncertainties play a similar role to the temperature in usual MC simulations, i.e. σ_S and σ_N control the equilibrium value and the magnitude of the allowed deviations of χ^2 and ΔN^2. The lower the value of σ_N the better the quality of the fit, but also the smaller the fluctuations allowed in χ^2; and the same applies to the number of particles N depending on the value of σ_N.

Due to the strong confinement effect imposed by the zeolite, insertion and deletion moves are crucial to avoid the trapping of adsorbed atoms in particular regions of the zeolite and therefore, will play a key role to sample efficiently the configurational space. Additionally, the performance of the RMC in confined media can be

much improved by imposing a bias in the insertion moves so that insertions are only attempted on those regions of the zeolite accessible to the adsorbate [20]. This is sufficient in our case (a monoatomic adsorbate), but when dealing with more complex adsorbates, such as chain or aromatic molecules, more sophisticated moves are needed. This is the same problem that one encounters in MC simulations of complex molecules in tightly confined media or at high densities. It can be tackled by using configurational bias moves[86] that have been designed to greatly enhance the performance of sampling in the case of molecules with important steric constraints (see Refs. [20, **?**] for a comparison of the acceptance probability of purely random and various types of biased displacement/insertion schemes in MC simulations).

Finally, as usual in the RMC method one has to define an exclusion core around each of the sample particles. This core, that reflects the effective size of the particle is needed in order to avoid unphysical overlaps, either between the adsorbates or between the adsorbed atoms and the zeolite framework. In our case, since we are dealing with model Lennard-Jones particles this quantity can be defined rather easily. Similar to the usual RMC other constraints can be applied, for example, a constraint on the adsorbate coordination number if many-body effects are known to be important[87]. In the examples studied here, many-body effects arise exclusively from the external field imposed from the zeolite rather than from adsorbate-adsorbate interactions. The target structure factor was obtained from MC simulations in which Ar-Ar interactions are simple pairwise Lennard-Jones potentials. In the case of bulk systems interacting via pairwise potentials, it is known that the knowledge of the pair distribution function determines uniquely the pair potential[**?**]. Thus one should expect that in the particular instance of pairwise interacting systems reproducing the pair structure will guarantee an accurate representation of higher order correlation functions without further constraints in the RMC procedure. One must note however that in our case, effective many-body effects on the Ar-Ar correlations are at play through the external confining field. So the uniqueness of the structural resolution would be in question, except for the fact that in the case of zeolites the structure of the confining medium and its corresponding field are accurately known. With this in mind, there will be no need to impose extra constraints on the procedure, as it will be illustrated below.

4.2.2 Simulation details

As mentioned, in order to assess the validity of the N-RMC approach to study the structure of fluids under confinement, we have considered as test cases the adsorption of argon in two zeolites with significantly different pore sizes, namely, Silicalite-I that is formed by a network of straight and sinusoidal pores of diameter of about 5-5.5 Å, and siliceous Faujasite that presents quite large cavities with diameters of about 11.5 Å. The first system was studied experimentally[63] by means of adsorption and neutron scattering experiments. Nonetheless, for our test purposes, we find more convenient to generate the "experimental" structure factor from a GCMC simulation. In this way, the target structure is accurately known and we have access to all microscopic structural quantities of relevance to compare with[**?**]. Obviously this substantially simplifies the problem, removing the experimental data treatment from the picture, or the incorporation of the instrument resolution function (which should replace the δ-function is Eq. (7.1)), and the appropriate treatment of the

discrete sampling of **q**-space[35]. In our case we will be comparing $S(q)$'s generated using identical simulation cells, by which all these subtleties can be omitted. Obviously, this will not be the case when dealing with real experimental data.

Explicitly, both in the GCMC and the N-RMC we have used a simulation box that contains 4×4×6 unit cells of the orthorhombic Silicalite-I[14] and 4×4×4 for the Faujasite (see the structures of these zeolites in Figure 4.1). In the GCMC both the oxygen atoms in the zeolite and the argon atoms are modeled using Lennard-Jones interactions. The parameters of the LJ model were chosen from the bibliography[88] and are given in Table 4.1. Silicon atoms are surrounded by oxygen tetrahedra and therefore it is common not to assign a Lennard-Jones (LJ) center to them. We used periodic boundary conditions and the LJ potential was truncated at a distance of 13 Å. GCMC simulations of argon adsorption were performed at 77K and in Silicalite-I at two different pressures that lead respectively to loadings of about 25.5 and 32 argon atoms per unit cell, the latter corresponding to saturation. In Faujasite the study was performed at a pressure corresponding to an intermediate loading of about 100 argon atoms per unit cell.

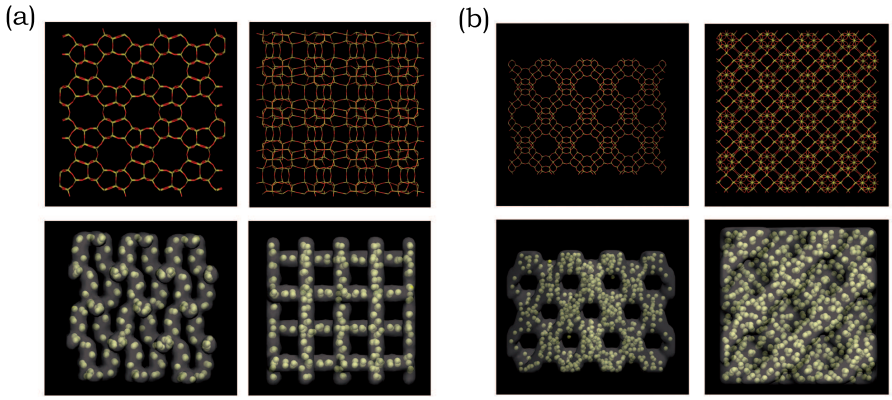

Figure 4.1: Structure of the two zeolites considered in this work: (a) Silicalite-I and (b) Faujasite. In each case, the two top panels show two different views of the zeolite structure and the two bottom panels show the volume of the channels in a grey shadow and the adsorbed molecules (at a loading of 32 atoms per unit cell in the case of Silicalite-I, and 100 atoms per unit cell in the case of Faujasite). For clarity purposes this figure shows smaller systems that the one simulated in this work.

Table 4.1: Parameters of the Lennard-Jones model used for the argon-argon and argon-zeolite interactions.

	ϵ/k_B (K)	σ (Å)
Ar-Ar	119.8	3.405
Ar-O	117.2	3.121

The simulated structure factor (subtracting the zeolite-zeolite contribution) averaged over a GCMC simulation of about 100,000 MC cycles was used as the target

in the N-RMC run. Here one cycle is defined as N_{ad} particle translations attempts plus one insertion and one removal attempt. We have defined the particle size (or overlap distance) in the N-RMC as $\sigma_{\alpha\beta}(RMC) = 0.92\sigma_{\alpha\beta}$, (and $\sigma_{\alpha\beta}$ taken from Table I) taking into account that the distance of minimum approach of LJ particles is slightly less than the LJ σ parameter.

During the RMC simulation we monitored the evolution of χ^2 and the number of particles. As it can be seen in Fig. 4.2, at the beginning of the N-RMC run, the quantity χ^2 drops very rapidly whereas the number of atom increases, until both quantities reach a plateau and finally oscillate around an average value. The magnitude of the oscillations in χ^2 and ΔN^2 can be controlled by the factors σ_S and σ_N that appear in the acceptance probability given in Eq. (4.10).

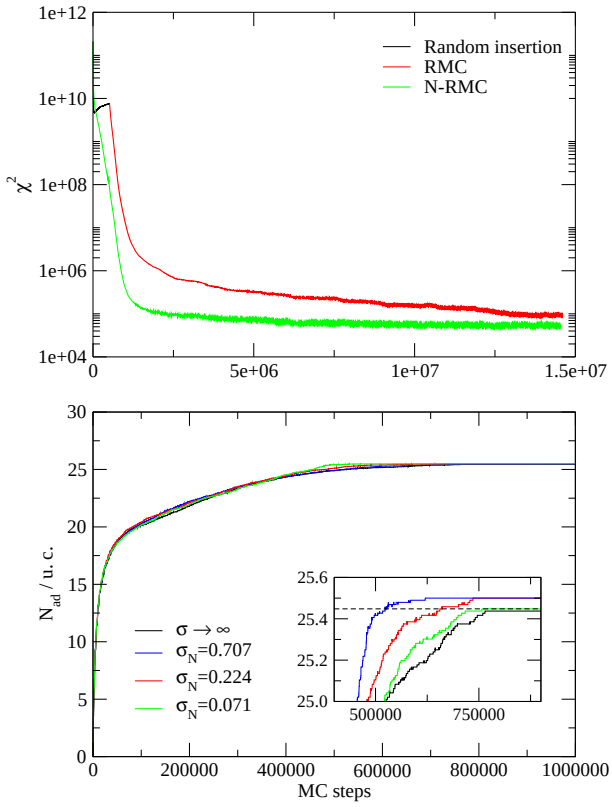

Figure 4.2: Evolution of χ^2 and the number of adsorbed particles N_{ad} per unit cell along the N-RMC simulation. The evolution of χ^2 with the usual RMC code is also shown for comparison. The black line shows the value of χ^2 during the random insertion of molecules used to generate the initial configuration for the usual RMC algorithm. Along with the evolution of the number of particles for the value of σ_N used in this work (shown in green), the results for other values of σ_N are also shown. The dashed black line in the inset shows the target N_{exp}.

In addition to the straightforward comparison of the target and the RMC simulated $S(q)$'s, in our case a better insight of the method's performance can be gained by inspecting the partial distribution functions and the three body correlation func-

tions. The partial distributions are defined as:

$$g_{\alpha\beta}(r) = \frac{n_{\alpha\beta}(r)}{\Delta V \rho_\alpha}, \tag{4.11}$$

where $n_{\alpha\beta}$ is the number of atoms of type β at a distance between r and $r + \Delta r$ of a central atom of type α, ΔV is the volume of a spherical shell between r and $r + \Delta r$, and ρ_α is the partial density of component α. We have calculated the adsorbent-adsorbent (Ar-Ar) and the adsorbent-adsorbate (Ar-O) partial distribution functions. No particular information can be extracted from the correlations involving Si atoms, since they all are buried within the framework tetrahedra formed by the oxygen atoms. In order to investigate the three body correlations we calculated the bond angle distribution, which is defined as the integral of the three body correlation function $g^{(3)}(r_1, r_2, \cos\theta)$ over the first coordination shell:

$$f(\theta) = 16\pi^2 \int_0^{r_c} \int_0^{r_c} r_{13}^2 dr_{13} r_{23}^2 dr_{23} g(r_{12}) g^{(3)}(r_{13}, r_{23}, \cos\theta), \tag{4.12}$$

where we chose r_c as the position of the first minimum of the pair distribution function. This function gives the distribution of angles between pairs of nearest neighbors with respect to a central atom. In this case we restricted our study to the bond angle distribution for argon triplets. From a practical point of view, this quantity will be evaluated from the ensemble average of $\cos\theta_{132}$ histograms corresponding to the 132 triplets of particles which fulfill $r_{13} < r_c$ and $r_{23} < r_c$.

4.3 Results

We will start presenting the results for argon adsorbed in Silicalite-I. For the case of a loading of about 25 molecules per unit cell and for the chosen values of the uncertainties, σ_S and σ_N, the N-RMC runs were fully converged after 10^7 MC steps (see Fig. 4.2). Initially the number of particles increased rapidly until it reached the experimental value after about 6×10^5 MC steps. Beyond this point the number of particles remains constant and particle insertion/deletion moves are no longer accepted. A potential enhancement of the algorithm would be the implementation of coupled insertion/deletion moves in which the former are guided by a cavity bias that takes into account the location of adsorbate molecules within the zeolite accessible volume. In the present instance this improvement has not been deemed necessary.

For the particular case studied here and for the chosen value of σ_N, the number of particles equilibrates exactly to N_{exp} for $\sigma_N = \sqrt{0.005} \approx 0.0707$. For larger values of σ_N the final number of particles is different (although not too far) from the experimental value. The fact that even when the constraint on the number of particles is not included (which corresponds to the case of $\sigma_N \to \infty$) the final number of particles is relatively close to the experimental one is related to the high accuracy in $S(q)$. Note, however, that when using experimental data which are subject to larger uncertainties, the deviation from the experimental number of particles will be quite large unless σ_N is given a value consistent with the experimental uncertainty. On the other hand, as mentioned before, the value of σ_S was chosen as a compromise between the quality of the fit of $S(q)$ and an efficient sampling of the configurational

space. Here we used $\sigma_S \approx \sqrt{(V\langle b\rangle^2)/(2\pi^2 \times 2 \times 10^5)}$. The effect of the choice of σ_S will be discussed in more detail below.

The evolution of χ^2 in the usual RMC method (which only includes displacement attempts) is also shown for comparison in Fig. 4.2. When using the usual RMC algorithm one needs a procedure to generate an initial configuration with the experimental number of adsorbed molecules, which can be obtained by random insertion of particles discarding those configurations that imply adsorbate-adsorbate or adsorbate-zeolite overlaps. In this work this procedure was accelerated by trying only insertions at positions of the zeolite accessible to the adsorbed particles. As it can be seen in Fig. 4.2, in this rather simple case that involves spherical particles and a moderate density of the adsorbed fluid, an initial configuration is obtained within about 5×10^5 MC steps. For more complex molecules, such as for example long chain alkanes, more sophisticated bias algorithms that enhance the probability of insertion of particles will be needed to generate an initial configuration in a reasonable amount of time[20, **?**]. The RMC simulation started from this quasi-random configuration, which exhibits a quite large value of χ^2, seems to be converging to the same value as the N-RMC method although at a much lower pace. Indeed, after 1.5×10^7 MC steps the RMC method has not reached equilibrium yet, the average value of χ^2 still decreasing. The lower convergence of the RMC method can be attributed to the low diffusion of the particles in the zeolite. Note that the N-RMC method needs a slightly larger number of steps to reach the experimental number of particles than the random insertion method. However, the value of χ^2 for the first configuration with N_{exp} molecules in the N-RMC, although still quite high, is about two orders of magnitude lower than when particles are inserted randomly, which indicates that particles are distributed already in a configuration much closer to the experimental one. The fact that virtually no particle exchange moves are accepted beyond this point indicates that indeed much of the diffusion problems are overcome already in the filling process in the N-RMC. It is quite remarkable that even for a simple system as that studied here the N-RMC method speeds up the convergence considerably with respect to the usual RMC method. As mentioned before, when dealing with complex molecules the use of biased insertion/deletion moves is essential to sample efficiently the phase space. In that instance the advantages of a N-RMC approach with respect to a RMC method with simple translational/rotational moves (if the latter is feasible at all) should be more apparent.

In Figure 4.3, the structure factor $S_{diff}(q)$ and its separate argon-argon and argon-zeolite contributions obtained from the N-RMC and the target GCMC $S(q)$'s for a loading of 25 argon atoms per unit cell are shown. The low-energy neutron scattering lengths have been taken from Ref. [**?**]. Note that the spiky appearance of both the target and fitted $S(q)$'s reflect the finite number of q-vectors sampled and that no experimental resolution function is taken into account. As mentioned before, all these factors must be explicitly incorporated in order to fit experimental data[35]. Along the N-RMC run, the number of particles rapidly converges to the experimental value (see Fig. 4.2), and the calculated and target $S(q)$'s are hardly distinguishable, the relative difference between the GCMC and N-RMC lying usually below 1% (obviously for very low intensity peaks relative errors can reach higher values, but this corresponds to very small absolute errors).

Besides the good quality of the fit of $S_{diff}(q)$, Figure 4.3 shows that the same applies to the fit of the partial structure factors (although the relative differences be-

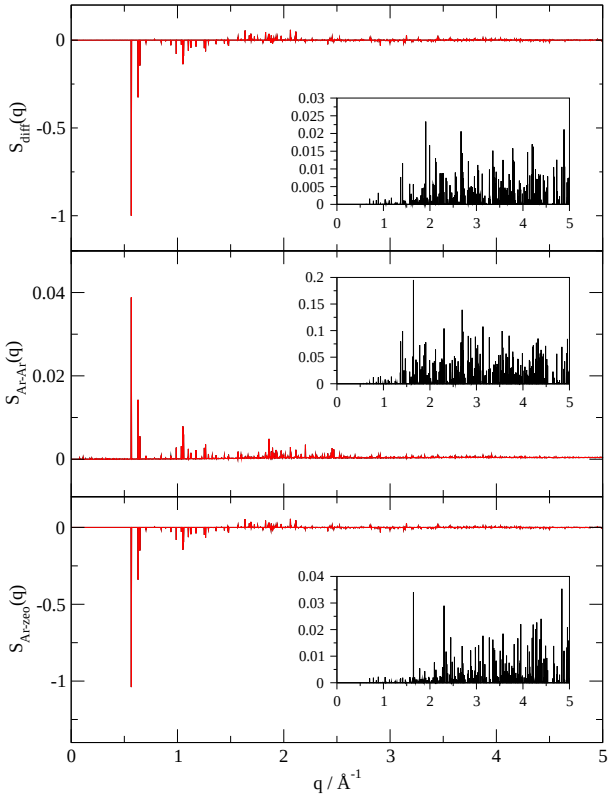

Figure 4.3: Comparison of the target GCMC (black line) structure factor and that obtained from the N-RMC (red line) in Silicalite-I at a loading of about 25.5 ^{36}Ar atoms per unit cell. Note that the zeolite-zeolite partial structure factor has been subtracted so that only the sum of the argon-argon and argon-zeolite partial structure factors are used in the fit. The two separate partial structure factors are also shown. The insets show the relative difference between the GCMC and N-RMC structure factors.

tween the target and calculated argon-argon partial structure factors are somewhat larger than in the other cases, which is a consequence of its much lower intensity). This is an important result, since when both components (4.6) and (4.7) enter into $S_{diff}(q)$ some of their features could average out, and hence a good agreement in $S_{diff}(q)$ does not necessarily imply the same for its partial components.

In order to get a better picture of the local order of the adsorbed fluid, and how this property is captured by the N-RMC approach, we analyze in Figures 4.4, 4.5 and 4.6 the corresponding partial distribution functions extracted from both the N-RMC and the GCMC simulations at the two adsorbate loadings in Silicalite-I (as an example of tight confinement) and Faujasite (as an example of a more loose confinement). The bulk Ar distribution function evaluated at the same temperature and at zero pressure is also shown for comparison. For Silicalite-I, a first glance at the distribution functions shows that the adsorbed fluid is very structured compared to the homogenous fluid, exhibiting order over quite long distances, this order being induced by the topology of the zeolite channels. Note, however, that despite the long range of correlations observed in Figs. 4.4 and 4.5, the sole intense peak corresponds

to the nearest neighbor shell, this peak being higher and narrower than in bulk Ar, as is typically the case for fluids confined in narrow porous systems. The second peak on the other hand is split in two, the splitting being more apparent for the higher loading. The remaining peaks have a much lower intensity, though they extend over a wider range of distances than in the bulk fluid. This is in marked contrast with the situation observed when dealing with much larger adsorbate molecules at high loading (see Ref.[89]), in which the adsorbed molecules are forced to occupy highly correlated positions in the framework channels, giving rise to much stronger interchannel adsorbate correlations. The argon-zeolite partial distribution functions are much less structured, reflecting the small ratio of Ar vs. oxygen atoms. In Faujasite, the larger size of the pores is reflected on a second fluid-like peak in the Ar-Ar distribution function that occurs at shorter distances than the second peak in the bulk case (see Fig. 4.6).

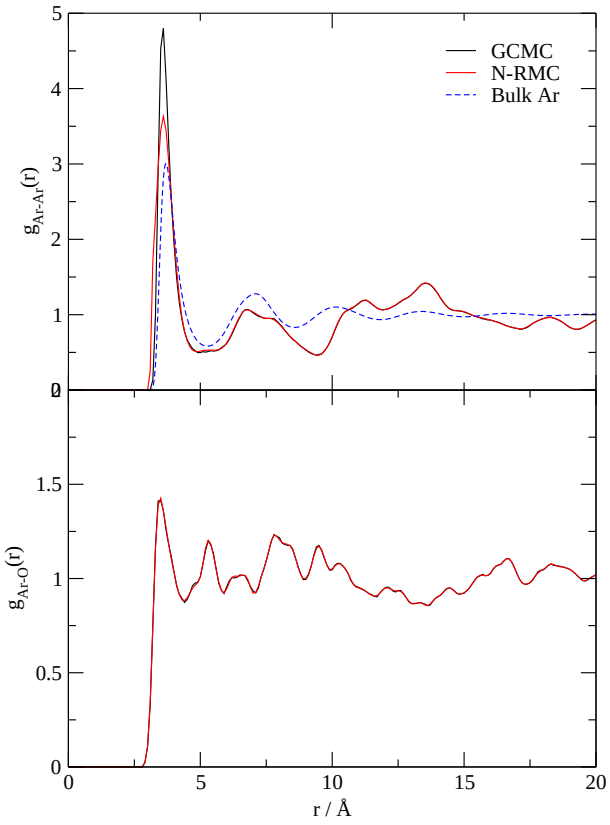

Figure 4.4: Comparison of the target (GCMC) and the *N*-RMC partial Ar-Ar and Ar-O pair distribution functions in Silicalite-I at a loading of 25.5 atoms per unit cell.

When comparing the *N*-RMC and GCMC partial distribution functions, the overall good agreement for both argon-argon and argon-oxygen correlations is readily apparent, both in Silicalite-I (at the two loadings) and in Faujasite. The small differences on the first peak of Ar-Ar distribution function arise due to the finite

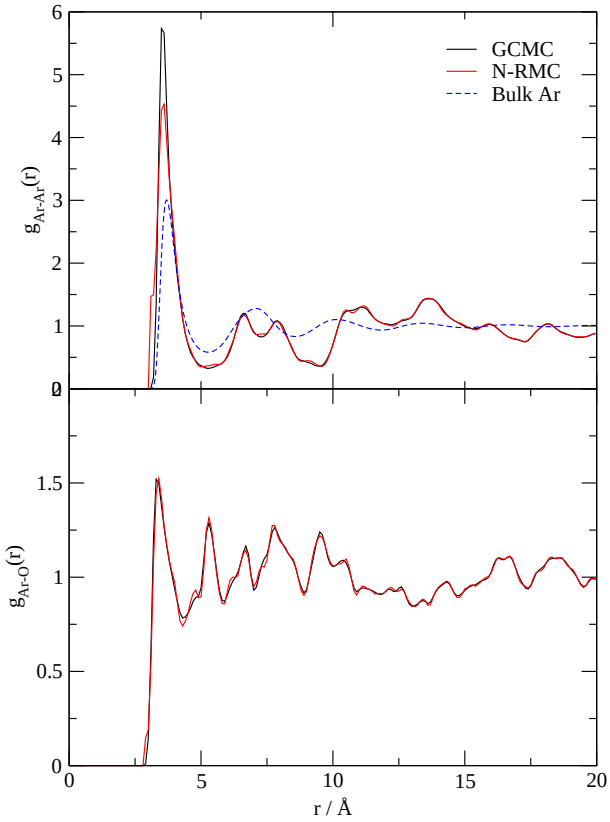

Figure 4.5: Comparison of the target (GCMC) and the N-RMC partial Ar-Ar and Ar-O pair distribution functions in Silicalite-I at a loading of 32 atoms per unit cell.

size of the simulation box. An accurate reproduction of the short-r behavior of $g(r)$ requires to have a detailed and accurate knowledge of the large q behavior of $S(q)$. This in turn implies both the use of a large system size that allows a finer sampling of q-space and the inclusion of a rather long q-range in the fitting procedure.

Discrepancies in the first peak are more evident in Silicalite-I, i.e., in the system with smaller pores that imposes a tighter confinement. This is not unexpected, a closer confinement leads to a more solid-like behavior of the adsorbed fluid and relevant features in the $S(q)$ extend to larger q than in systems with a more fluid-like behavior. Obviously a small uncertainty in $S(q)$, σ_S in Eq. 4.10, is also required to accurately reproduce the first peak in the partial distribution functions. As shown in Figure 4.7, χ^2 equilibrates to a lower value by decreasing σ_S, which means that the N-RMC $S(q)$ is closer to the target $S(q)$. As mentioned before, we chose a value that allowed us to sample the configurational space in a reasonable amount of time and at the same time produces a fairly good quality fit. We checked that the chosen value corresponds to a very small relative error of about 0.001 % for the most intense peak, whereas the relative error grows up to 1% for peaks with an intensity a thousand times smaller than the most intense peak. Experimental data usually have a larger statistical uncertainty of about a few percent (even in the more intense peaks). We checked the effect of a relative error on the target structure factor and found that the distribution function was still reproduced with a very good

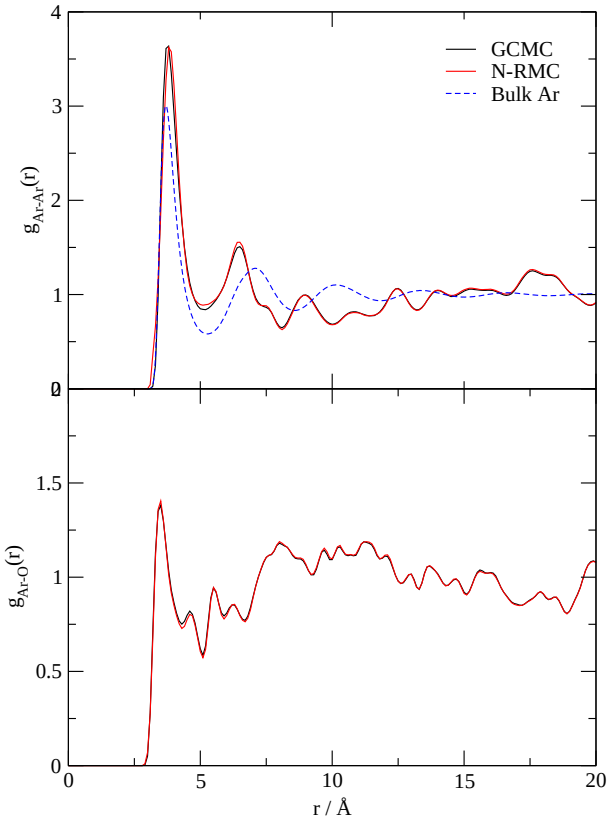

Figure 4.6: Comparison of the target (GCMC) and the *N*-RMC partial Ar-Ar and Ar-O pair distribution functions in Faujasite at a loading of about 100 atoms per unit cell.

accuracy. If any kind of medium-long range order builds up in the adsorbate within the zeolite, *N*-RMC should be able to provide an appropriate microscopic picture of it in consonance with the quality of the experimental data.

Further insight into the structure of the adsorbed fluid can be gained from the angular distribution function for triplets of argon atoms (see Figure 4.8 for Silicalite-I and Figure 4.9 for Faujasite). As mentioned before, we integrated the triplet correlation function up to the first minimum in the argon-argon partial distribution function (≈ 5Å). For Silicalite-I the bond angle distribution is similar at moderate and at high loadings, exhibiting peaks at roughly the same angles, but, as expected, the peaks are sharper at a high loading as a consequence of the higher density and reduced mobility of the adsorbed atoms. The two peaks at high angles reflect the tendency of the argon atoms to adopt local linear configurations imposed by the confinement in the channels of the zeolite. The GCMC and *N*-RMC bond angle distribution functions agree very well at both loadings except for some small discrepancies in the strong peak at short angles (these differences being connected to the small error in the first peak of the Ar-Ar pair distribution function). On the other hand, the bond angle distribution of Ar in Faujasite is more similar to the bulk LJ fluid, reflecting the larger pores in this zeolite. In this case the agreement between the GCMC and the *N*-RMC bond angle distribution is almost perfect. The

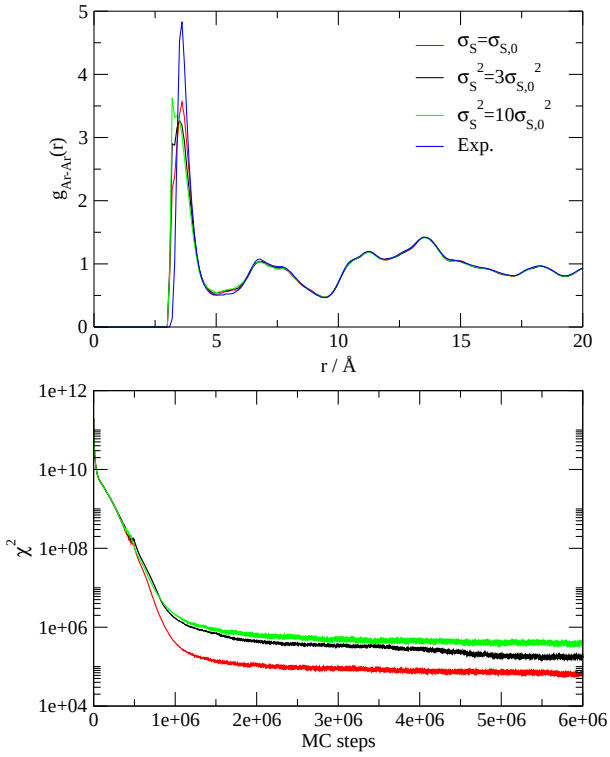

Figure 4.7: Effect of the σ_S parameter on the resulting pair distribution function (upper panel) and on the evolution of χ^2 with the MC step (lower panel) in the case of a loading of 25.5 atoms per unit cell in Silicalite-I. $\sigma_{S,0}$ corresponds to the value used in this work, $\sigma_{S,0} = \sqrt{(V\langle b\rangle^2)/(2\pi^2 \times 2 \times 10^5)}$.

correct prediction of the three body distribution function obtained here indicates that the RMC method is able to capture the three-body correlations induced mostly by the external field created by the confining medium. In our particular case the structure of the confining medium is accurately known. Obviously, in those instances where the intermolecular interactions of the adsorbate are strongly directional with a significant influence of three body forces (e.g. in the case of zeolite templated carbons[**?**]) additional constraints must be imposed along the RMC procedure, as it is customary in many RMC applications (see for instance Refs. [90, 91] for particular applications to disordered carbon materials). In any case, as shown for diatomic molecules and water, results obtained from RMC simulations need to be always interpreted with caution, as the correct description of the pair distribution function in real systems does not necessarily mean a good reproduction of the higher order distribution functions[**?**, **?**]. Nonetheless, as explained before, for tightly confined media, one would expect that geometric effects play a more significant role. In those instances, the N-RMC approach can be a very useful tool.

Before concluding we would like to comment on the range of q used to fit the $S(q)$. For the example presented here choosing a rather narrow range of q ($q \leq 5\mathring{A}$) was shown to be enough to obtain a very good description of the adsorbed fluid. Indeed, simulations including a broader range of q did not lead to a substantial improvement

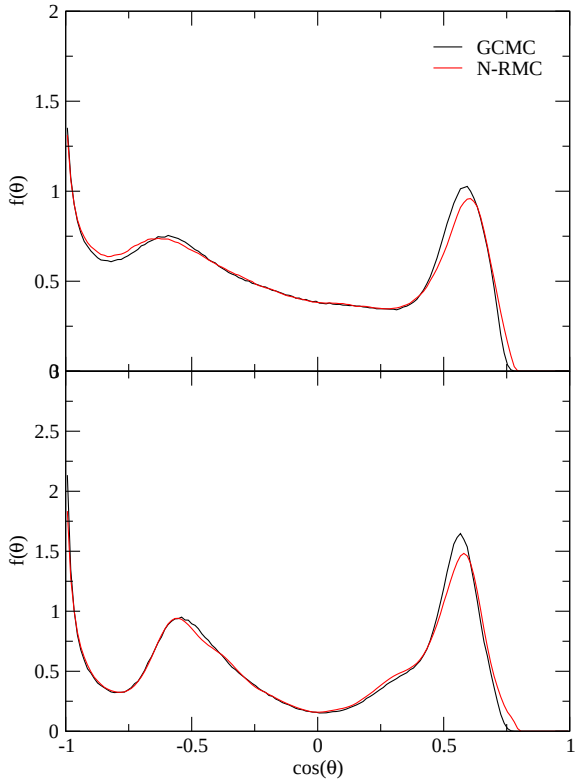

Figure 4.8: Comparison of the target (GCMC) and the N-RMC bond angle distribution function –Eq.(4.12)– for argon triplets at a loading of about 25.5 atoms per unit cell (top panel) and 32 atoms per unit cell (bottom panel) in Silicalite-I.

of the results. The correct sampling of the reciprocal space (by increasing the simulation box more reciprocal vectors are included in the evaluation of S(q)) had a higher impact on the quality of the results. The reason why including a higher range of q has little influence on the results is that oscillations in the target $S(q)$ practically die out for $q > 5\mathring{A}$ (see Fig. 4.3). This can be understood as the result of the relatively simple short range structure of the adsorbed Ar, which must be recalled is one of the simplest fluids in all respects. However, for systems in which the short range $g(r)$ displays significant features (e.g. due to intramolecular correlations), fine long range details of $S(q)$ cannot be neglected, and consequently a broader range of q must be included in the fitting procedure. When dealing with real systems, these data can be obtained from x-ray or neutron diffraction experiments, which currently allow to acquire fairly high resolution data up to quite large values of q.

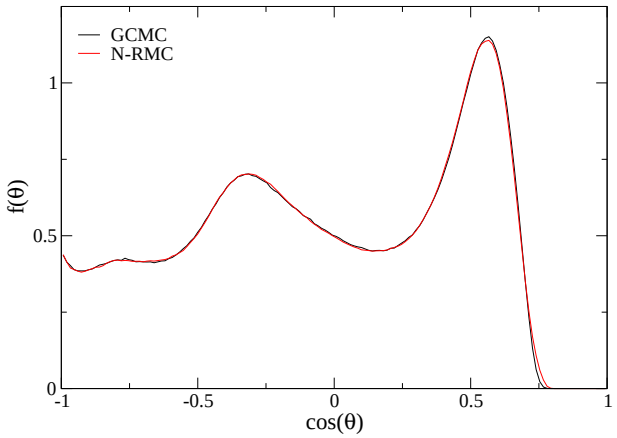

Figure 4.9: Comparison of the target (GCMC) and the N-RMC bond angle distribution function –Eq.(4.12)– for argon triplets at a loading of about 100 atoms per unit cell in Faujasite.

4.4 Conclusions

In summary, we have presented a simple extension of the Reverse Monte Carlo method that enables the determination of the microscopic structure of fluids under confinement. The success of our test case study of a monoatomic fluid adsorbed into two well known zeolites (Silicalite-I and Faujasite), evidences the performance of the proposed method. Our approach can easily be extended to other systems, even disordered porous materials, provided a previous study to determine the structure of the adsorbent material is performed as prerequisite. Complex molecular adsorbates can also be dealt with resorting to bias sampling techniques. In a forthcoming publication we will demonstrate the application of the method to determine the structure of adsorbed aromatic hydrocarbons in various zeolites using both X-ray diffraction data and volumetric and microcalorimetric adsorption experiments as input for the N-RMC.

Acknowledgments

The authors gratefully acknowledge the support from the Dirección General de Investigación Científica y Técnica under Grant No. FIS2010-15502 and from the Dirección General de Universidades e Investigación de la Comunidad de Madrid under Grant No. S2009/ESP/1691 and Program MODELICO-CM. The CSIC is also acknowledged for providing support in the form of the project PIE 201080E120. V.S.G. also acknowledges the CSIC for support of his work by means of a JAE program PhD fellowship.

Chapter 5

Adsorption of argon on pure silica MEL. Volumetric experiments and grand canonical Monte Carlo simulations

Micro. Meso. Mat., **222**, 218-225 (2016)

Vicente Sánchez-Gil[1], Eva G. Noya[1], José María Guil[1], Enrique Lomba[1] and Susana Valencia[2]

[1] *Instituto de Química Física Rocasolano, Consejo Superior de Investigaciones Científicas, CSIC, Calle Serrano 119, 28006 Madrid, Spain*

[2] *Instituto de Tecnología Química (UPV-CSIC), Avda. de los Naranjos s/n,E-46022 Valencia, Spain*

Abstract

The adsorption isotherm of argon on the zeolite MFI at liquid nitrogen temperature exhibits a sub-step at high loading before saturation that, in spite of much theoretical and experimental effort, is still lacking a definitive microscopic interpretation. In this work, we try to get insight into this peculiar behaviour by investigating the adsorption of argon on MEL, a zeolite that is structurally very similar to the MFI. First, we performed volumetric experiments that confirm that the adsorption of argon on MEL exhibits the same qualitative behaviour as on the MFI, again a sub-step appearing at high loading before saturation. Subsequently, the microscopic origin of this behaviour was investigated by means of molecular simulation. The simulations indicate that, for loads lower than that of the experimental sub-step, argon atoms can accommodate at low energy positions within the zeolite pores, whereas, above this point, some reordering of the adsorbate is needed to host further argon atoms. Moreover, the flexibility of the zeolite can have a significant impact on the shape of the adsorption isotherm, although the magnitude of this change depends on the zeolite model potential.

5.1 Introduction

The adsorption of simple gases on the zeolite silicalite-1 (pure silica MFI) has attracted considerable attention over the last three decades. This is mainly motivated by the observation that some of them, such as argon, krypton and nitrogen, exhibit one or several sub-steps in the adsorption isotherm at liquid nitrogen temperature [1, 2, 92]. Interestingly, the appearance of the sub-step can coincide with an exothermic signature in the heat of adsorption, as in the case of argon, or an endothermic one, as for krypton [1, 2]. This suggests that the microscopic origin of the sub-step might be different in these two cases.

For argon, the adsorption isotherm exhibits one step at loadings from about 20 to 25 atoms per unit cell [1, 24]. Two main hypothesis have been put forward to explain the origin of this behaviour. According to the first one, the sub-step appears as a result of a liquid–solid-like transition of the adsorbate induced by the confinement [1]. This possibility is supported by the emergence of a number of high intensity peaks on the neutron diffraction patterns after the sub-step. Other authors argue that the sub-step is caused by a structural change of the zeolite [93]. The MFI zeolite is known to undergo reversible structural changes upon increasing the temperature or by adsorption of big aromatic molecules. Specifically, at low temperature the MFI adopts a monoclinic structure [15] which, above 380 K, transforms into an orthorhombic cell with group symmetry *Pnma* [14] or, upon the adsorption of p-xylene, into the so-called PARA configuration with group symmetry $P2_12_12_1$ [80]. The splitting of some diffraction peaks after the sub-step might be indicative of such zeolite structural change [94, 95].

Simulations using different argon models (including even three-body contributions [96]) and keeping the zeolite framework rigid, were not able to quantitatively reproduce the experimental adsorption behaviour. In some cases, they yield smooth isotherms without any sub-step and, in other cases, they predict a jump in the adsorption, but at pressures several orders of magnitude higher than in experiments [93, 95, 97]. Furthermore, simulated diffraction patterns were not able to reproduce the appearance of all the experimental peaks after the step. This could mean that the adsorbate is less ordered in the simulations than in the experiments. However, it could also be indicating a zeolite structural change, a feature that, obviously, cannot be captured by simulations using a rigid framework. More recently, García-Pérez *et al.* [24] revisited these simulations, but explicitly incorporating the flexibility of the zeolite, an effect that had long been neglected in previous studies. This approach led to a more faithful description of the adsorption isotherm, from which the authors concluded that the sub-step was due to a combined effect of a structural change of the zeolite and of the adsorbate. However, a detailed description of those atomic structural changes is still lacking.

In this work, we will further investigate this phenomenon from a different perspective, which is by focusing on the related pure silica MEL zeolite, structurally very similar to the MFI but somewhat simpler (see Fig. 5.1). In particular, the MFI framework consists of parallel straight cylindrical pores that are intersected by sinusoidal channels, exhibiting four of that intersections per unit cell. The MEL zeolite exhibits a very similar structure, with the only difference being that in this zeolite all the channels are straight and, consequently, its unit cell has a higher symmetry (with space group I-4m2) [11]. In addition to that, there are experimental evidences

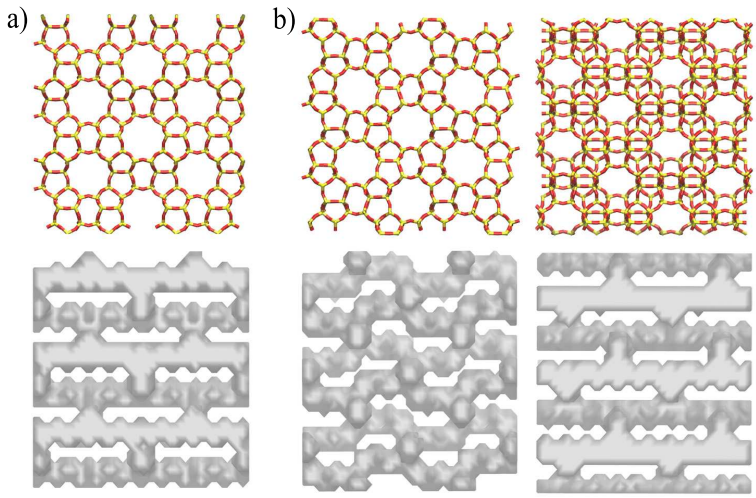

Figure 5.1: Structure of the a) MEL and b) MFI zeolite frameworks. Two different views are shown for the MFI. The volume accessible to the argon atoms is shown in the bottom figures.

that, similarly to MFI, MEL might also undergo a structural change upon increasing the temperature (at roughly 320 K) [98, 99, 100]. However, as far as we know, such structural transformation has not yet been fully characterized [11]. Given the structural similarity between both zeolites, it seems reasonable to think that both of them should exhibit a similar adsorption behavior.

5.2 Experimental procedure

Measurements were performed on an expressly synthesized pure silica ZSM-11 sample. Details of the synthesis of the ZSM-11(Si) sample are reported elsewhere [101]. In a previous work, using the "t"-method, we estimated that the micropore volume of the sample was 0.12 cm^3/g. [101]. This value is agreement with the literature [**?**, **?**]. High purity Ar (99.999%, Air Liquide, Spain) was used as adsorbate.

Adsorption volumetry

In an adsorption experiment, small doses of Ar were successively added at increasing pressures, measuring the increment of amount adsorbed to obtain the volumetric isotherm, $n^\sigma - p$. The amount adsorbed, n^σ, was determined in a volumetric apparatus, equipped with two pressure transducers (Baratron 310, MKS, USA) of 0-1.33 kPa and 0-133 kPa ranges, respectively. Dead volumes were determined by mercury weighting and helium expansions. Reproducibility in the measurement of amount adsorbed, determined by successive helium expansions, was better than 0.2 μmol.

Before each experiment the samples were heated in oxygen flow, c.a. 30 cm^3/min, up to 723 K, and kept at this temperature for 4 h to eliminate any organic residue. After that, the sample was out-gassed overnight at 723 K in a vacuum better than 1 mPa. All experiments were carried out at 77 K with the sample cell immersed in a boiling liquid nitrogen bath. Bath temperature was determined with a home made oxygen vapour pressure thermometer. Second virial coefficient correction was

applied to take into account the non-ideal behaviour of Ar vapour. For the case of argon this correction is negligible, but we still included it because it is our usual protocol for any adsorbent/adsorbate experiment. An experimental range of relative pressure, p/p_0, of 10^{-6} to 1 was covered in the measurements.

5.3 Modelling and simulation

Model potentials

In this work, interactions between argon atoms, and between argon and the zeolite, are described by the Lennard-Jones potential. The parameters for the argon-argon interaction are taken from Ref. [24], where they were fitted to the experimental liquid-vapour curve. The crossed argon-oxygen parameters were adjusted to reproduce the experimental adsorption isotherm, a usual approach in simulations of adsorption processes [24, 102]. Given that silicon atoms are caged inside oxygen tetrahedra, only the oxygen atoms are considered when evaluating the van der Waals interactions between the adsorbate and the zeolite. Interactions with silicon atoms are thus implicitly incorporated in the crossed oxygen-adsorbate interactions. The Ar-Ar and Ar-O parameters used in this work are summarized in Table 6.2.

Table 5.1: Parameters of the Lennard-Jones model used for the argon-argon and argon-zeolite interactions. For comparison, the parameters used in Ref. [24] to study the adsorption of argon on MFI are also provided.

	MEL (this work)		MFI (Ref. [24])	
	ϵ/k_B (K)	σ (Å)	ϵ/k_B (K)	σ (Å)
Ar-Ar	124.07	3.380	124.07	3.380
Ar-O	114.81	3.1265	107.69	3.150

As regards the zeolite intramolecular interactions, numerous model potentials can be found in the literature [25, 26, 103, 104, 105, 106, 107]. In this work, we focused on the popular models proposed by Demontis *et al.* [25] and by Nicholas *et al.* [26]. Our choice is motivated by a recent study that showed that both were able to reproduce reasonably well the experimental infrared spectra of a large variety of zeolites, including that of MEL [108]. In particular, the best results were obtained for the Nicholas model, that incorporates bonding, bending and torsional, as well as van der Waals and Coulombic non-bonded terms, and whose parameters were fitted to *ab initio* and experimental data [26]. On the other hand, the Demontis model is rather simple, including only bonding terms between the O-O and Si-O atoms. Surprisingly, it was found to perform better than more sophisticated models, such as that proposed by Hill and Sauer [104]. The parameters for the Demontis model were fitted to experimental structural data and the infrared spectrum of zeolite LTA, but numerous studies have proven its transferability to study properties of other zeolites [109, 108].

Besides using the original parameterization for these two models, we have also considered modified versions that, in what follows, will be designated as Nicholas modified and Demontis modified models, respectively. In those modified potentials, the equilibrium bond distances and bending angles, instead of being assigned

to constant values for all the bonded pairs and triplets as in the original parameterization, are taken from the experimental structural data of the zeolite under investigation [11]. Note that the nearest neighbours' bond distances and angles show some dispersion in the experimental unit cell. For example, for MEL, the probability distribution of the Si-O-Si bending angle is quite broad (see Table 5.2 and Fig. S1 in the Supplementary Material). This modification of the zeolite models has been commonly used in previous simulation studies [110, 111]. In the case of the Demontis model, this guarantees that the experimental structure corresponds to the energy minimum. This is not necessarily true for the Nicholas model as, in this case, there are also non-bonded terms that come into play. Indeed, simulations of the empty zeolite at 77 K, using both the original and modified versions of Nicholas model, yield average energies lower than that of the frozen experimental structure. In particular, for the original model, the energy of the experimental structure was −89.40 kcal/mol, whereas the average energy at 77 K is −89.81 kcal/mol. Similarly, for the modified model, the energy of experimental structure is −89.83 kcal/mol, slightly higher than the average energy at 77 K, −89.96 kcal/mol. In both cases, the Coulombic contribution to the energy is responsible for the experimental structure not lying at the energy minimum.

Table 5.2: Equilibrium bond distances and bending angles for the zeolite model potentials considered in this work. For the modified versions of the models, bond distances and bending angles do not adopt constant values across the unit cell [11]. In this case, only the upper and lower bounds are provided.

	d_{Si-O} (Å)	$d_{O-(Si)-O}$ (Å)	$d_{Si-(O)-Si}$ (Å)	θ_{O-Si-O} (degrees)	$\theta_{Si-O-Si}$ (degrees)
Nicholas	1.61	—	3.1261	109.5	149.5
Nicholas mod.	1.565-1.623	—	3.033-3.164	106.3-112.7	144.9-172.5
Demontis	1.605	2.61786	—	—	—
Demontis mod.	1.565-1.623	2.563-2.655	—	—	—

To further investigate the effect of the modification of the model parameters on the structure of the empty zeolite, we also calculated the pair distribution functions and the bending angle distributions. We found that the four considered models, namely, the original and modified versions of Nicholas and Demontis potentials, yield very similar pair distribution functions (data not shown). Larger differences appear in the bending angle distributions (see Fig. S1 in the Supplementary Material). In particular, for the Si-O-Si bending angle, the distribution is significantly broader for the original models than for the modified versions. This broadening is seemingly unrealistic when compared to the distribution functions calculated with the experimental structure, even when considering the possible effect of thermal disorder (see Fig. S1 in the Supplementary Material). Focusing now on the differences between both models, the Nicholas model tends to preserve more faithfully the experimental Si-O-Si angles, exhibiting two clear peaks at approximately $\theta_{Si-O-Si} = 155°$ and $\theta_{Si-O-Si} = 170°$, the first peak having a shoulder at $\theta_{Si-O-Si} = 145°$. On the other hand, the modified Demontis model shows a tendency to widen the Si-O-Si angles, favouring values larger than 160°. This is simply due to the absence of constraints on these angles in this model.

Simulation details

The adsorption isotherms were numerically evaluated by means of Grand Canonical Monte Carlo (GCMC) simulations. The simulation box contained 2×2×3 replicas of the zeolite unit cell. We considered two structures for the rigid zeolite: one of them obtained from a measurement at room temperature [11] (below the hypothetical structural transition at 320 K), and the second one measured at 363 K [98] (i.e., above the transition). Periodic boundary conditions were used along the three dimensions of space. Ar-Ar and Ar-O interactions were truncated and shifted at 12 Å, whereas the zeolite-zeolite van der Waals and Coulombic non-bonded terms of the Nicholas model were truncated at 8.85 Å [26]. Long range contributions to the Coulombic interaction were evaluated using Ewald summation [18]. Typically, simulations consisted of about a million Monte Carlo (MC) cycles, plus another one hundred thousand for equilibration. We defined a MC cycle as 250 particle insertion/deletion attempts, plus 250 particle move attempts. For those simulations that incorporate the zeolite flexibility, one cycle includes also one movement attempt for each atom of the zeolite. A larger number of MC cycles was used at loadings close to saturation than at low loadings.

Besides evaluating the number of adsorbed atoms as a function of the pressure (or chemical potential), we also calculated the isosteric heat of adsorption, that measures the enthalpy change when a molecule in the gas phase is adsorbed into the porous material. Several approaches can be used in simulations to determine this quantity [112]. Here, we used the energy/particle fluctuations route, according to which the isosteric heat of adsorption is computed as:

$$q_{st} = RT - \langle U_g \rangle + \frac{\langle UN \rangle - \langle U \rangle \langle N \rangle}{\langle N^2 \rangle - \langle N \rangle^2} \tag{5.1}$$

where U is the total energy of the system (adsorbent plus adsorbate), N is the number of particles, R is the gas constant and T the temperature. The brackets indicate an ensemble average over a GCMC simulation. Assuming ideal gas behaviour, the potential energy of the gas phase U_g can be equated to zero in the previous expression for Ar atoms [31, 112].

Information about the distribution of the adsorbed atoms on the channels of the zeolite was obtained by evaluating the density profile along the x and y directions of space (that are chosen to be parallel to the directions of the channels of the zeolites). This quantity is simply defined by:

$$p_N(x) = \frac{n_{Ar}(x)}{\Delta x} \tag{5.2}$$

where $n_{Ar}(x)$ is the number of argon particles with x-coordinate between x and $x + \Delta x$, and analogously for the y direction.

5.4 Results

5.4.1 Experimental measurements

Two isotherms of Ar on pure silica MEL were measured at 77 K up to a relative pressure of unity, $p/p_0 = 1$. They are Type I+IV isotherms: an initial abrupt uptake

increase, followed by a right angle knee at very low relative pressures corresponding to the filling of the zeolite's micropores. Afterwards, a large plateau appears, followed by a hysteresis loop in the p/p_0 range of 0.3-1 (this zone not shown here); the latter indicates mesoporosity of wide diameter range in the zeolite intermicrocrystallite voids. Results at low relative pressures are presented in Fig. 5.2. Good reproducibility is seen when comparing both isotherms. The noise observed at very low coverage, in Henry's law region, is attributed to experimental dispersion. As a test of the experimental setup, we have also performed measurements for the MFI, for which there are abundant experimental data for comparison. As can be seen, our adsorption isotherm on MFI is in very good agreement with one of the most recently reported measurements [24]. On the other hand, for MEL, as far as we know, this is the first time that the adsorption isotherm for the whole range of pressures is provided. We are aware of only one previous measurement of Ar adsorption for ZSM-11 (whose composition was not pure silica) that was restricted to pressures below the sub-step that we observe at a loading of $\sim$ 24 molec./u.c. [113]. As shown in Fig. 5.2, the adsorption behaviour of Ar on the two zeolites is very similar, both exhibiting a sub-step at high loadings before saturation. The only significant differences are that MEL absorbs up to about 15% more Ar than MFI, both at the sub-step and at saturation, and that the sub-step occurs at a pressure about one order of magnitude higher. These differences can be interpreted using a simple geometric argument, as the diameters of the channels and intersections are somewhat larger in MEL than in MFI (5.19Å and 7.72Å for MEL and 4.46-4.70Å and 6.36Å for MFI), leading to a higher porous volume in MEL [114].

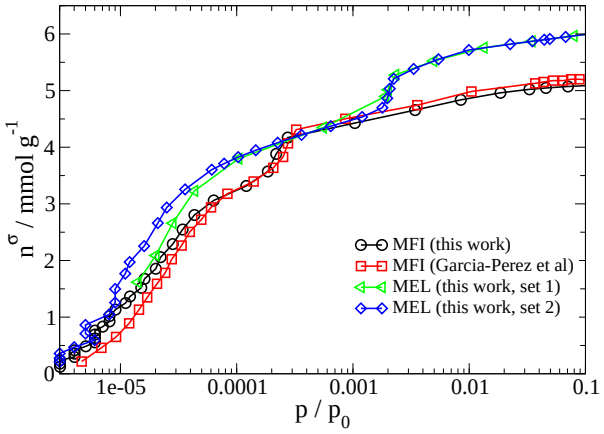

Figure 5.2: Experimental adsorption isotherm of Ar on MEL and MFI at 77 K. Results from Ref. [24] are also shown for comparison.

The fact that the same qualitative behaviour is found for both zeolites suggests a general mechanism that does not depend on the specific structural details of the pores. This is an interesting observation, as the origin of the sub-step at intermediate loading has often been attributed to the characteristic structure of the MFI framework with straight and sinusoidal channels [95, 79]. Here, we show that this phenomenon can also appear in the absence of sinusoidal channels.

5.4.2 Simulation results

The simulated adsorption isotherm of argon on MEL is compared to the experimental data in Fig. 5.3. The first observation is that simulations with a frozen framework are not able to quantitatively reproduce the experimental results. The simulated curve does not exhibit a clear sub-step at half loading. Instead, there is a change of slope at a loading of about $\sim$ 24 argon atoms per unit cell, after which the argon uptake occurs continuously without more abrupt changes up to saturation. Besides, the curve is very similar both when using the zeolite atomic coordinates measured at room temperature [11] and at high temperatures [98] (see Fig. 5.3).

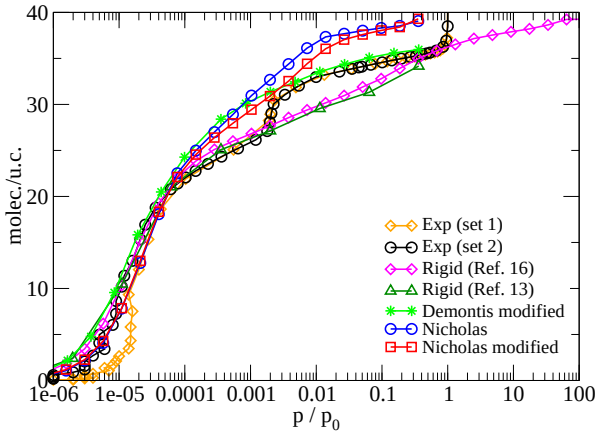

Figure 5.3: Simulated and experimental adsorption isotherms of Ar on MEL at 77 K.

Dubbeldam *et al.* [102] showed that the sub-steps in the adsorption isotherms are usually related to the accessibility of the adsorbate to different sites within the zeolite. As a consequence, their location, or even their appearance, can be tuned by modifying the size parameters of the crossed adsorbate–zeolite interactions. The energy strength can then be adjusted to match the experimental data at low loadings. Following these guidelines, we investigated the effect of the size parameter σ_{Ar-O} on the adsorption isotherm of Ar on MEL. Although we did observe a certain dependence of the slope in the region from half to high loading on σ_{Ar-O}, an abrupt jump similar to that found in experiments was never obtained (see Fig. S3 in the Supplementary Material). This is in line with the results obtained by García Pérez *et al.* [24], who also found that simulations with a frozen framework do not provide a satisfactory description of argon on the related MFI zeolite (either using the monoclinic or orthorhombic unit cells).

Our next step was then to incorporate the zeolite flexibility in the simulations. As can be seen in Fig. 5.3, the adsorption behaviour at low loadings and up to half loading (about 24 atoms per unit cell) is rather similar, regardless of whether the flexibility is included or not. However, in the region from half to high loading, all the flexible models predict a higher adsorption of argon than the rigid model at the same pressure. Note that the behaviour is also different depending on the model used to describe the flexibility of the zeolite.

Focusing first on the differences between the original and modified Nicholas mod-

els, both give rather similar results at low pressures. However, at a loading of about 24 molecules per unit cell, the uptake of argon with pressure becomes somewhat more moderate for the modified model, exhibiting a sub-step from about 30 to 37 atoms per unit cell. Comparing now these results to the experimental data, the shape of the sub-step for the modified Nicholas model is rather similar to the experimental one, although it appears at a loading significantly higher than in experiments.

Using a different functional form for the zeolite model has an even higher impact. Indeed, using the simpler modified Demontis model (whose geometric parameters are adjusted to the experimental structure of the MEL), the isotherm does not show any step at half loading, although, curiously, it quantitatively reproduces the experimental data, both at low loading and at saturation. Differences in the adsorption behaviour depending on the zeolite model have already been noted in previous studies (see, for example, Ref. [111]).

With the aim of trying to identify a possible structural change on the zeolite upon the adsorption of Ar in our simulations, we calculated the average positions of the framework atoms along simulations of the empty and full loaded zeolite. Comparison of those average structures by visual inspection showed only subtle differences between them (see Fig. S2 in the Supplementary Material). However, a better way to characterize the adsorption properties of these two average structures is to evaluate their adsorption isotherms by GCMC simulations (keeping the average structures frozen). Then, if the average structure of the fully loaded zeolite is able to absorb significantly more than that of the empty one, this would indicate a structural change in the zeolite. The results of these simulations are shown in Fig. 5.4. Surprisingly, for the modified Nicholas model (Fig. 5.4, top panel), the adsorption isotherms for both average structures (empty and fully loaded) are almost indistinguishable from that for the flexible model. This, together with the fact that the experimental atomic MEL structure is not an energy minimum for the modified Nicholas model, suggests that the adsorption isotherm for this flexible model differs from that for the rigid zeolite (using the experimental atomic coordinates), not because of the incorporation of flexibility, but, instead, because it slightly deforms the zeolite structure, seemingly opening somewhat the pores. Completely analogous results were obtained for the original Nicholas model (data not shown).

By performing the same study for the modified Demontis model (for which the experimental structure corresponds to the minimum of energy by construction), a completely different scenario is obtained. In this case, the adsorption isotherms for the average structures of the empty and fully loaded zeolite are very similar to that obtained using the rigid experimental structure and, thus, different from that for the flexible zeolite. Contrary to the the Nicholas model, the flexibility now plays an important role, changing the adsorption isotherm form above a loading of roughly 20 molec./u.c. However, the fact that the isotherm for the empty and fully loaded structures are almost indistinguishable, indicates that the atomic average positions are the same. This rules out the possibility of a structural transition upon the adsorption of Ar in the simulations with the modified Demontis model.

Taking all these results together, it is clear that none of the considered models is able to provide a full quantitative description of the experimental data. We think that this can be due both to a poor description of the flexibility of the zeolite upon the adsorption of the adsorbate, and to the need to improve the crossed Ar-zeolite interactions. In relation to the latter, even though MEL and MFI have the same

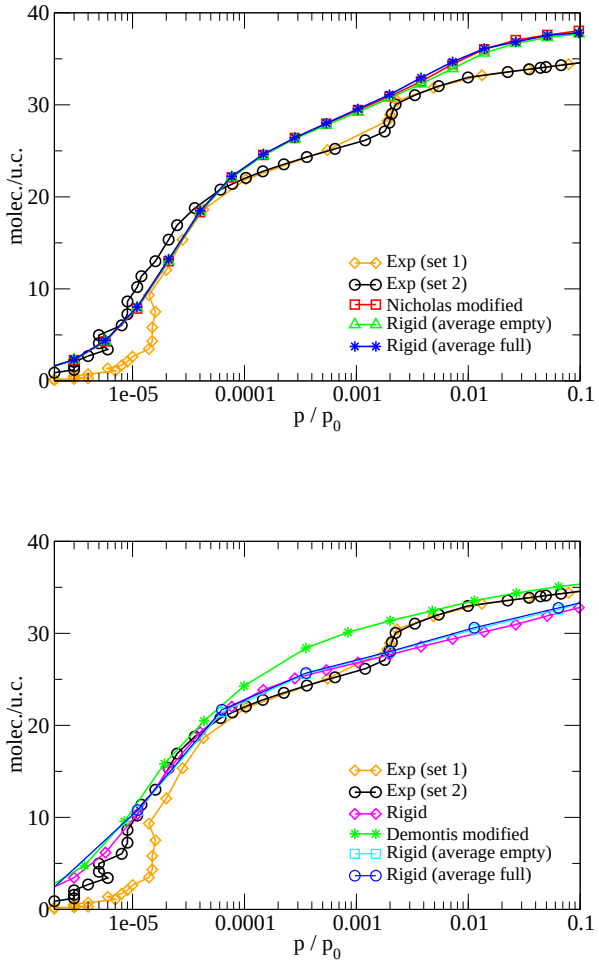

Figure 5.4: Adsorption isotherms of Ar on MEL at 77 K obtained from simulations using average structures of the zeolite along simulations of the empty and full loaded zeolite. The top panel shows the results using the average positions for the modified Nicholas model and the low panel for the modified Demontis model.

chemical composition (pure silica), the parameters fitted in Ref. [24] to reproduce the experimental isotherm of Ar on MFI do not describe properly the adsorption on MEL at low pressures (see Fig. S3 in the Supplementary Material). The fact that a different set of parameters has to be used for each of the zeolite models suggests that the functional form of the Lennard-Jones model does not reproduce properly the interaction between argon and the zeolite.

With the aim of providing a detailed description of the mechanism behind the simulated adsorption isotherms, we have analyzed the isosteric heat of adsorption and the distribution of the adsorbate atoms within the pores. To keep the discussion simple, we present only results for the rigid zeolite [11] and for the flexible zeolite described with the modified Demontis model, as this model predicts that flexibility plays an important role in the adsorption properties.

As can be seen in Fig. 5.5, the isosteric heat of adsorption is rather similar at low loadings regardless of whether the zeolite is rigid or flexible, increasing moderately

with the amount of adsorbed argon up to a loading of about 24 molecules per unit cell. By looking at the different contributions to the isosteric heat of adsorption, we can see that the Ar-Ar contribution increases in this region, simply because more Ar-Ar interactions come into play as the density of the adsorbate increases. On the other hand, the heat due to the Ar-zeolite contribution decreases, reflecting, in this case, that argon atoms occupy first the most energetically favourable positions within the zeolite pores and, once those are occupied, the new adsorbed atoms go to slightly less energetically favoured positions.

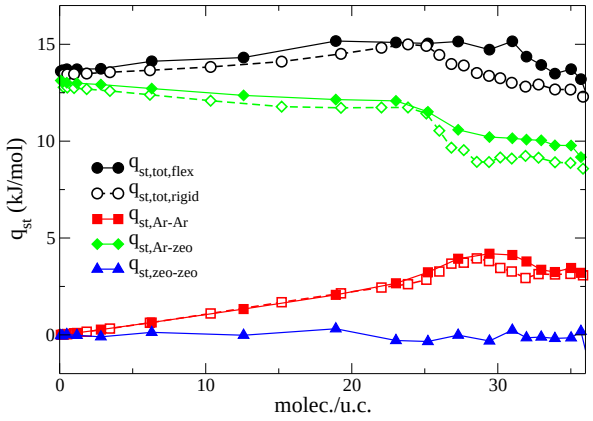

Figure 5.5: Isosteric heat of adsorption calculated for the rigid and the flexible zeolite modelled with the modified Demontis model. Full symbols and solid lines correspond to data from simulations for the flexible zeolite, whereas open symbols and dashed lines are for the rigid zeolite.

Visual inspection of the configurations reveals that, from very low loadings ($\sim 2-3$ atoms per unit cell), argon atoms are found both at the channels and at the intersections. At a loading of ~ 24 atoms per unit cell, we found two atoms per channel and other two at the junctions (note that there are 8 channels and 4 junctions per unit cell). A typical snapshot of the system at this loading is shown in Fig. 5.6. The distribution of the atoms within the pores can be quantified by calculating the density profiles along the directions parallel to the channels (Eq. 5.2). The profile along the x-direction, depicted in Fig. 5.6, is in agreement with the description just provided. It shows two peaks within the channels and a broader, more pronounced peak, at the positions of the intersections ($x \approx 0, 10, 20, 30$ Å). Note, however, that these peaks result from the addition of the contribution of the intersections as well as the perpendicular channels that run along the y-axis. As can be seen in Fig. 5.6, the distribution of the adsorbate is almost indistinguishable for the rigid and flexible zeolite cases.

The distribution of argon within the zeolite pores up to a loading of 24 molec./u.c. can be more clearly visualized in the probability map depicted in Fig. 5.7. This figure shows the Boltzmann factor ($\exp(-U/kT)$) for a probe argon atom at a $x-z$ cross section of the MEL zeolite. As can be seen, the most energetically favoured positions are located at the channels, with two sites with approximately the same probability per channel. In the junctions, there are another two regions with en-

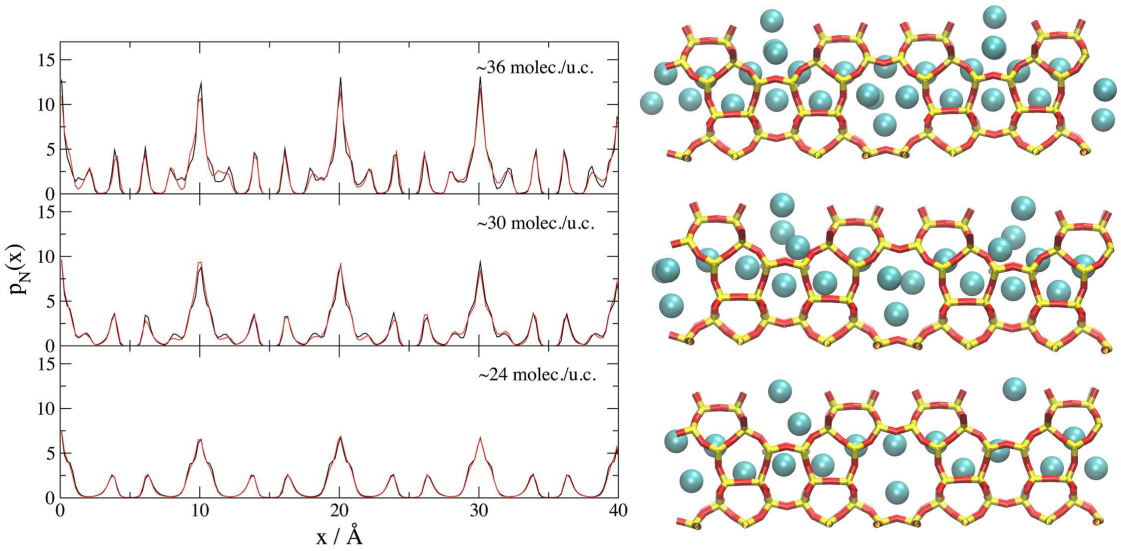

Figure 5.6: Density profile of Ar in the zeolite MEL along the x-axis at different loadings at 77 K. Density profiles along the y-axis are identical and for that reason are not shown. The black line shows the results for the simulations using a rigid zeolite framework, whereas the red line corresponds to simulations with the flexible modified Demontis model.

hanced probabilities, located at the top and bottom edges, the Boltzmann factor diminishing considerably at the center of the intersections. In all, there are 24 sites (2 in each of the 8 channels and another 2 in each of the 4 intersections) that exhibit a high occupation probability, so that the 24 first adsorbed molecules will go to sit preferentially around those locations. Given that those sites are sufficiently apart from each other, the argon atoms can be easily accommodated up to a loading of 24 atoms per unit cell, resulting in a net energy gain of the zeolite-argon system. At this loading, the isosteric heat presents a maximum that is coincident with a change of slope of the adsorption isotherm (see Fig. 5.3).

At higher loadings, differences between the results for the rigid and the flexible zeolite become evident, also in keeping with the distinct behaviour of the adsorption isotherm in this region. In the case of the rigid zeolite, the heat decreases for loadings higher than 24 atoms per unit cell. However, for the flexible zeolite, the curve remains roughly constant from about $\sim$ 24 molec./u.c. to $\sim$ 31 molec./u.c., after which undergoes a subtle drop. In the region between $\sim$ 24 to $\sim$ 28 atoms per unit cell, the different behaviour arises mainly from the Ar-zeolite contribution, as the Ar-Ar is rather similar for both the rigid and the flexible zeolite. The Ar-zeolite term undergoes a sudden decrease from $\sim$ 24 to $\sim$ 28 atoms per unit cell, this decrease being significantly more abrupt for the rigid zeolite. As can be seen in the probability map depicted in Fig. 5.7, once that 24 atoms per unit cell have been adsorbed, the unoccupied positions are no longer energetically favourable. As a result, the new argon atoms can only go to the available higher energetic positions (usually displacing a bit some of the previously loaded atoms to leave room for the extra load), causing the change of slope of the adsorption isotherm. Indeed, the distribution of argon atoms is rather similar when 24 or 28 argon atoms are

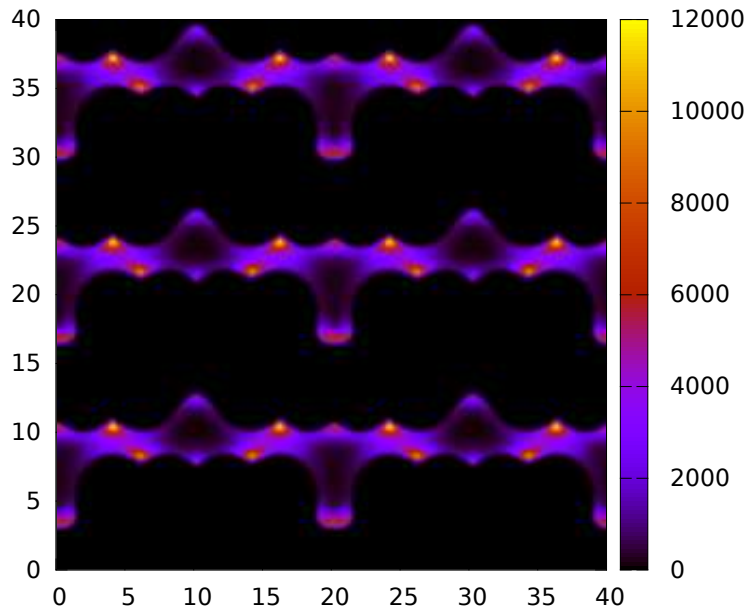

Figure 5.7: Boltzmann factor at a $x - z$ cross section intersecting the center of the channels. The zeolite was kept frozen to build this map.

adsorbed, the four extra atoms being placed at the intersections. The fact that the drop of the Ar-zeolite contribution is less pronounced for the flexible framework indicates that the atomic vibrations alleviate the energetic cost of inserting particles, i.e., subtle displacement of the atoms of the zeolite can lead to lower repulsions in the argon-zeolite interactions.

Beyond a loading of ~ 30 atoms per unit cell, differences between the rigid and the flexible zeolite extend also to the Ar-Ar contribution. Whereas this contribution starts to decrease at this point for the rigid zeolite, for the flexible framework it continues to increase up to a slightly higher loading ($\sim 32 - 33$ molec./u.c.), after which it also drops. This is just reflecting that the vibration of the zeolite can also lead to lower repulsion between the adsorbate atoms at high loadings.

In spite of the different energetics of the adsorption process, the distribution of the argon atoms within the pores is rather similar for both the rigid and the flexible zeolite (see Fig. 5.6). At a load of ~ 30 molec./u.c., the density profile again shows two peaks at the channels (that become narrower and taller than at ~ 24 molec./u.c., as a result of the lower mobility of the adsorbate at higher loads), whereas the peaks corresponding to the intersections develop two lower peaks, one at each side. A typical configuration is depicted in Fig. 5.6.

This tendency to host the extra atoms in the intersections extends up to saturation. The density profile at a load of ~ 36 molec./u.c. exhibits peaks at the same positions as that for ~ 30 molec./u.c., although, obviously, these peaks become even narrower and taller for loads close to saturation, indicating that the adsorbed fluid presents a solid-like behaviour. At these high loadings, the atoms tend to adopt highly ordered configurations imposed by the geometry of the zeolite pores. Specifically, the argon atoms are distributed in zig-zag configurations along the channels and up to 6 atoms can be packed at each intersection (see Fig. 5.6). In this way, the MEL can host up to 40 atoms per unit cell. However, this very high load is only

attained at unrealistically high pressures.

Curiously, the contribution to the isosteric heat arising from the zeolite flexibility is negligible at all coverages (only subtle oscillations are observed at high loading, a region more prone to statistical uncertainty). This means that the slight distortion of the zeolite framework to better accommodate the argon atoms occurs without a relevant energetic penalty. Note, however, that it is important to incorporate the flexibility, because it affects the Ar-Ar and Ar-zeolite contributions and, thus, the total isosteric heat, specially after the sub-step.

Focusing now on the differences between the structure of the adsorbed fluid, as mentioned before, the density profiles along the x-axis are rather similar for both the rigid and the flexible zeolite. Only minor changes are observed at the highest load, namely, ~ 36 molec./u.c.. In this case, the profile for the rigid zeolite exhibits somewhat sharper peaks, making evident the tighter confinement of the adsorbate when the adsorbent is kept frozen. Analysis of the Ar-Ar and Ar-O average pair distribution functions corroborate this view (see Fig. S4 in the Supplementary Material). Those curves are again very similar in both cases, the largest differences appearing for the Ar-O distributions, as expected. The Ar-Ar functions are very similar at all loadings, except for a slight sharpening of the peaks at the highest loadings. All these results evidence that the incorporation of the zeolite flexibility does not lead to significant changes in the structure of the adsorbate.

Unfortunately, we could not measure the isosteric heat of adsorption experimentally, so that a comparison between simulations and experiments is not possible in this case. However, given the similar adsorption isotherms for MFI and MEL, it is expected that the isosteric heat will behave similarly in both systems. According to the experimental data reported in Ref. [93], the heat of adsorption remains constant up to a loading of about $\sim 22 - 23$ molec./u.c. At that point, it suffers a rather abrupt increase, after which it remains again constant up to a loading of about $\sim 27 - 28$ molec./u.c. Assuming that the isosteric heat of adsorption of Ar on MEL may well exhibit a similar behaviour, the results using the flexible zeolite should then provide a better description of the experimental data.

5.5 Conclusions and outlook

To summarize, in this work, we have measured the experimental adsorption isotherm of argon into MEL zeolite. We find a sub-step at a loading of $\sim$24 argon molecules per unit cell, similar to that observed for the MFI framework (although, in this case, it appears at ~ 20 molec./u.c.). Our simulations indicate that the sub-step at half loading can simply originate from the occupation of different "energetic sites" within the pores. Initially, adsorbate atoms go to the most energetically favoured positions. Once all those sites are occupied, roughly at half loading, the new adsorbed argon molecules necessarily have to go to higher energy positions (often leading to small displacements of the already adsorbed atoms).

In addition, we have seen that the flexibility of the zeolite can have some influence on the energy of these less favourable sites and, as a consequence, also on the shape of the adsorption isotherm above half loading. However, different zeolite models attribute different relevance to flexibility. For the Nicholas model, flexibility does not seem to affect the adsorption isotherm. In this case, the experimental structure is not at the energy minimum and the zeolite structure is somewhat deformed. The change

in the adsorption properties is a consequence of this deformation of the zeolite, not of having incorporated the zeolite flexibility. On the contrary, the simpler Demontis model (for which the experimental structure corresponds to an energy minimum by construction) predicts that the explicit incorporation of zeolite flexibility does change the shape of the adsorption isotherm. Finally, we have also found that the structure of the adsorbate within the pores seems to be little influenced by the flexibility of the framework.

When comparing the simulated adsorption isotherms with experimental data, it is evident that none of the proposed models leads to a quantitative agreement. In our opinion, these discrepancies can be due to the deficiencies of the modelling of the zeolite flexibility and/or the argon-zeolite interactions. The fact that different flexible models yield different results points to the importance of having an accurate model for the zeolite that is able to faithfully reproduce the zeolite vibrations in the presence of high adsorbate loadings. On the other hand, we have seen that parameters of the crossed argon interactions fitted to reproduce the adsorption isotherm on MFI had to be slightly modified to obtain a good agreement also for MEL. This might indicate that the Lennard-Jones functional form used to describe the argon-zeolite interactions also needs to be improved.

As mentioned in the Introduction, information about the microscopic structure of adsorbed argon can be obtained by neutron diffraction experiments. Indeed, there are plenty of instances in the bibliography in which this technique has been used to investigate the structure of a variety of adsorbed molecules within zeolite frameworks (see, for example, Ref. [79]). Following a similar protocol as that used by Lewellyn *et al.* [1], we have performed measurements of a MEL sample at different loadings, before and after the sub-step. The experiment was carried out using two different argon isotopes, ^{40}Ar and ^{36}Ar, with scattering lengths differing by an order of magnitude, which allows us to separately visualize the structure of the zeolite and of the adsorbate. These data will be analyzed in a forthcoming article. Besides comparing the experimental data to theoretical spectra calculated from configurations of the simulations of this work, we will also try to obtain a structural model compatible with the experimental spectra by using the Reverse Monte Carlo method. In a previous work, we showed theoretically that this method can provide a satisfactory description of the adsorbed fluid up to the level of three body correlations [5, 6]. In that theoretical work, the zeolite was kept frozen, but its flexibility can easily be incorporated in the Reverse Monte Carlo method, being also possible to investigate possible deformations of the zeolite. The structural models obtained in this subsequent study could be also potentially used to get a better modelling of the argon-zeolite interactions using a numerical inversion procedure [115].

Improving the zeolite models, so that they are able to properly predict structural deformations upon adsorption of different molecules, is probably a more difficult goal. Most of the models proposed so far have been fitted to dynamical properties (such as the infrared vibrational spectrum) and structural properties in the presence of cations. However, there is no guarantee that these models will work for adsorbates under tight confinement conditions, as those considered in this work. We speculate that a more reasonable approach for our purposes will be to fit the zeolite model to try to predict the very well characterized structural changes on MFI. Given that these structural changes are really subtle, consisting simply on small modifications

of the group symmetry, we anticipate that this will be a challenging goal.

Acknowledgment

This work was funded by Dirección General de Investigación Científica y Técnica under Grants No. FIS2013-47350-C5-4-R, MAT2012-38567-C02-01 and Severo Ochoa SEV-2012-0267. The authors are thankful to Y. Mejía for performing the adsorption measurements. VSG also thanks the CSIC for support by means of a JAE program Ph.D. fellowship. Fruitful discussions with Noé G. Almarza are also gratefully acknowledged.

5.6 Supplementary material

Effect of the bond distance and bond angle parameters in the structure of the empty zeolite

In order to characterize the structure of the zeolite we evaluated different properties, such as the partial distribution functions defined as:

$$g_{\alpha\beta}(r) = \frac{n_{\alpha\beta}(r)}{\Delta V \rho_\alpha}, \tag{5.3}$$

where $n_{\alpha\beta}$ is the number of atoms of type β at a distance between r and $r + \Delta r$ of a central atom of type α, ΔV is the volume of a spherical shell between r and $r+\Delta r$, and ρ_α is the partial density of component α. We also calculated the angular distribution functions (ADF) of the O-Si-O and Si-O-Si angles of the zeolite using the following expression:

$$ADF_{OSiO}(cos\theta) = \frac{n_{OSiO}(cos\theta)}{n_{OSiO,tot}\Delta(cos\theta)} \tag{5.4}$$

$n_{OSiO}(cos\theta)$ being the number of O-Si-O triplets forming an angle whose cosine is within $cos\theta$ and $cos\theta + \Delta(cos\theta)$ and $n_{OSiO,tot}$ the number of O-Si-O triplets. The ADF for the Si-O-Si triplets is defined analogously.

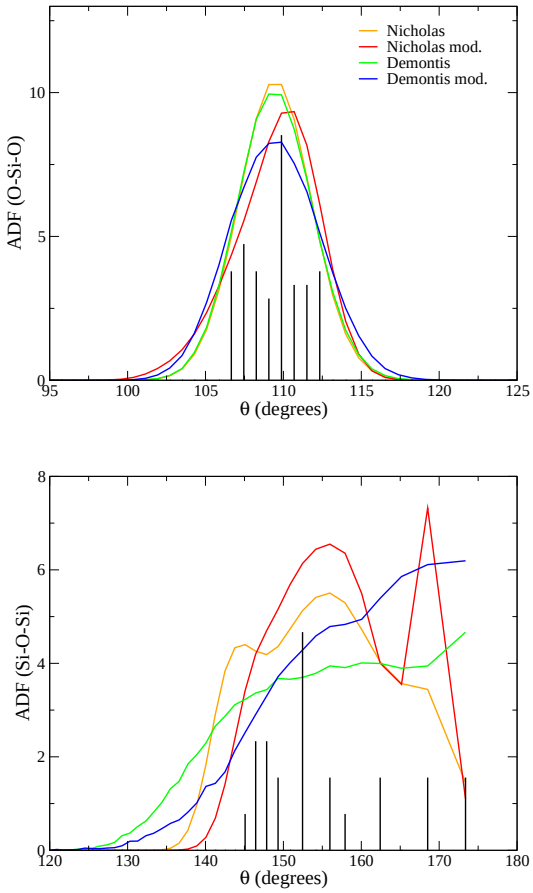

Figure 5.8: Probability distribution of the O-Si-O and Si-O-Si bending terms in the MEL as obtained from NVT simulations at T=77K for the different models considered in this work. For comparison the distributions corresponding to the experimental crystal structure (Ref.[11]) are also shown as black vertical lines. To facilitate the visualization the probabilities of the experimental data has been scaled.

Figure 5.9: Comparison of the experimental structure and average structure of the empty (left) and full loaded ($\sim$ 36 atoms/u.c., right) zeolite as obtained from the simulations with the modified Demontis model. The experimental structure is shown in red and the average structure obtained from the simulations with the flexible zeolite in blue.

Effect of the argon-oxygen parameters on the simulated adsorption isotherm

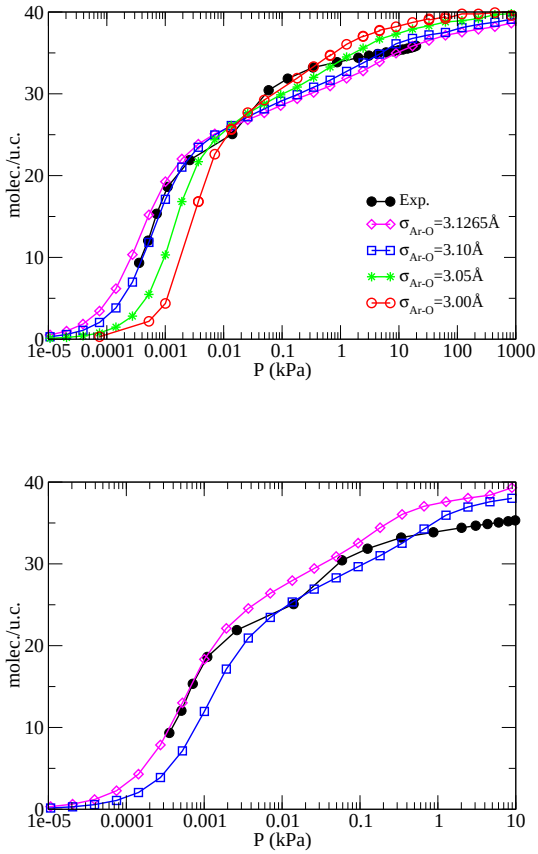

Figure 5.10: Left panel: Effect of the size parameter σ_{Ar-O} on the adsorption isotherm. These results were obtained keeping the zeolite frozen. Right panel: Comparison of the adsorption isotherm using the Ar-O parameters obtained in this work and using those fitted to the experimental adsorption data for the MFI zeolite (taken from Ref. [108]).

Effect of the zeolite flexibility on the structure of the adsorbate: partial distribution functions

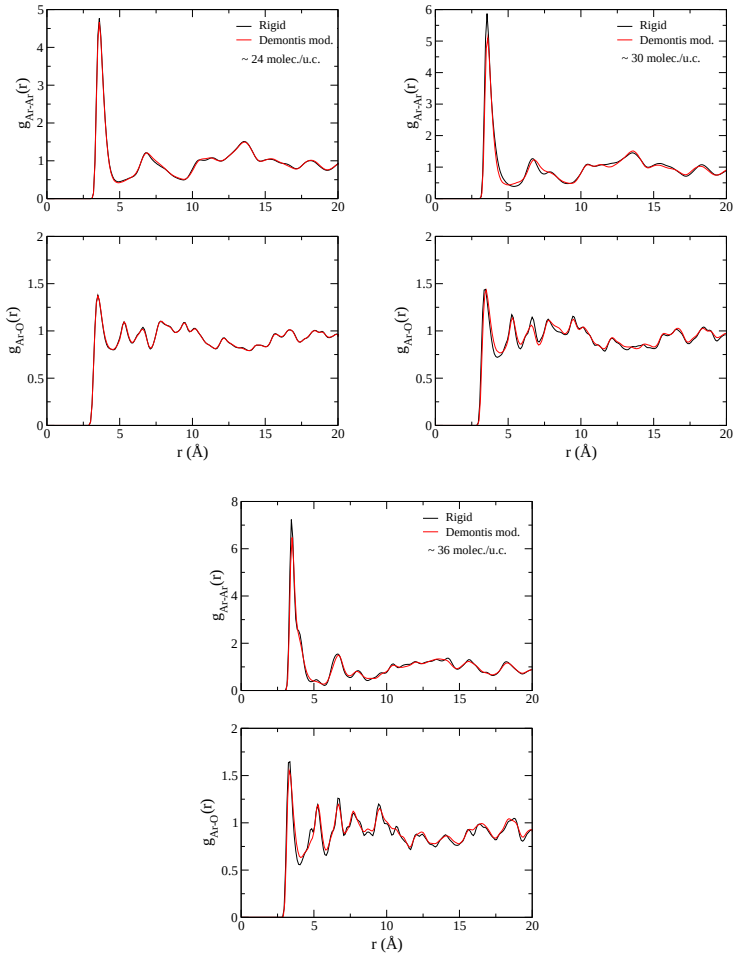

Figure 5.11: Ar-Ar and Ar-O partial distribution functions on MEL at different loadings at 77 K.

Chapter 6

Evidences of a Structural Change in Pure-Silica MEL upon the Adsorption of Argon

J. Phys. Chem. C, **submitted** (2015)

Vicente Sánchez-Gil[1], Eva G. Noya[1], José María Guil[1], Enrique Lomba[1], Susana Valencia[2], Iván da Silva[3], Laszlo Pusztai[4] and Laszlo Temleitner[4]

[1] *Instituto de Química Física Rocasolano, Consejo Superior de Investigaciones Científicas, CSIC, Calle Serrano 119, 28006 Madrid, Spain*

[2] *Instituto de Tecnología Química (UPV-CSIC), Avda. de los Naranjos s/n,E-46022 Valencia, Spain*

[3] *ISIS Facility, Rutherford Appleton Laboratory, Chilton, Oxfordshire OX11 0QX, UK*

[4] *Institute for Solid State Physics and Optics, Wigner Research Centre for Physics, P.O. Box 49, H-1525 Budapest, Hungary*

Abstract

In this work, we investigate the structure of argon adsorbed on pure-silica MEL at liquid nitrogen temperature. Our goal is to provide a microscopic interpretation for the appearance of a sub-step in the adsorption isotherm at intermediate loadings before saturation. For that purpose, we first perform time-of-flight neutron diffraction experiments of the loaded zeolite, before and after the sub-step. The measured spectra reveal that, after the sub-step, a considerable ordering of the adsorbate builds up, but there are also evidences of a zeolite structural change. These experimental data were then used in conjunction with Reverse Monte Carlo simulations to obtain theoretical structural models of the adsorbate/adsorbent system. Interestingly, the spatial distribution of the adsorbate predicted by Reverse Monte Carlo is considerably different from that obtained from grand canonical Monte Carlo simulations, even at half loading. We ascribe these discrepancies to deficiencies in the argon-zeolite interatomic potential. Besides, at high loading, we observe a different distribution of atoms along the channels parallel to the x-axis and those parallel

to the y-axis. This might be attributed to a zeolite structural change distorting the tetragonal symmetry of MEL.

6.1 Introduction

The adsorption of simple gases at liquid nitrogen temperature has often been used as a means of characterizing the porosity of zeolites. However, in some cases it is observed that, even for simple gases, the adsorption does not occur through a typical type I isotherm, but, instead, follows a more complex pattern exhibiting one or more sub-steps [1, 2]. For example, the uptake of Ar on silicalite-1 (framework type MFI) and silicalite-2 (framework type MEL) follows, in both cases, a type I+IV isotherm with a sub-step at intermediate loads [1, 24, 92, 3] (see Fig. 6.1). Both zeolites have a similar structure consisting on a three dimensional network of fairly narrow cylindrical channels with diameters in the range of approximately 5.0 to 5.6 Å [114]. The essential difference lies in the fact that MFI consists of an array of parallel linear cylindrical pores intersected by sinusoidal channels, whereas in MEL all the pores are linear.

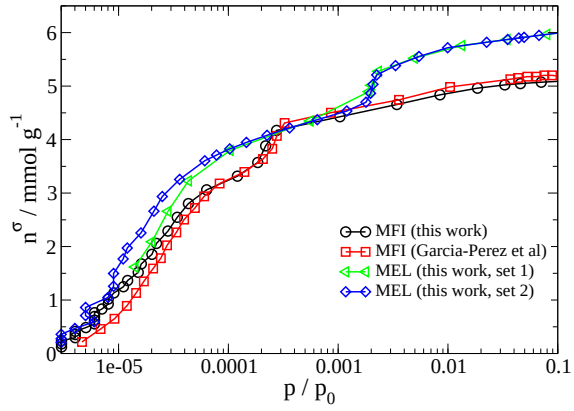

Figure 6.1: Experimental adsorption isotherms of Ar on silicalite-1 (MFI) and silicalite-2 (MEL) at liquid nitrogen temperature. Data were taken from Refs. [24, 3] . The arrows indicate the loadings for which neutron diffraction measurements were performed.

The origin of the sub-step in the adsorption isotherm of argon on MFI has been extensively investigated over the last years. In particular, Llewellyn *et al.* [1] found that this sub-step was correlated to a sudden increase in the heat of adsorption, and observed the emergence of a number of well-defined peaks in the diffraction pattern after the sub-step. They interpreted both signatures as an indication of an adsorbate phase transition from a fluid-like to a solid-like state. Molecular simulations using frozen zeolite frameworks have been shown to be unable of reproducing the appearance of a sub-step in the adsorption isotherm in the correct pressure range, even with the incorporation of three-body contributions [93, 97, 95]. In some cases, the sub-step is predicted, but at pressures several orders of magnitude higher than in experiments. In addition to that, diffraction patterns calculated from simulated configurations after the sub-step exhibit some but not all the peaks observed in

the measurements [95]. One possibility would be that those peaks are the result of a zeolite structural change [1, 97, 95]. This hypothesis is reinforced by the fact that MFI-type zeolites can undergo structural changes from a monoclinic structure (which is the stable phase at temperatures lower than 380 K [15]) to an orthorhombic lattice with group symmetry *Pnma* when increasing the temperature [14], or to another orthorhombic structure with group symmetry $P2_12_12_1$ upon the adsorption of big aromatic molecules [80]. On the other hand, simulations incorporating the flexibility of the zeolite provide adsorption isotherms closer to the experimental data [24]. Thus, one might speculate that the sub-step appears as a result of a combined effect of the reorganization of the adsorbate and a structural change of the zeolite [24]. At this stage, a detailed description of the microscopic origin of the sub-step is still far from satisfactory.

In the case of MEL, some of us have recently investigated argon adsorption by means of volumetric experiments and Monte Carlo simulations [3]. We found that, again the adsorption isotherm exhibits a sub-step at intermediate loadings. This indicates that the emergence of the sub-step is to some extent independent of specific structural details of the pores, such as the presence of zig-zag channels. As for MFI, we cannot rule out the possibility that the sub-step coincides with a structural change of the zeolite. Even if, as far as we know, a detailed description of structural changes on MEL has not been reported, there are some experimental evidences of such structural transformations upon increasing the temperature [11, 98, 99]. In Ref. [3], it was found that simulations using either a rigid or a flexible zeolite framework were not able to accurately reproduce the experimental adsorption isotherm. We observed that the flexibility of the zeolite played an important role, changing the shape of the adsorption isotherm, similarly to what has been previously found for MFI [24]. However, the results were highly dependent on the chosen zeolite model, stressing the need to develop accurate zeolite model potentials. In addition to that, argon-zeolite interactions fitted to low pressure experimental data were somewhat different from those obtained for MFI [3, 24]. Given that MEL and MFI zeolites have identical chemical composition and very similar topology, it seems clear that also a better description of the crossed argon-zeolite interactions is needed.

With the aim of getting further insight into the microscopic origin of this peculiar behaviour, in this work, we have performed time-of-flight (TOF) neutron diffraction experiments of MEL with adsorbed argon at different loads, before and after the sub-step in the adsorption isotherm, at liquid nitrogen temperature. Diffraction experiments have often been used to investigate the structure of adsorbed fluids of varying complexity on zeolites (see, for example, Refs. [80, 1, 2, 94, 116, 117, 79]). When only a few big molecules per unit cell are adsorbed, the structure of the adsorbate/adsorbent system can be determined by the Rietveld refinement method [118, 117, 78, 79]. However, for the case of small gas molecules, such as argon, structural models have been most often constructed using MC simulations. Nonetheless, as mentioned before, the quality of the structural model obtained strongly depends on the goodness of the interatomic potentials used to describe the system, and usually not all the experimental peaks are reproduced [95].

Here, we will use a different approach to obtain a structural model of adsorbed argon on MEL from the experimental diffraction pattern, which is by resorting to Reverse Monte Carlo (RMC) simulations [39]. This method consists in a numerical search for a molecular structural model whose diffraction pattern is compatible with

the experimental one [39]. Initially, this method was used to investigate the structure of disordered systems, including simple liquids, molecular liquids or amorphous solids, just to mention a few examples [73]. However, it has later been extended also to the study of crystalline solids with some degree of disorder [119]. In this case, given that the diffraction pattern presents both strong Bragg peaks coming from the crystalline structure and a diffuse contribution arising from the disorder, "total scattering" measurements are needed. These are measurements that cover a wide range of momentum transfer q, so that the diffractogram contains information about the long-range crystalline order and the short-range diffuse contribution as well [62, 120]. This can be achieved by using powder TOF neutron diffractometers [62].

The use of total scattering data introduces some complexity in the way that RMC deals with the fit of the calculated diffraction pattern to the experimental one. So far, two alternative routes have been proposed for this purpose. The first one, implemented in the RMCpow code [35], calculates the orientationally averaged scattering functions so that it is possible to compare the calculated diffraction pattern to the experimental one. The second method, available in the RMCprofile package [120], uses real space radial distribution functions to calculate the diffuse contribution, and an explicit analysis of Bragg peaks. In this work, we opted for using the method used by RMCpow, but employed our own implementation. This allowed us to easily adapt it to the particularities of our system. More specificially, our code uses the N-RMC method, which is a variant of the RMC approach that allows for fluctuations of the number of particles and is specially suited to deal with highly confined systems [5, 6].

The paper is organized as follows. In Section 6.2, the experimental preparation of the samples and the TOF neutron experiments are described. In Section 6.3, we briefly sketch the the RMC method and provide the simulation details. The experimental results, as well as the structural models obtained with RMC are discussed in Section 6.4. Finally, a summary of the main conclusions of the paper is given in Section 6.5.

6.2 Experimental procedure

A powder sample of pure-silica ZSM-11 was expressly synthesized as described in Ref. [101]. The micropore volume of the sample was 0.12 cm^3/g [101]. The empty MEL sample was heated in oxygen flow, c.a. 30 cm^3/min up to 723 K and kept at this temperature for 4 hours to eliminate any organic residue. After that, the zeolite was introduced into a vanadium cell and out-gassed overnight at 723 K (P<1 mPa). Two sets of measurements were performed using as adsorbate high purity ^{36}Ar and ^{40}Ar, respectively. ^{40}Ar was supplied by ISIS and ^{36}Ar was purchased from Euriso-top.

TOF neutron diffraction experiments were carried out at the GEM diffractometer at ISIS facility based on the Rutherford Appleton Laboratory. The temperature of the sample was kept at 77 K with a helium cryostat, which can be penetrated by the neutron beam. The diffraction pattern was measured up to very high values of q (we obtained data up to $q_{max} \approx 40$ $Å^{-1}$) [38]. The zeolite was loaded with argon *in situ*. Besides measuring the diffraction pattern for the empty zeolite, data were collected at two different loads: at medium (before the sub-step) and high loads

(just after the sub-step, see the arrow marked pressures at Fig. 6.1). The amount of load was inferred from the volume of gas added and the mass of the zeolite sample (2.4467 g). After the measurement for each argon isotope, the vanadium cell was heated and pumped to obtain a vacuum lower than 1 mbar.

As mentioned before, these experiments were carried out using two different argon isotopes, namely, ^{40}Ar and ^{36}Ar. These isotopes exhibit the same adsorption behaviour, but have quite different coherent scattering lengths, being 1.90 fm for ^{40}Ar, and 24.90 fm for ^{36}Ar [71]. As a consequence, when the zeolite is loaded with ^{40}Ar, the signal of the adsorbate is much smaller than that coming from the zeolite (also because, at saturation, the number of atoms belonging to the zeolite is about one order of magnitude higher than that of the adsorbed fluid). This will highlight any possible structural change in the zeolite framework, but makes it practically impossible to gain information on the distribution of the adsorbed fluid. On the other hand, when the zeolite is loaded with ^{36}Ar, the signal of the adsorbed fluid has a considerable weight on the total diffraction pattern, thus providing access to information on the adsorbate structure. The drawback in this case is that new features appearing on the diffraction pattern might be ascribed both to the presence of adsorbate and to structural changes in the zeolite. By jointly analyzing both sets of data, we intend to obtain information about the structure of the adsorbate/adsorbent system.

6.3 Reverse Monte Carlo modelling

As we are considering a tightly confined system, the usual implementation of the Reverse Monte Carlo (RMC) method [39] might face sampling difficulties due to the poor diffusion of particles along the narrow channels of the zeolite. Therefore, we will resort to a recent extension of the RMC method, the N-RMC, that deals efficiently with highly confined fluids [5]. Briefly, the N-RMC method consists in performing, additionally to the usual random particle moves of standard RMC, trials of insertion/removal of adsorbate particles. A detailed description of the method and how to adapt it to use it in conjunction with experimental TOF data is provided in the Supporting Information.

N-RMC simulations were performed using a custom-made code. Given that the most time-consuming part of the simulations is the evaluation of the structure factor and this is suitable for a q-space parallelization, we implemented the code in CUDA so that it could be run on a GPU. On a Nvidia GeForce GTX 590 GPU with 960 cores, the parallel GPU code runs 105 times faster than the serial version on an Intel Core Quad CPU at 2.66 GHz for the typical system size used in this work ($N \approx 5000$, N being the number of particles in the system).

The simulation box was constructed by replicating the experimental pure-silica MEL unit cell [11] to obtain a 2×2×3 supercell. The equilibrium number of adsorbed argon atoms, N_{exp}, was set to the estimated experimental value at each loading, namely, N =20 atoms/u.c at half loading and N =31 atoms/u.c. at high loading. Given that ^{36}Ar provides a strong signal for the adsorbate, the experimental diffraction pattern measured with this isotope was used as target in our N-RMC. To keep a reasonable computational time, the data was fitted only up to 5.6 Å^{-1}, which means that only data collected from detector banks 1 to 5 were fitted (the range of scattering angle, 2θ, covered by each detector bank of GEM is given in

Ref. [38]). The structure of the adsorbed fluid was characterized by evaluating the Ar-Ar and Ar-O average pair distribution functions, as well as one-, two- and three-dimensional density distributions maps [121]. More details of the simulations can be found in the Supporting Information.

The *N*-RMC results are also compared to grand canonical Monte Carlo (GCMC) simulations. In GCMC, the system was modelled as in Ref. [3]. In particular, the Ar-Ar and Ar-O interactions were described using a Lennard-Jones (LJ) model. As is customary for adsorbates without net charge, Ar-Si interactions were not explicitly considered. Given that the spatial distribution of the adsorbate is very similar regardless of whether the zeolite atoms are allowed to vibrate or not (using the Demontis model [25] for the zeolite) [3], we will present only results for simulations performed with the frozen zeolite. Using equilibrated configurations of GCMC, we calculated diffraction patterns, as well as the average pair distribution functions and density maps mentioned above.

6.4 Results

6.4.1 Experimental diffraction patterns

The experimental diffraction patterns for MEL, empty and with adsorbed ^{40}Ar and ^{36}Ar at two different loads (before and after the sub-step in the adsorption isotherm at 77 K) are shown in Fig. 7.4. The GEM diffractometer collects measurements using an array of detectors that are arranged in banks. As each bank provides a different resolution, it is not straightforward to merge all the banks in a single diffraction pattern, specially for crystalline materials [122, 123]. For this reason, here we will work directly with the data split into banks as measured in the experiments. For visualization purposes, we plot in Fig. 7.4 the results only for those four banks that exhibit the more interesting features.

Focusing first on the results for ^{40}Ar (in which case the signal of the adsorbate is much lower than that of the adsorbent), it can be seen that the diffraction pattern of the zeolite at half load is almost identical to the one of the empty zeolite. The only appreciable differences are a subtle decrease of the two strong peaks at low q (at $q \approx 0.55$ Å^{-1} and $q \approx 0.63$ Å^{-1}) and those at $q \approx 0.94$, 1.05 and 1.13 Å^{-1}. This is due to a destructive interference steaming from the Ar-zeolite crossed contribution [1, 5]. At higher load (after the step in the adsorption isotherm), the spectrum is again very similar to those of the empty and half load cases. However, a more careful inspection reveals the appearance or enhancement of some peaks at $q \approx 1.33, 1.72, 1.89, 2.86$ and at $q > 3$ Å^{-1} (see the insets in Fig. 7.4). Given that the ^{40}Ar signal is much lower than the zeolite contribution, we speculate that these new peaks arise from a small structural change of the zeolite framework.

If we look now at the results for ^{36}Ar, the diffraction pattern of the adsorbate/adsorbent system differs considerably from that of the empty zeolite, even at half load. The low-q peaks are now almost suppressed due to the zeolite-argon destructive contribution mentioned before. On the contrary, for $q > 1.5$ Å^{-1}, new peaks appear upon the adsorption of argon. These peaks become shaper and more intense at high load. Comparing this diffraction pattern with that of ^{40}Ar, it becomes evident that these new peaks are due to the adsorbate. The fact that most of the peaks appearing at high loads are quite sharp evidences a strong ordering of

the adsorbate atoms, exhibiting a solid-like behaviour.

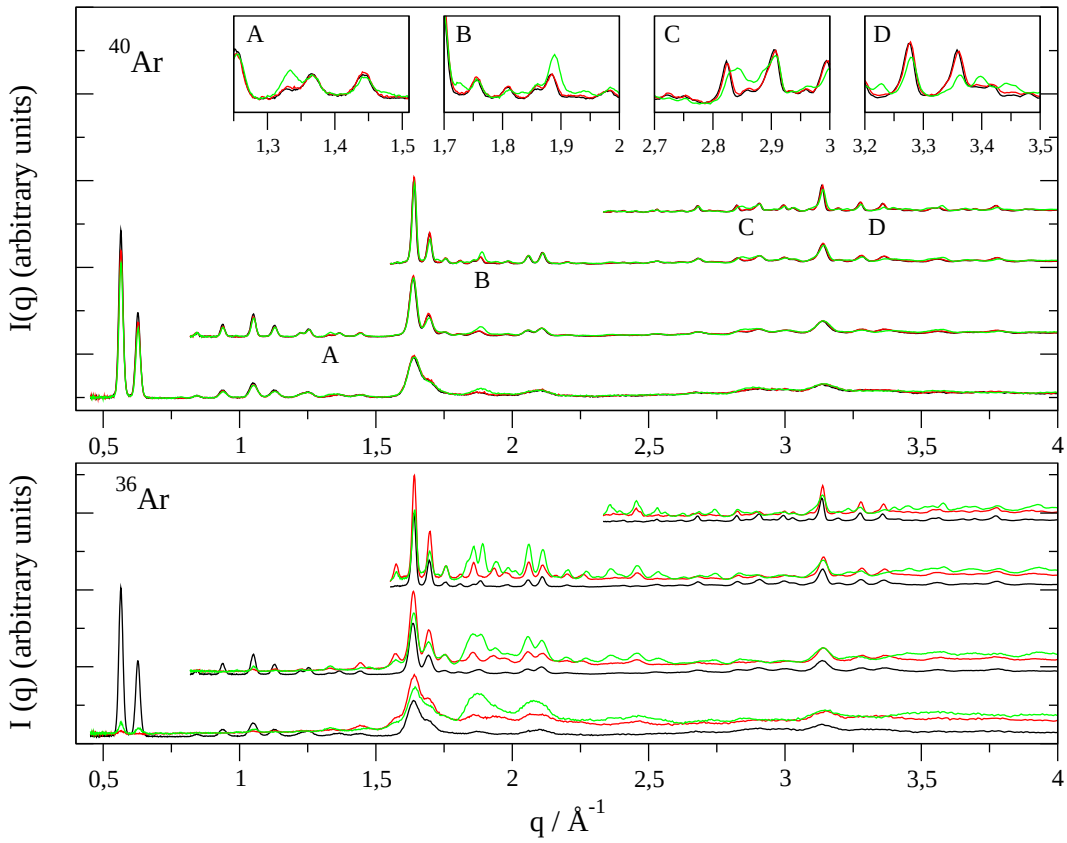

Figure 6.2: Experimental diffraction patterns for empty MEL (black line) and for MEL with adsorbed argon at two different loads, before ($\sim$ 20 molec./u.c., red line) and after ($\sim$ 31 molec./u.c., green line) the sub-step in the adsorption isotherm at 77 K. The upper panel shows the results for the most common isotope ^{40}Ar, whereas the lower panel displays the spectra for isotope ^{36}Ar, which has a considerably larger scattering length. For ^{40}Ar, the insets show enlarged views of some regions of the diffractogram to highlight the appearance of new peaks after the sub-step in the adsorption isotherm. Results from different detector banks have been displaced along the y-axis to aid visualization.

6.4.2 Structural model: Reverse Monte Carlo results

Let us start by comparing the calculated spectra for the empty zeolite (taking the structure from the bibliography [11]) to the measured data. As can be seen in Fig. 6.3, there is a fairly good agreement between the two sets of data. We also performed a RMC simulation for the empty zeolite using as target the experimental TOF neutron diffraction pattern. This simulation has two purposes. On one hand, it provides a better fit of the experimental data than the structural model of Terasaki *et al.* [11] (see Fig. 6.3). On the other hand, it allows us to choose reasonable values for the parameters that control the weight of the bonding and bending constraints of the zeolite (Eqs. 8 and 9 in the Supporting Information). In particular, the values of these parameters are fitted to roughly reproduce the pair and angular

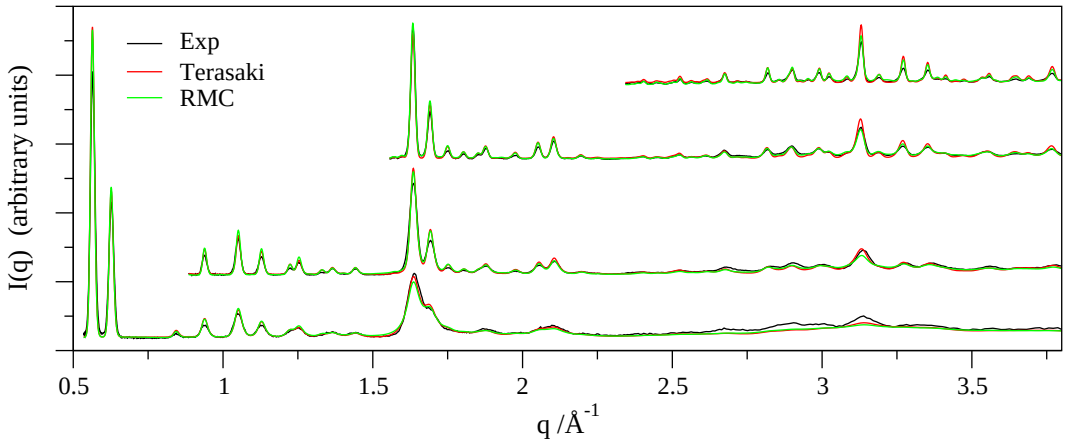

Figure 6.3: Experimental neutron TOF diffraction pattern of the empty zeolite compared to the calculated spectrum using the zeolite atomic coordinates provided by Terasaki *et al.* [11], and to that obtained from a RMC simulation. For clarity, only detector banks 2 to 5 (from bottom to top) are shown. Results from different banks have been displaced along the y-axis to aid visualization.

distribution functions obtained in a GCMC simulation using the Demontis model [25]. Even though we constrained only the Si-O bond distances and the Si-O-Si bending angles, a fairly good agreement is also obtained for the Si-Si and O-O pair distribution functions, as well as for the Si-O-Si bending angle (data not shown).

We focus now on the measurements of the loaded zeolite. As our purpose is to obtain a structural model for the adsorbate, we used the ^{36}Ar pattern as the target for our N-RMC simulations. For simplicity, we started with a frozen zeolite model. The results for MEL at half load ($\approx$ 20 atoms/u.c.) are shown in Fig. 6.4. As can be seen in Fig. 6.1, this corresponds to a point before the sub-step in the adsorption isotherm at 77 K. In this case, N-RMC is able to fit with good accuracy the experimental structure factor for all ranges of q. The good agreement obtained using N-RMC simulations that keep the zeolite rigid, reinforces the previous conclusion that there is not an appreciable framework structural change at moderate loadings. For comparison, in Fig. 6.4, we also include the calculated diffraction pattern using configurations from GCMC simulations. Although some differences in the intensity of a few peaks in the range of 1.8 Å^{-1} $< q <$ 2.5 Å^{-1} are clearly seen, in general, there is a quite good agreement between the pattern calculated from GCMC simulations and the experiments. However, as expected, N-RMC provides a better fit to the experimental data.

At high load, it is not so clear that we can still keep the zeolite rigid, as we found evidences in the ^{40}Ar measurements of a possible zeolite structural change. Still, as this change seems to be small and to keep the calculations as simple as possible, we first have performed N-RMC simulations with a frozen zeolite framework. The resulting diffraction pattern is compared to the experimental results in Fig. 6.5. In general, N-RMC provides a fairly good fit of the experimental diffraction pattern, except for some small differences in the regions $1.8 < q < 2$ Å^{-1} and for q above 2.75 Å^{-1}. Note that those values of q coincide with the regions for which the spectrum of ^{40}Ar at high load differs most from the empty and the half loaded cases. We interpret that these small differences might be due to some deformation of the zeolite that

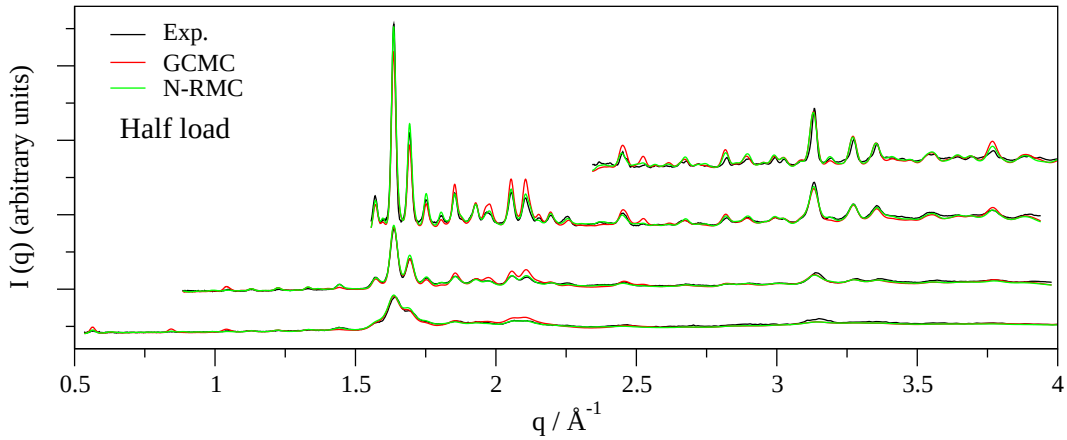

Figure 6.4: Comparison of the experimental and the N-RMC diffraction pattern of ^{36}Ar on MEL at half load. N-RMC results were obtained keeping the zeolite frozen and using a hard core to avoid overlaps between particles. For comparison, the calculated diffraction pattern using configurations from GCMC simulations using a rigid zeolite [3] is also shown. For clarity, results from different banks are displaced along the y-axis. Only detector banks 2 to 5 (from bottom to top) are shown.

has not been included in our simulations. Interestingly, even if a zeolite structural change takes place, our results indicate that the main features of the experimental diffraction pattern can still be captured by the frozen zeolite approximation.

In Fig. 6.5, we also include the calculated spectra from configurations obtained along a GCMC simulation. In this case, the GCMC diffraction pattern reproduces some but not all the experimental peaks. In particular, there are notable differences for q larger than 1.75 Å^{-1}. For example, the experimental triple peak at $1.81 < q < 1.91$ Å^{-1} is a single peak in GCMC, and the intensity of the two peaks between $2.02 < q < 2.25$ Å^{-1} is overestimated. For q's larger than 2.3 Å^{-1}, differences become more evident, GCMC failing to predict the appearance and/or the intensity of numerous peaks.

With the aim of getting some insight into the origin of the differences between the N-RMC and GCMC spectra, we calculated the three partial contributions to the diffraction pattern, i.e., those coming from the zeolite, the adsorbate and the crossed zeolite-adsorbate atomic positions. We restrict our discussion to the region where the most significant differences between N-RMC and GCMC have been found. As can be seen in Fig. 6.6, N-RMC predicts that the triple peak between $1.81 < q < 1.91$ Å^{-1} arises mainly from the Ar-Ar contribution. The second of these peaks has an additional positive contribution from Ar-zeolite, whereas the intensity of the third peak is lowered due to a destructive Ar-zeolite interference. GCMC fails to predict the first and third peaks. What is worst, for the third peak, it underestimates the Ar-Ar contribution but overestimates the destructive argon-zeolite contribution, leading to a cancellation of errors. The higher intensity of the peaks at $2.02 < q < 2.25$ Å^{-1} is due to an overestimation of both, the Ar-Ar and Ar-zeolite contributions. Thus, we can conclude that GCMC describes poorly this region of the diffraction pattern, as compared to the N-RMC results.

So far we have seen that configurations from GCMC simulations present diffraction patterns that are fairly similar to those obtained from N-RMC (and, thus, also

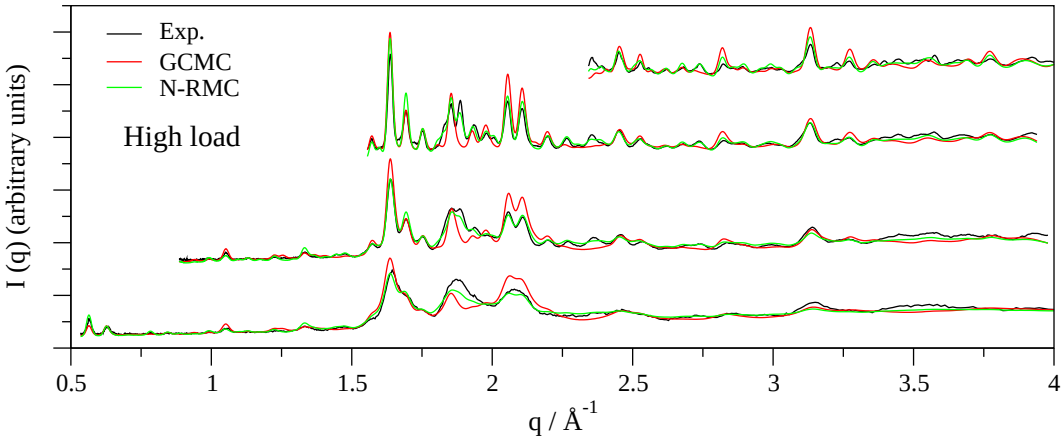

Figure 6.5: Comparison of the experimental and the N-RMC diffraction pattern of ^{36}Ar on MEL at high load. N-RMC results were obtained keeping the zeolite frozen and using a hard core to avoid overlaps between particles. For comparison, the calculated diffraction pattern using configurations for GCMC simulations using a rigid zeolite [3] is also shown. For clarity, results from different detector banks are displaced along the y-axis. Only detector banks 2 to 5 (from bottom to top) are shown.

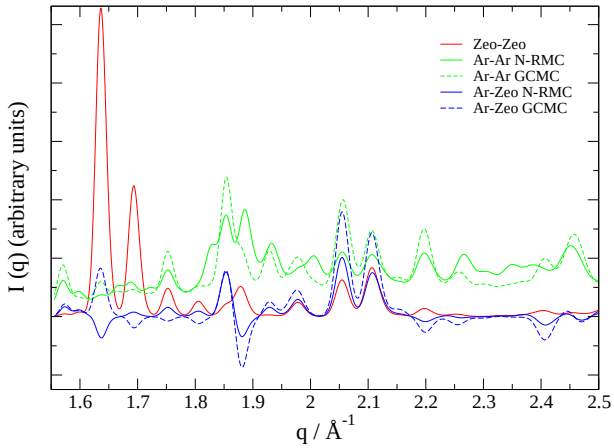

Figure 6.6: Comparison of the partial contributions to the total diffraction pattern for the N-RMC and GCMC structural models at high load.

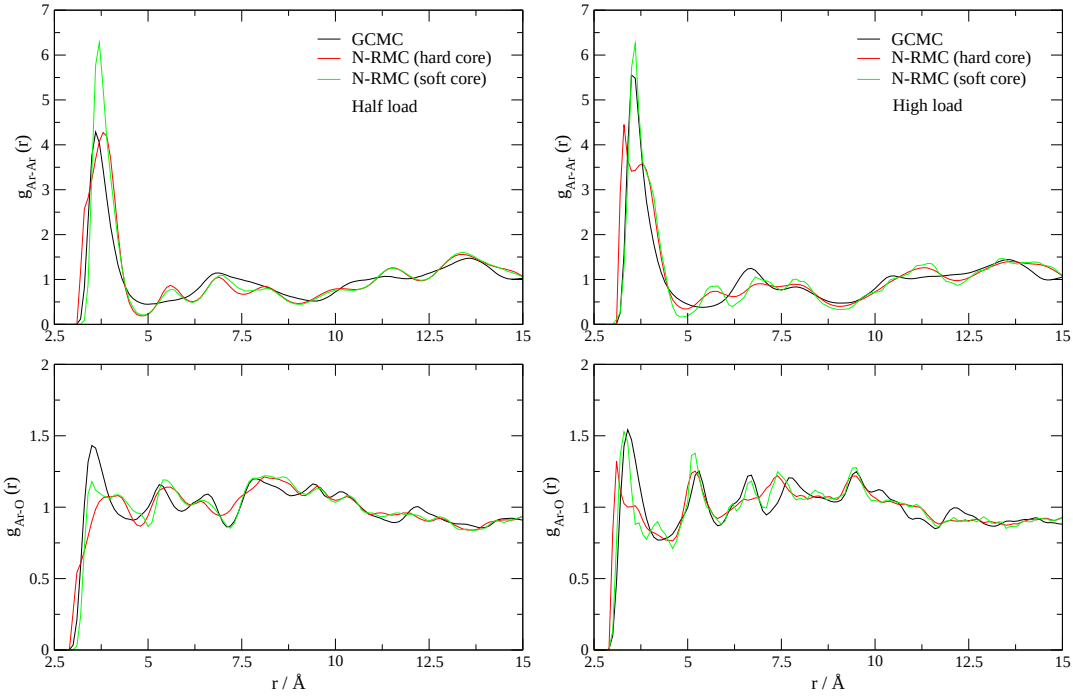

Figure 6.7: Ar-Ar and Ar-O pair distribution functions obtained with *N*-RMC at half (left column) and high loads (right column). Two sets of data are included, the difference between them being that in one of them overlaps between the particles are avoided using a hard core and in the other a soft core is used instead. For comparison, the distribution functions obtained from GCMC simulations are also shown [3].

to the experimental data) at half load, but exhibit appreciable discrepancies at high load. Now we investigate how the differences between *N*-RMC and GCMC diffraction patterns translate to the distribution of argon atoms in real space by calculating the average Ar-Ar and Ar-O pair distribution functions (see Fig. 6.7).

Curiously, at half load, differences between the GCMC and *N*-RMC partial distribution functions are much more significant than those observed in the spectra (see Fig. 6.4). In particular, *N*-RMC predicts a more structured Ar-Ar distribution function. The first maximum is displaced towards slightly larger distances, and the minimum after this first peak is deeper. At medium distances, the *N*-RMC distribution function displays well-defined maxima at roughly 5.5, 7 and 8 Å. The two latter peaks seem to be also present in the GCMC distribution function, although considerably smoother. Indeed, it is fairly straightforward to see that the peak at 7 Å corresponds to second neighbours in the channels. However, the maximum at 5.5 Å is completely missing in the GCMC function. The more pronounced structure at medium distances is also reflected at larger distances (between 10-15 Å), the *N*-RMC function exhibiting more defined wiggles than GCMC. Looking now at the Ar-O distribution functions, again some differences become evident. In *N*-RMC, the first peak is much broader and less pronounced than in GCMC. The two following oscillations of the Ar-O distribution functions are present in both cases, although their shape is different in the two sets of data. At distances beyond 8 Å, discrepancies between the two curves are smaller, although still clearly visible.

At high load, there are again significant differences between the GCMC and the N-RMC curves (see Fig. 6.7). The first peak in the N-RMC Ar-Ar partial distribution function is split in two, one with the maximum at contact (i.e., at the distance of the diameter of the hard core introduced in N-RMC to avoid overlaps) and the second one at distances somewhat larger than that of the first maximum in GCMC. Then, there are three maxima at roughly the same distances as in the half load case, namely, at 5.5, 7 and 8 Å. Again the peak at 5.5 Å does not appear in the GCMC curve, causing a shift of the second maximum to shorter distances (to about 6.75 Å). The different local arrangement of the particles at short and medium distances reflects once more in the long range structure. Moving now to the Ar-O distribution, the first peak presents again a strange splitting, attaining the maximum value at contact. Apart from that, both curves are relatively similar, exhibiting oscillations roughly at the same distances.

In our opinion, the unusual shape of the first peaks in the partial distribution functions reveals deficiencies in the fit of the diffraction pattern at long distances and it is most likely a spurious feature due to the use of a hard core in the N-RMC simulations. For computational convenience, in N-RMC, the experimental pattern was fitted only to a rather limited range of q (up to about 5.6 Å^{-1}). However, we checked that increasing the range of q (up to 8 Å^{-1}) or the system size (to $4 \times 4 \times 6$ replicas of the unit cell, thus achieving a better sampling in q) did not lead to any improvement. But a careful look at the fit at q's larger than 3 Å^{-1} (see the pattern for the top bank in Fig. 6.5) reveals significant differences between the fitted and the experimental pattern. We attribute these differences to the fact that many of these peaks might emerge from a structural change of the zeolite, which is not taken into account in our N-RMC simulations. To check the validity of this hypothesis, we repeated the N-RMC simulations but introducing also particle moves of the zeolite atoms (the weights for each term in the acceptance probability are given in Table 1 in the Supporting Information). Unfortunately, we did not obtain a significant improvement either in the fit of the the diffraction pattern at long values of q (see Table 6.1), or a more physically reasonable first peak in the partial distribution functions of the adsorbate (data not shown).

The failure of this approach might be related to having used as target the ^{36}Ar diffraction pattern. As the signal of ^{36}Ar is quite strong, reflections arising from the zeolite at long distances are blurred by the diffuse contribution coming from the adsorbate. Thus, we also performed N-RMC simulations that simultaneously fit the ^{36}Ar and ^{40}Ar patterns. As can be seen in Fig. 6.8 and Table 6.1, the high-q region can now be reproduced with higher accuracy. However, the agreement is still not perfect (as compared, for example, with that obtained for the empty zeolite). Unfortunately, the first peaks of the average partial distribution functions are still rather unphysical. We speculate that a better fit might be obtained by introducing smart zeolite atomic moves that sample more efficiently a change of symmetry.

However, in the spirit of keeping the calculations as simple as possible, we opted for an alternative method to try to obtain distribution functions for which the shape of the first peak exhibits a shape closer to what one would expect from a physical point of view. With that objective in mind, we replaced the hard core to avoid overlaps between particles by a softer LJ repulsive core. Specifically, we used a Week-Chandler-Andersen potential [124], which is simply the usual LJ potential cut and shifted at distance of the minimum of energy, $r_{cut} = 2^{1/6}\sigma_{LJ}$. We denote

Table 6.1: Weighted-profile R-factors of the N-RMC fitted diffraction patterns. Values for each detector bank are given.

	R_{wp} (%)				
	Bank 1	Bank 2	Bank 3	Bank 4	Bank 5
Half (hard core)	25.11	10.64	8.26	8.34	12.64
Half (soft core)	24.81	11.27	9.56	7.99	13.08
Half (flex. zeolite)	23.58	10.60	8.54	8.23	12.77
High (hard core)	29.25	15.11	12.05	12.14	12.31
High (soft core)	30.04	15.38	10.06	10.81	10.82
High (flex. zeolite)	29.68	14.61	11.11	11.88	12.33
High (^{36}Ar)	7.64	7.06	10.94	7.32	5.74
High (^{40}Ar)	7.79	8.98	19.45	13.27	14.34

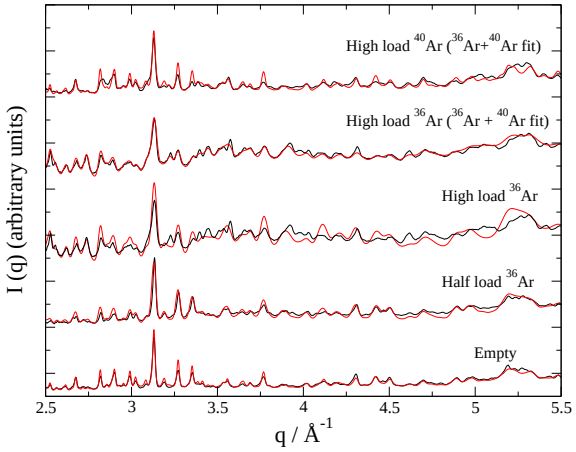

Figure 6.8: Comparison of the experimental (black line) and RMC (red line) diffraction pattern (bank 5) for the empty zeolite, at half and high load for ^{36}Ar. At high load, we also show the spectra for the two isotopes obtained in the N-RMC simulation that simultaneously fits the two sets of data.

this soft core potential as U_{LJ}^{rep}. The LJ parameters were the same as those used in the GCMC simulations [3]. The introduction of interatomic potentials in RMC is not new, it has already been implemented in the past [61]. As can be seen in Table 6.1, the fit of the spectrum hardly changes by incorporating the LJ repulsive core. However, the shape of the first maximum of the adsorbate partial distribution functions is now closer to that obtained from GCMC and to what one would expect, specially for the Ar-Ar case (see Fig. 6.7). For Ar-O, the first peak still differs somewhat from that of GCMC. At half load, the first maximum is less defined and much broader for N-RMC than for GCMC. This can be attributed to the tendency of RMC to generate configurations with the maximum disorder. At high load, on the contrary, the first peak is slightly shifted to shorted distances and is narrower than that of GCMC. This might be suggesting a stronger preference of the adsorbate atoms to position closer to the walls of the zeolite pores. Interestingly, the shape and location of the remaining maxima is not much affected by the use of a hard or a soft repulsive core. This indicates that the structural model predicted by N-RMC is rather robust beyond the first coordination shell.

We have seen that there are important differences between the average pair distribution functions obtained from N-RMC and GCMC simulations. However, it is not possible to infer how the adsorbate atoms are distributed along the zeolite's pores from the partial distribution functions alone, since these are spatially averaged

quantities. Hence, we have also calculated the probability density maps for a slab of thickness 1.5 Å parallel to the $x-y$ plane and that passes through the center of the channels and intersections (see Fig. 6.9). At half load, enhanced probabilities are clearly seen at three sites within the channel and four sites at the edges of the intersection. Each of these sites is split in two, being the probability appreciably higher in positions close to the pore walls and almost vanishing in the center of the pores. The tendency of argon atoms to place themselves close to the zeolite walls is also evident at the edges of the intersections. The GCMC map at half load is relatively similar to that of N-RMC, with the important difference that the higher probability occurs now at the center of the channels instead of at the edges.

At high load, differences between the N-RMC and GCMC probability density maps become more pronounced. According to N-RMC simulations, adsorbate atoms tend to occupy rather fixed positions close to the walls. This preference extends also to the intersections, where atoms are found more frequently at the corners. On the contrary, in GCMC, the maximum probabilities are found at the center of the channels, and at the center of the edges of the intersections.

Further insight into the distribution of argon atoms can be obtained by calculating integrated density profiles along the x and y axes. As shown in Fig. 6.10, at half load, the density profiles along the x and y axes are equivalent within statistical uncertainty, both in N-RMC and GCMC. This is consistent with MEL having tetragonal symmetry [11]. Focusing on the differences between N-RMC and GCMC, N-RMC exhibits somewhat broader and less pronounced peaks. This is in accordance with the tendency of RMC to yield the more disordered structure compatible with the experimental diffraction pattern. Apart from that, N-RMC and GCMC profiles are relatively similar, with two rather well defined peaks at the channels and another stronger peak at the junctions that exhibits two shoulders, one at each side. Note that due to the integration along the other two dimensions of space, this strong peak results from the addition of the contribution from the junctions and from the channels running in the perpendicular direction.

Surprisingly, at high load, the N-RMC profiles along the x and y axes are substantially different. This does not occur for GCMC, for which both profiles are equivalent, as expected from the tetragonal symmetry of zeolite. For GCMC, the profiles are rather similar to those obtained at half load, with the difference that now the peaks are considerably shaper due to the reduced mobility of the adsorbate atoms under the tighter confinement conditions. Besides, two smaller peaks appear at both edges of each intersection. The N-RMC density profile along the x axis also exhibits two peaks in the channels although much less defined than in the GCMC profile, again indicating a larger degree of disorder in N-RMC. At the intersections, on the contrary, it shows two quite well defined peaks with a reduced probability at the center of the intersections, in opposition to GCMC for which the maximum probability occurs precisely at those locations. Interestingly, in the density profile along y, there are three peaks at the intersections of similar intensity, i.e., the density probabilities are similar at the edges and at the center. Coincidentally, an integral equation approach predicts integrated profiles as the one found here for the y-axis, with three peaks at the intersections, although with different relative intensity [121]. This indicates that atoms are located at energetically favoured positions.

To make sure that this asymmetry was not due to an erroneous bias in our simulations, we checked that the same diffraction pattern but exchanged x and y

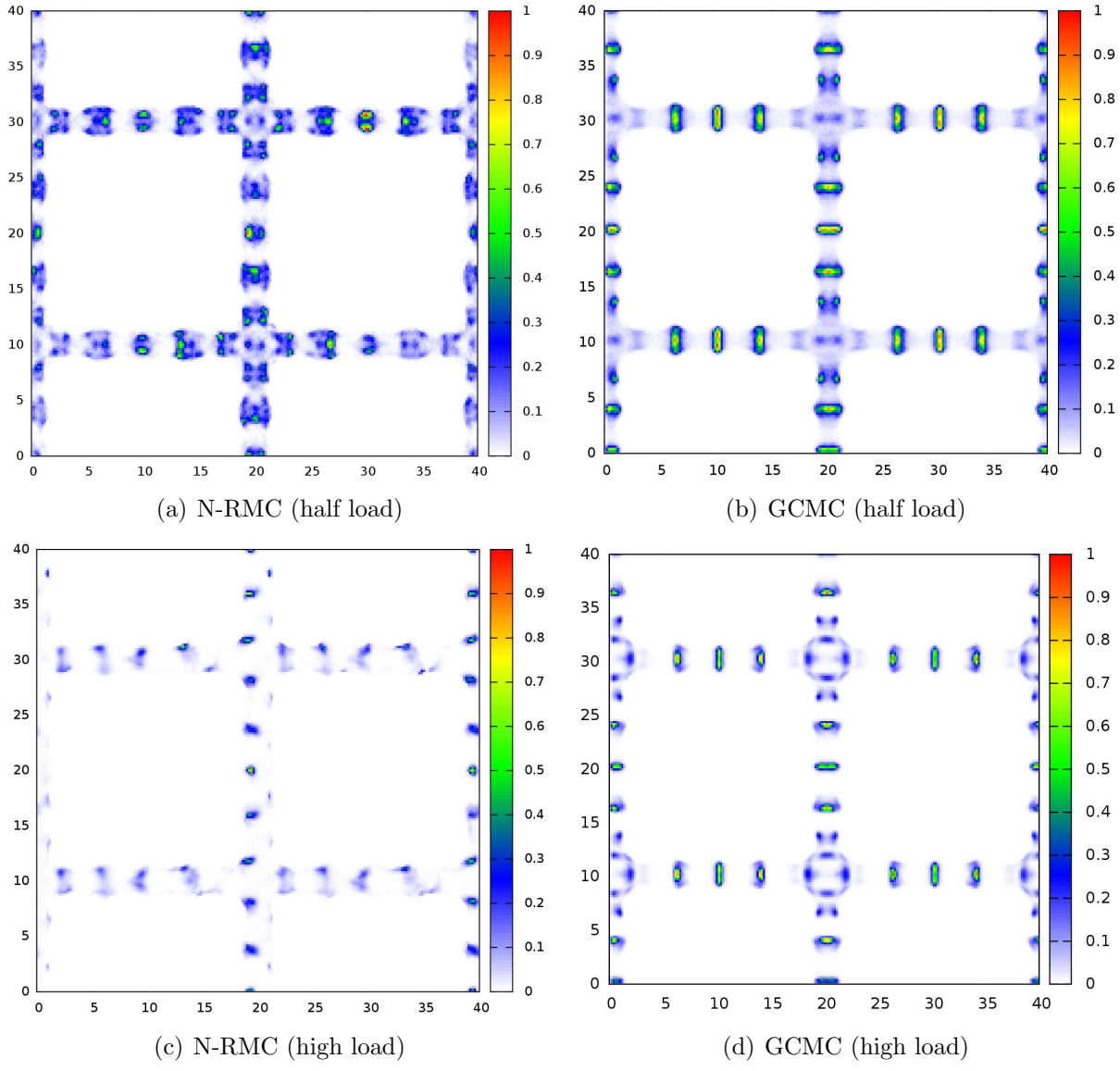

(a) N-RMC (half load)

(b) GCMC (half load)

(c) N-RMC (high load)

(d) GCMC (high load)

Figure 6.9: Probability density maps of adsorbed argon corresponding to a slab of thickness 1.5 Å parallel to the xy plane and centered at z_0 =23.4 Å.

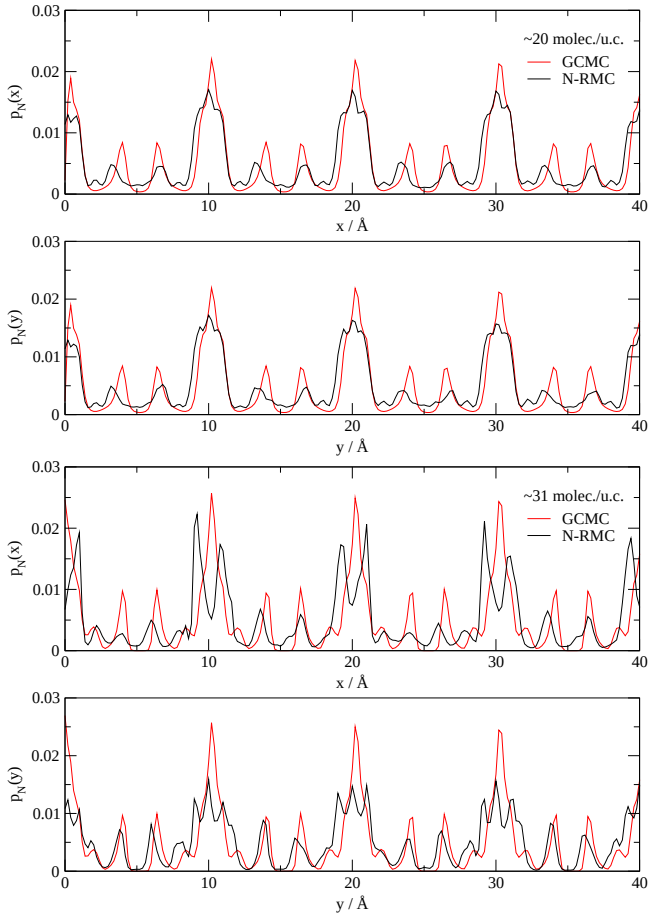

Figure 6.10: Density profiles of Ar on MEL along the x and y axes at half (two top panels) and high loads (two bottom panels) at 77 K.

integrated profiles, are obtained when the adsorbed atoms are rotated and translated, so that adsorbed particles in the x-channels are now located at the y-channels and vice versa. This indicates that simulations starting from a different seed will invariably give the same results except for a possible exchange of the x and y integrated profiles. The robustness of our results was also checked by performing an N-RMC simulation starting from a configuration from GCMC simulations. These simulations converged to a equivalent structural model, exhibiting again different density profiles along the x and y axes, as the one just discussed.

The distinct profiles along the x and y axes predicted by N-RMC might be the way in which our frozen zeolite model attempts to capture a structural change in the zeolite that breaks its tetragonal symmetry. Even though these profiles were obtained from simulations in which the zeolite was kept frozen, N-RMC might still be able to grasp the effect of small zeolite structural changes through the fitting of the experimental diffraction pattern.

Finally, with the aim of better visualizing the distribution of argon atoms within the zeolite pores, we have also calculated three-dimensional density distribution maps. Fig. 6.11 shows the higher density probability regions for GCMC and N-RMC in a fragment of the zeolite. According to GCMC, the adsorbate can be found in the channels with similar likelihood both at the edges and at the center. However,

at the edges of the intersections there seems to be a preference

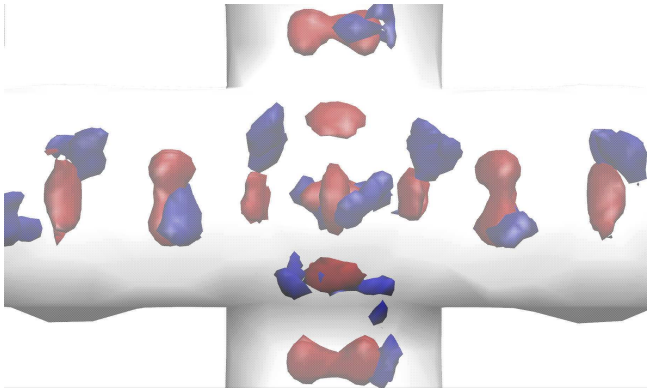

Figure 6.11: Three-dimensional density distribution plot of argon on MEL, as predicted by GCMC (red) and N-RMC (blue). The coloured regions represent isosurfaces of density.

for central positions. N-RMC, on the other hand, shows that argon atoms in the channels tend to be somewhat closer to the pore walls. In the intersections, the sites with higher probability are now at the corners, instead of at the center as in GCMC. Another fragment of the N-RMC three-dimensional density distribution maps is shown in Fig. 6.12. This picture shows the stronger tendency of the argon atoms to settle in a zig-zag configuration along the channels running parallel to the y-axis. On the contrary, along the x-channels, there is a similar probability of finding the particles at the center and at the edges of the channels and the intersections. This different arrangement of the atoms along the x and y channels explains the differences between the integrated profiles along the x and y axes.

Figure 6.12: Three-dimensional density distribution plot of argon on MEL calculated with N-RMC. The coloured regions represent isosurfaces of density.

6.5 Conclusions

In summary, we have performed TOF neutron diffraction experiments of MEL zeolite at two different loads, before and after the sub-step that appears in the adsorption

isotherm. By comparing the diffraction patterns at these two loads with that of the empty zeolite, we found that, after the sub-step, there is a strong ordering of the adsorbate. In addition to that, there are evidences of a small structural change of the zeolite.

The structural models obtained from N-RMC in conjunction with the experimental data are significantly different from those obtained by GCMC simulations, in which the Ar-Ar and Ar-zeolite interactions are described by a simple LJ model. The most significant difference is a higher propensity of adsorbate atoms to be located closer to the pore walls in the N-RMC structural models. Interestingly, this is observed both at half and high load. In addition to that, at high load, N-RMC predicts a different distribution of the atoms along the x and y channels, which suggests a zeolite structural change that breaks its tetragonal symmetry.

The fact that N-RMC and GCMC lead to different distribution probabilities of argon atoms within the pores might be reflecting deficiencies in the argon-zeolite interatomic potential used in the latter. At high load differences in the distribution density seem to arise, at least in part, from the aforementioned zeolite structural change. However, discrepancies are also evident at half load, in which case a structural change seems much more unlikely. We speculate that the origin of these deficiencies might be attributed to the fact that Ar-Si interactions are only implicitly included through the Ar-O force field, which is a widely used approximation in simulation studies of adsorption in zeolites [125]. It would be interesting to check whether the energetically favored positions are significantly different in a force field that explicitly considers Si and O atoms from those for the one used here, that only considers the oxygens. In addition to that, it is not evident that the interactions of Ar with either Si or O can be properly described with a LJ model, in particular if many body effects due to polarization contributions are to be properly accounted for.

Acknowledgements

This work was funded by Dirección General de Investigación Científica y Técnica under Grants No. FIS2013-47350-C5-4-R, MAT2012-38567-C02-01 and Severo Ochoa SEV-2012-0267. VSG also thanks the CSIC for support by means of a JAE program Ph.D. fellowship. We are thankful to Y. Mejía for performing the adsorption measurements, and to Winfried Kockelmann for kindly helping us to prepare the experimental set up to perform the TOF neutron diffraction measurements at ISIS. Fruitful discussions with Noé G. Almarza are also gratefully acknowledged.

6.6 Supporting information

In what follows, we give a detailed description of the the main steps to calculate the structure factor, and adapt the N-RMC method to use in conjunction with TOF neutron data.

6.6.1 Calculation of the structure factor

As mentioned before, we used a powder zeolite sample in our experiments. Therefore, we are measuring an orientationally averaged structure factor:

$$S(q) = \frac{2\pi^2}{NV < b >^2} \sum_{\mathbf{q}'} |F(\mathbf{q}')|^2 \delta(q - q')/q'^2 \tag{6.1}$$

where N and V are, respectively, the number of atoms and the volume of system, $\mathbf{q}'$ are the allowed vectors in the reciprocal unit cell, and $< b >$ is the average of the coherent scattering lengths of the constituent atoms, b_j. The $1/q'^2$ factor stems from the angular integration over all the possible $\mathbf{q}'$ orientations in the powder sample [35]. Finally, $F(\mathbf{q})$ contains the correlations between the scattering nuclei and is given by:

$$F(\mathbf{q}) = \sum_{j=1}^{N} b_j \exp(i\mathbf{q}\mathbf{R}_j) \tag{6.2}$$

where $\mathbf{R}_j$ denotes the position of the atom j in the unit cell.

Here we are dealing with experimental data, consequently the δ-factor in the calculated structure factor (Eq. 7.1) has to be replaced by the instrument resolution function. For TOF neutrons, it is common to use an empirical function consisting in a convolution of two back-to-back exponentials with a Gaussian function [46, 126]. All the parameters of this empirical function were fitted to minimize the difference between the calculated (using the experimental atomic coordinates reported by Terasaki *et al.* [11]) and the experimental pattern for the empty zeolite. In our implementation, these parameters remain constant along the RMC and N-RMC simulations.

For a system with partial order, such as the one considered here consisting of a crystalline solid (the zeolite) and a disordered fluid (the adsorbate), the diffraction pattern has two contributions [35]: the Bragg peaks arising from the zeolite crystal, and a diffuse contribution coming from the adsorbate and the atomic vibrations of the zeolite atoms (when such vibrations are incorporated in N-RMC modelling). Bragg peaks appear for those wave vectors allowed for the zeolite unit cell. The presence of disorder results on the emergence of diffuse intensities on those parts of reciprocal space which are forbidden for the perfect crystalline structure. Here, we evaluated this diffuse contribution using an approximate method proposed by Mellergård and McGreevy [35] that consists of averaging the intensities of those reciprocal lattice points of the simulated supercell for a certain range of q, which do not belong to the reciprocal lattice of the crystallographic unit cell (in this work, diffuse scattering was averaged over 0.1 Å^{-1}). Spurious effects on the diffraction pattern resulting from the finite size of the system are drastically reduced using this approximate method.

6.6.2 N-RMC method

Briefly, the RMC method consists in performing random particle moves that are accepted or rejected depending on whether the calculated structure factor approaches the experimental one according to the acceptance probability:

$$P^{acc} = \min\left(1, \exp\left(-\frac{\chi^2_{new} - \chi^2_{old}}{2}\right)\right), \tag{6.3}$$

where χ is a quantity that measures the deviation of the calculated and experimental structure factors, before and after the movement (χ_{new} and χ_{old}, respectively):

$$\chi^2 = \sum_{i=1}^{N_q} \frac{(S_{cal}(q_i) - S_{exp}(q_i))^2}{\sigma^2(q_i)}. \tag{6.4}$$

$S_{cal}(q_i)$ and $S_{exp}(q_i)$ are the calculated and experimental structure factors, $\sigma(q_i)$ are the uncertainties of the experimental measurement and N_q is the number of discrete points used to evaluate the diffraction pattern.

As mentioned before, the N-RMC implementation also includes particles insertion/deletion attempts, which are accepted with probability:

$$P^{acc} = \min\left(1, \exp\left(-\frac{\chi^2_{new} - \chi^2_{old}}{2} - \frac{\Delta N^2_{new} - \Delta N^2_{old}}{2}\right)\right) \tag{6.5}$$

Here, $\Delta N^2 = (N - N_{exp})^2/\sigma^2_N$, N_{exp} being the experimental estimation of number of adsorbed particles and σ_N its uncertainty.

As usual in RMC, overlaps between particles are avoided incorporating also a hard repulsive core. Move attempts that result in a particle overlap are immediately rejected.

In our implementation of RMC, the correction due to the background of the experimental data was also fitted along the simulations. This was done by renormalizing the experimental data to minimize the difference with the calculated pattern:

$$\chi'^2 = \sum_{i=1}^{N_q} \frac{(S_{cal}(q_i) - a\, S_{exp}(q_i) + b)^2}{\sigma^2(q_i)}, \tag{6.6}$$

where the parameters a and b are optimized to minimize χ'^2 using a least square fitting, and are calculated in every RMC step. Besides, we also included an additional parameter, $k_{\chi'}$, that can be used to allow for somewhat larger deviations between the calculated and measured patterns than the experimental error, thus leading to a higher mobility of the atoms and a faster sampling of the configurational space. Therefore, in our implementation, the acceptance probability is calculated as:

$$P^{acc} = \min\left(1, \exp\left(-k_{\chi'}\frac{\Delta\chi'^2}{2} - \frac{\Delta N^2_{new} - \Delta N^2_{old}}{2}\right)\right) \tag{6.7}$$

where $\Delta\chi'^2 = \chi'^2_{new} - \chi'^2_{old}$.

Given that it is rather common that the structure of the zeolite is hardly affected by the adsorbed fluid, the computational cost of the N-RMC method can be considerably reduced by keeping the atoms of the zeolite frozen during the N-RMC

simulations. However, there are increasing evidences that the structure of the zeolite can change under tight confinement conditions [1, 24] or upon the adsorption of big aromatic molecules [15, 14, 80]. In such instances, it might be necessary to include also displacements of the zeolite atoms. While doing that, it is important to incorporate bonding and bending constraints that avoid large deformations of the zeolite. In this work, the bond constraining potential is defined as:

$$U_{bond} = \sum_{i=1}^{N_{bond}} \frac{(r_{Si-O,i} - r_{0,i})^2}{2\sigma_{bond}^2}, \tag{6.8}$$

where N_{bond} is the number of Si-O bonds in the zeolite, $r_{Si-O,i}$ is the instantaneous length of bond i and $r_{0,i}$ its equilibrium bond distance. In this work, $r_{0,i}$ were assigned different values for each Si-O bond according to the experimental structure of MEL [11]. σ_{bond} is the parameter that controls the maximum deviation of the bond distances from the equilibrium value. It can also be interpreted as the weight of this term with respect to the remaining terms in the acceptance probability.

Similarly, the $O - Si - O$ angles are constrained by a bending interaction of the form:

$$U_{bend} = \sum_{i=1}^{N_{bend}} \frac{(\theta_{O-Si-O,i} - \theta_{0,i})^2}{2\sigma_{bend}^2}, \tag{6.9}$$

where N_{bend} is the number of O-Si-O bending terms, $\theta_{O-Si-O,i}$ is the instantaneous angle of bending term i and $\theta_{0,i}$ its equilibrium angle (here set to the experimental angle for each O-Si-O triplet [11]). σ_{bend} is the parameter that controls the maximum deviation of the bending angles from the equilibrium value.

When these constraints are incorporated to the N-RMC method, the acceptance probability of the zeolite atomic displacement attempts becomes:

$$P^{acc} = \min\left(1, \exp\left(-k_{\chi'}\frac{\Delta\chi'^2}{2} - \Delta U_{bond} - \Delta U_{bend}\right)\right), \tag{6.10}$$

where $\Delta U_{bond} = U_{bond,new} - U_{bond,old}$ and $\Delta U_{bend} = U_{bend,new} - U_{bend,old}$.

When the hard core overlap potential is replaced by a soft core, in this case the Weeks-Chandler-Andersen (WCA) potential [124], the acceptance probability is given by:

$$P^{acc} = \min\left(1, \exp\left(-k_{\chi'}\frac{\Delta\chi'^2}{2} - \frac{\Delta N_{new}^2 - \Delta N_{old}^2}{2} - \Delta U_{LJ}\right)\right), \tag{6.11}$$

where $\Delta U_{LJ} = (U_{LJ,new}^{rep} - U_{LJ,old}^{rep})/\sigma_{LJ}^2$, U_{LJ}^{rep} being the WCA potential and σ_{LJ} the parameter that controls the relative weight of this term.

6.6.3 Simulation details

The weights of the different terms contributing to the acceptance probability are given in Table 6.2. The overlap distances were chosen as σ_{Ar-Ar}=$0.94\sigma_{LJ,Ar-Ar}$ and σ_{Ar-O}=$0.96\sigma_{LJ,Ar-O}$, being $\sigma_{LJ,Ar-Ar}$ =3.38Å and $\sigma_{LJ,Ar-O}$ =3.1265Å. These correspond to the shortest distances for which the average pair distribution functions from Monte Carlo simulation adopt non-zero values [3].

The three-dimensional maps were built by dividing the system in a grid of width 0.2 Å. The two-dimensional maps were accumulated over a slab of thickness 1.5 Å

centered at given values of x or y, carefully chosen to section the zeolite channels longitudinally through their centers. Finally, the one-dimensional distributions along the x or y axes are constructed by integrating the three-dimensional maps along the remaining two dimensions of space. These data were averaged over 200,000 N-RMC cycles, after reaching equilibration. Typically about 25,000 N-RMC cycles are needed to attain equilibration when keeping the zeolite framework rigid and about 200,000 when the zeolite is flexible. One cycle is defined as one attempt to move each and every adsorbate atom, plus about 300 particle insertion/deletion attempts. For simulations incorporating the zeolite flexibility, it also includes attempts to move half the atoms of the zeolite.

In order to characterize the goodness of the fit obtained in a N-RMC simulation, we have evaluated the weighted profile R-factor defined as [127]:

$$R_{wp} = 100 \times \left(\frac{\sum_{i=1}^{N_q} [S_{exp}(q_i) - S_{cal}(q_i)]^2 / \sigma^2(q_i)}{\sum_{i=1}^{N_q} S_{exp}(q_i)^2 / \sigma^2(q_i)} \right)^{1/2} \tag{6.12}$$

Note that, as this factor is highly dependent on the background [128], comparison is only meaningful among different N-RMC simulations fitting the same set of experimental data.

Table 6.2: Weights of the different contributions to the argument of the exponential that determines the acceptance probability (Eqs. 6.7 and 6.10).

	$k_{\chi'}$	σ_N^2	σ_{bond}^2	σ_{bend}^2	σ_{LJ}^2
Half (hard core)	0.01	0.001	-	-	-
Half (soft core)	0.01	0.001	-	-	0.25
Half (flex. zeolite)	0.01	0.001	10^{-4}	0.1	-
High (hard core)	0.01	0.001	-	-	-
High (soft core)	0.01	0.001	-	-	0.1
High (flex. zeolite)	0.01	0.001	10^{-4}	0.1	-

Chapter 7

Experimental and simulation studies of the stepped adsorption of toluene on pure silica MEL zeolite

J. Phys. Chem. C, **submitted** (2015)

Vicente Sánchez-Gil[1], Eva G. Noya[1], Alejandro Sanz[2], Sheima J. Khatib[1], José María Guil[1], Enrique Lomba[1], Ramona Marguta[1], Susana Valencia[3]

[1] *Instituto de Química Física Rocasolano, Consejo Superior de Investigaciones Científicas, CSIC, Calle Serrano 119, 28006 Madrid, Spain*

[2] *Instituto de Estructura de la Materia, Consejo Superior de Investigaciones Científicas, CSIC, Calle Serrano 123, 28006 Madrid, Spain*

[3] *Instituto de Tecnología Química (UPV-CSIC), Avda. de los Naranjos s/n,E-46022 Valencia, Spain*

Abstract

In this work, the adsorption of toluene on pure silica ZSM-11 zeolite is investigated using a variety of experimental and simulation methods. Firstly, we measured the volumetric and calorimetric curves at 301 K and at 315 K. The adsorption isotherm presents a sub-step at a loading of roughly 4 molecules per unit cell that shifts to higher pressures at higher temperatures, and that coincides with a sudden increase in the adsorption isotherm. Grand Canonical Monte Carlo simulations reveal that the sub-step at half load is caused by the adsorption of toluene molecules at different energetic sites within the porous network. According to this, toluene molecules occupy first the intersections and, once all intersections are filled, additional toluene molecules place themselves within the channels. The structure of the adsorbate/adsorbent system was further investigated by performing X-ray diffraction experiments of the zeolite at three different loads: empty, at half load (before the

sub-step) and at high load (after the sub-step). Numerous new low intensity peaks and splittings of existing peaks at the empty and half loaded diffractograms appear in the diffraction pattern of the high loaded sample. Atomic structural models compatible with the experimental spectra were obtained by performing N-Reverse Monte Carlo simulations. Whereas at half load a good fit of the experimental diffraction pattern could be obtained using the rigid zeolite approximation, at high load, this was only possible when incorporating the flexibility of the zeolite. In this structural model, the channel cross sections are deformed from a nearly circular shape in the empty zeolite to a more elliptical shape in the case of the high loaded zeolite. Probably due to this deformation of the zeolite, toluene molecules in the channels adopt different orientations in the N-Reverse Monte Carlo and in Grand Canonical simulations (that not include the flexibility of the zeolite).

7.1 Introduction

The adsorption of aromatic molecules on ZSM zeolites has important industrial applications [129, 130, 131]. As the size of aromatic molecules is comparable to the pore size, they provide an excellent route to study the zeolite shape selectivity [132, 133, 134]. Motivated by this, numerous experimental [135, 132, 136, 137, 138, 139, 140, 141], theoretical and simulation [142, 143, 144, 23, 145] studies have been performed with the aim of understanding the adsorption process of this type of molecules, mostly on ZSM-5 (MFI framework) zeolites. ZSM-5 has a three-dimensional porous network formed by the intersection of straight and sinusoidal channels running in perpendicular directions. Linear channels have an approximately circular section of dimensions 0.54×0.56 nm, whereas sinosoidal channels adopt a slightly more eliptical shape of size 0.51×0.55 nm [135].

Early studies showed that the adsorption of p-xylene on ZSM-5 zeolites exhibits a stepped isotherm (type VI) [**?**] with a sudden increase from about 4 to 6.5-8 molecules per unit cell, with the exact location of the transition depending on the Al content of the zeolite [135, 146]. Initially, this step was attributed to a fluid-like to solid-like transition of the adsorbate. [146] However, X-ray diffraction measurements revealed that the adsorption of p-xylene induced a structural change on the zeolite [80]. ZSM-5 is known to adopt a monoclinic (MONO) structure at low temperature [15] that reversibly transforms to orthorhombic (ORTHO) with point group symmetry $Pnma$ [14] at 380K. ZSM-5 loaded with p-xylene also exhibits an orthorhombic structure but with point group symmetry $P2_12_12_1$ (PARA) [80]. In this configuration, the sinusoidal channels are deformed adopting more elliptical cross sections with dimensions (6.15-6.35)×(4.58-4.76) Å. This allows a better accommodation of the p-xylene molecules. According to this, the step would be caused by the porous heterogenity, the first four molecules occupying positions at the intersections and subsequent ones at the sinusoidal channels. Grand canonical Monte Carlo simulations corroborate this view [23].

Similar steps were observed in the adsorption isotherms of benzene and toluene on silicalite-1 (pure silica ZSM-5) [132, 139]. We note in passing that the presence of sub-steps is only noticeable in pure silica zeolites, since Al cations play the role of active acid sites controlling the process of adsorption of aromatic molecules [134]. In the case of benzene, the adsorption isotherm presents indeed two steps [139]. As for p-xylene, these steps are attributed to the absorption of the aromatic molecules in different energetic sites within the zeolite, inducing a zeolite structural change at

high loads [23, 138]. Neutron diffraction experiments suggest that benzene molecules accommodate first at the intersections, then at the straight channels and finally at the sinusoidal channels, the molecules in the channels occupying positions close to those at the intersections and forming dimer-like structures [138]. Simulations predict that in the ORTHO structure, benzene goes initially to the intersections, and in the PARA configuration, intersections and sinusoidal channels fill simulatenously, whereas no molecules are found in the straight channels [23]. Heats of adsorptions have also been measured, however there are quantitative and qualitative differences between the data provided by different groups [140, 147, 139].

The adsorption of aromatic molecules on the structurally related ZSM-11 zeolite has been more rarely studied [134], which might be attributed to the difficulty posed by its synthesis [11]. ZSM-11 has a porous network rather similar to that of ZSM-5, with the difference that now the two sets of intersecting pores are straight, with nearly circular cross sections of dimensions 0.53×0.54 nm. Therefore, it is to be expected that they exhibit a rather similar adsorption behaviour to ZSM-5, but, as its porous geometry is simpler, it might be easier to understand how the adsorbate molecules distribute along the porous network. As in the case of ZSM-5, it is foreseable that adsorption of aromatic molecules induce structural changes on ZSM-11. These changes have not yet been so well characterized as those of ZSM-5. There are, however, experimental evidences of their occurence upon increasing the temperature [98, 11, 99] and upon the adsorption of argon at liquid nitrogen temperature [7].

The objective of this work is to investigate the adsorption of toluene on pure silica MEL at room temperature. Firstly, we perform volumetric and calorimetric experiments that show that, indeed, the adsorption of toluene on MEL presents a sub-step at intermediate loads. This sub-step coincides with an increase of the heat of adsorption. The microscopic origin of the sub-step in the adsorption isotherm is investigated by grand canonical Monte Carlo simulations using emprirical potentials.

In addition to that, with the aim of obtaining experimental information about the structure of the adsorbent/adsorbate system, we carry out X-ray diffraction experiments of the loaded zeolite, before and after the sub-step in the adsorption isotherm. Traditionally, structural models of the adsorbed fluid were obtained using the Rietveld refinement methods or using molecular simulation (see, for example, Refs. [142, 143, 141, 138]). Instead, here we use the Reverse Monte Carlo method [39]. Since it was proposed in 1998, this technique has been widely used to eluciadate the structure of liquids and amorphous materials [148], as well as that of crystalline materials with partial disorder [119, 35, 120]. Some of us have recently proposed an extension of the method, the N-RMC, designed to avoid the diffusion problems that appear when studying the structure of fluids in tightly confined media [5]. The usefulness of this approach has been proven by studying the structure of argon on MEL at liquid nitrogen temperature in conjunction with experimental time-of-flight (TOF) neutron diffraction patterns [7]. We intend to show that this method is also valid for larger adsorbates, such as toluene, and for other diffraction techniques, such as X-ray powder diffaction.

7.2 Experimental measurements

7.2.1 Volumetric and microcalorimetric experiments

Measurements were performed on an expressly synthesized pure silica ZSM-11, hereafter denoted as ZSM-11(Si) sample. Details of the synthesis of the ZSM-11(Si) sample are reported elsewhere [101]. A micropore volume of 0.12 cm^3/g has been determined for this sample [101].

In an adsorption experiment, small doses of vapour were successively added at increasing pressures, measuring simultaneously the amount adsorbed and the heat generated in each dose. The heat of adsorption was measured in a Tian-Calvet type microcalorimeter (model C-80, Setaram, France) and the amount of gas adsorbed was determined in a volumetric apparatus, coupled to the microcalorimeter, equipped with a pressure transducer (Baratron 310, MKS, USA), 0-0.133 MPa range, as described in detail elsewhere [149]. Reproducibility in the measurement of amount adsorbed, determined by successive helium expansions, was better than 0.2 μmol; reproducibility of the calorimetric measurements, estimated from the mean deviation of a series of helium expansion experiments, was of the order of 2 mJ.

After correction for the so-called heat of compression, associated to the gas entrance into the cell, the isosteric heat of adsorption, q_{st}, was calculated. It is a quantity thermodynamically well defined that can be directly compared with that obtained from a family of adsorption isotherms at different temperatures [150]. In this way, the volumetric isotherm, n^{σ} – p, and the differential calorimetric isotherm, q_{st} - n^{σ}, were obtained.

Before each experiment, the samples were heated in oxygen flow, c.a. 30 cm^3/min, up to 450°C, and kept at this temperature for 4h to eliminate the hydrocarbon remainder from the previous experiment. After that, the sample was outgassed overnight at 723 K in a vacuum lower than 1 mPa.

Amounts adsorbed are expressed as milimoles of molecules per gram of sample dried under vacuum at 450°C.

7.2.2 X-ray diffraction experiments

X-ray diffraction experiments were conducted at the high resolution Materials Science and Powder Diffraction beamline at ALBA facilities. Three samples were prepared *ex situ*, namely, the empty zeolite and the zeolite with adsorbed toluene at half (3.5 molec./u.c.) and high load (6 molec./u.c.). They were contained in glass capilars that were subsequently sealed. The beamline had a wavelenght of 0.9537331 Å and data were collected at 0.002° angular increments. During data acquisition, samples were rapidly rotating to avoid the existence of a preferent orientation. In each measurement, diffraction angles, 2θ up to 40° were swept. This corresponds up to about 4.51 $Å^{-1}$. At each angle increment, counts were collected over half a minute, so that each measurement lasted about 2 hours. In addition to the three zeolites samples mentioned above, we also measured one empty capilar to subtract its contribution from the diffraction pattern measurement of each sample. Note that as the capilars are made of glass (i.e. an amorphous material), they will produce a gaussian-like diffraction pattern.

Table 7.1: Parameters of the OPLS model for toluene [22].

	ϵ/k_B (K)	σ (Å)	q (e)
C	35.247	3.550	-0.115
CH_3	85.599	3.800	0.115
H	15.106	2.420	0.115

7.3 Simulations

7.3.1 Grand canonical Monte Carlo simulations

In this work, toluene was described using the OPLS rigid all-atom model [22]. The geometric parameters of toluene molecule are given in Fig. 7.1. In this model, a Lennard-Jones (LJ) center plus a point charge are located at each atomic position. The parameters of the model are given in Table 7.1. As usual in simulations of adsorption processes, we considered that the positions of the zeolite atoms were kept frozen. Interactions between toluene and the zeolite take into account explicit dispersion interactions only with oxygen atoms (this is justified by the fact that silicon atoms are always buried within oxygen tetrahedra). However, electrostatic interactions between the adsorbate and both oxygen and silicon atoms have been considered. This model has been shown to reproduce the low pressure region (i.e. the region that follows Henry's law) of the toluene adsorption isotherm on silicalite-1 [144].

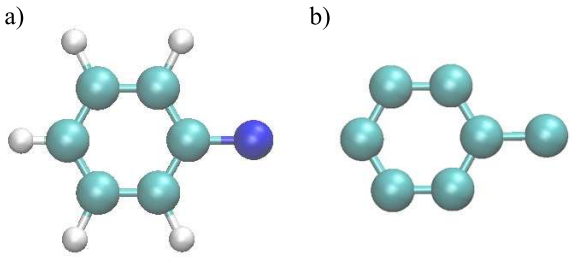

Figure 7.1: Schematic representation of the toluene molecules models used in this work: a) the all-atom model proposed by Jorgensen [22] b) the unified-like model used in the *N*-RMC simulations. For computational convenience, in this case, we have chosen the same size for the CH and CH3 centers.

A review of the bibliography reveals that the silicon and oxygen atoms have been assigned quite different values. For example, Rungsirisakun *et al.* assigned -1.0e to oxygen and +2.0e to silicon when studying the adsorption and diffusion of benzene in several siliceous zeolites, including FAU, MFI and MCM-22. The same values were also used by Kolokathis *et al.* [151] and Snurr *et al.* [23]. Fairly silimar values for the charges are given in the Kramer potential for zeolites (+2.2e for silicon and -1.1e for oxygen) [103]. However, other authors allocate quite different charge values. For example, the Nicholas model assigns a charge +1.1e for Si and -0.55e for O [26]. Given that the electrostatic terms have a relatively small contribution to the energy

Table 7.2: Cross interaction parameters for the oxygen-toluene LJ potential [23]. In addition to the LJ interaction between toluene and oxygen atoms, the zeolite-adsorbate interactions also include electrostatic terms between toluene and zeolite oxygen and silicon atoms. We assigned oxygen atoms a charge of -1e and +2e to silicon atoms.

	ZSM-5 (from Ref. [23])		ZSM-11 (this work)	
	ϵ/k_B (K)	σ (Å)	ϵ/k_B (K)	σ (Å)
C-O	73.553	3.007	97.3111	3.280
CH_3-O	80.317	3.364	106.259	2.932
H-O	49.056	2.604	64.901	2.539

(less than 10%), for consistency, we have chosen to use the same charges as Snurr *et al.* [23].

The adsorption isotherm was evaluated by means of Grand Canonical Monte Carlo (GCMC) simulations. The simulation box was built replicating the zeolite unit cell in the three dimensions of space to obtain a 2×2×3 supercell. The atomic coordinates of the zeolite in the unit cell were taken from the bibliography [11]. Simulations with the rigid zeolite consisted of 10^5 MC cycles for equilibration, plus another 10^6 cycles for taking averages. One MC cycle is defined as 100 particle insertion or deletion attempts, plus another 100 attempts to traslate or rotate one toluene molecule. We used a cavity bias algorithm to accerelate the sampling in the GCMC simulations [23].

The isosteric heat of adsorption was evaluated using the energy/particle fluctuations route [112]. Besides that, we also calculated average pair distribution functions. In particular, we focused on C-C, C-CH_3, CH_3-CH_3, C-O, C-H, and C-H_3 functions.

7.3.2 N-Reverse Monte Carlo (N-RMC) modelling

The N-RMC method is a variant of RMC modelling [39] specifically designed to deal with tightly confined media. As the method has already been detailed elsewhere [5, 7], only a brief description is provided here. In short, the N-RMC method consists in performing, in addition to particle/molecule displacement and rotation move attempts, insertion and deletion attempts of adsorbate molecules. These are accepted or rejected depending on whether the calculated diffraction pattern approaches the experimental one or not, before or after the move attempt. The incorporation of adsorbate insertion/deletion moves allows to circumvent the problem of slow diffusivities that usually appears under tight confinement conditions.

The theoretical X-ray powder diffraction patterns were calculated using the orientational averaged structure factor [35]. The parameters that allow to calculate the dependence of the atomic form factors on the scattering vector were taken from the International Tables of Crystallography. The instrumental resolution was included by modelling the peak-shape with a pseudo-Voigt function. The variation of the instrumental broadening of the peaks with the scattering angle was estimated using an expression proposed by Gaglioti *et al.* [**?**]. When the atoms of the zeolite are kept frozen, the Debye-Waller factor is introduced to model their atomic vibrations. A detailed description of the theoretical calculation of the X-ray diffraction patterns

is provided in the Supporting Material.

Toluene molecules are described using a seven-site rigid model, shown in Fig. 7.1 b). Hydrogen atoms are ignored because they are almost invisible to X-ray diffraction. The C-C and C-CH_3 bond distances are chosen the same as those in the Jorgensen model used in the GCMC simulations [22]. As usual in RMC, overlap between atoms is avoided by introducing hard-cores, so that a move attempt is inmediately rejected if it leads to overlaps. For simplicity, we have assigned the same size to CH and CH_3 centers. In particular, we have chosen $\sigma_{CH} = \sigma_{CH3}$=2.9Å and $\sigma_{CH-O} = \sigma_{CH_3-0}$=2.52Å. This is a reasonable choice, as pair distribution functions calculated from GCMC indicate that these functional groups can be approximated by same size sites.

Simulations were performed using a custom-made code. Given that the most time-consuming part of the simulations is the evaluation of the structure factor (including the evaluation of the resolution peak-shape function) and this is suitable for a q-space parallelization, we implemented the code in CUDA so that it could be run on a GPU. On a Nvidia GeForce GTX 590 GPU with 960 cores, the parallel GPU code runs 105 times faster than the serial version on an Intel Core Quad CPU at 2.66 GHz for the typical system size used in this work ($N \approx 5000$, N being the number of particles in the system).

Two types of N-RMC simulations were perfomed in this work. At half load, we have used the approximation that the zeolite was frozen, whereas, at high load, we also incorporated the flexibility of the zeolite. In order to avoid large deformations of the zeolite structure, restraints over the Si-O bond distance and Si-O-Si bending angles were introduced [7]. The initial simulation box was built by replicating the experimental unit cell [11] in the three dimensions of space to obtain a 4×4×6 supercell. Typically it takes about 10,000 N-RMC cycles to attain equilibrium in simulations with the rigid zeolite and about 100,000 when the zeolite is flexible. To keep computational time within reasonable limits, the calculated diffraction pattern was only fit up to a diffraction wavevector of 3.5 $Å^{-1}$.

7.4 Results

7.4.1 Volumetric and calorimetric experiments

Volumetric adsorption isotherms of toluene on ZSM-11(Si) at T=301 K and 315 K are plotted in Fig. 7.2 (top panel). The isotherms present an initial vertical slope where not detectable amount of adsorbate remained in the gas phase. That is an indication of a strong adsorption interaction taking place. Isotherms at the two temperatures run together in this region. This is followed by a second zone that starts at around 0.61 mmol/g when the isotherm departs from the vertical line as if reaching a saturation state. (The shape reminds a type I isotherm). However, that point corresponds to a packing density, d_{pck}= $n^{\sigma}_{\mu p}/V_{\mu p}$, $n^{\sigma}_{\mu p}$ being the amount adsorbed on the micropores and $V_{\mu p}$ the micropore volume, inside the micropores of c.a. 5.1 mmol/cm^3. This value is around half the liquid molar density at these temperatures (9.33 and 9.19 mmol/cm^3 at 301 K and 315 K, respectively). In consequence, it cannot be ascribed to completion of micropore filling. Moreover, in this second zone of the isotherm, at somewhat higher relative pressures, an unusual sudden increase of amount adsorbed appears. It is evident at both temperatures

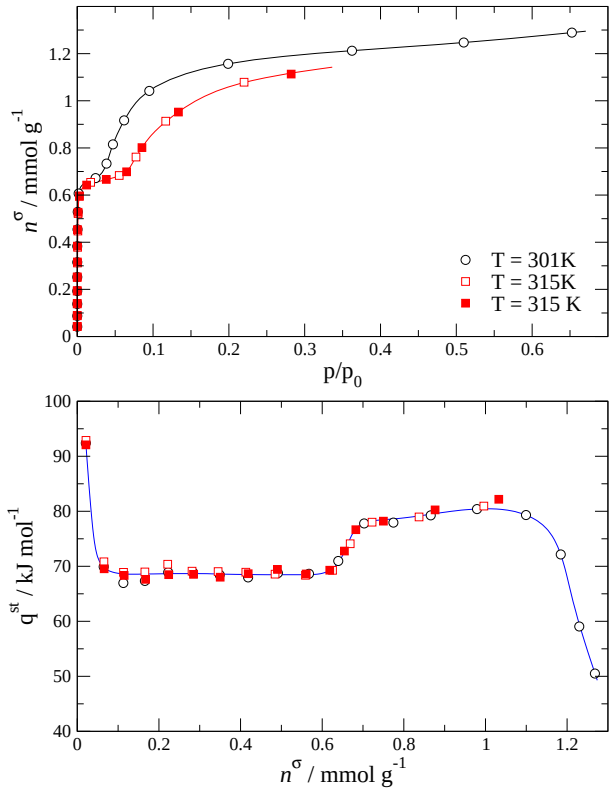

Figure 7.2: Experimental volumetric (top panel) and differential calorimetric adsorption isotherms of toluene adsorption on MEL. Two independent measurements were performed at T=315 K to show its reproducibility.

although it started at lower relative pressure at 301 K. After that, the final part of the isotherms behaves as usual: smooth increase of amount adsorbed at high relative pressures. This later behaviour corresponds to weaker adsorption on the surface so that adsorption is lower at higher temperature because equilibrium is displaced to desorption. It is remarkable the reproducibility of the isotherms at 315 K and the presence of the jump in the amount adsorbed in the two measurements. The presence of the steps and the lack of hysteresis during desorption characterize these isotherms as type VI.

The corresponding differential calorimetric isotherms at the two temperatures are shown in Fig. 7.2 (bottom panel). A narrow initial region, 0-0.04 mmol/g, of high adsorption heat is ascribed to a very small amount of irregularities on the zeolite crystals (Fig. 7.2). This is followed by a plateau at 68.5 kJ/mol in the range 0.04-0.61 mmol/g . This region corresponds to adsorption on the very regular and homogeneous microporous network of these materials as it is the case of our pure silica sample. After that, in many occasions, a final smooth increase of the adsorption heat due to lateral interactions is detected before the final fall that indicates the completion of micropore filling. However, in our case of toluene/ZSM-11(Si) the adsorption behaviour is different: at c.a. 0.61 mmol/g the heat of adsorption sharply increases from the plateau at 68.5 kJ/mol to reach 78.0 kJ/mol at ca. 0.70 mmol/g. A quasi-plateau follows to end in the final fall of the adsorption heat. This last decline is very steep in this case because the sample almost lacks of mesoporosity. From this part, a value of 1.13 mmol/g is approximately estimated as the

total uptake of the micropores. That gives a packing density value of 9.4 mmol/cm^3 when the micropores are full. It is the same value at both temperatures and slightly higher than the liquid molar density. The behaviour followed by toluene adsorption on ZSM-11(Si) is qualitatively very different from that shown on a ZSM-11(Si-Al) sample [134]. In this case, the specific strong interaction of toluene with the aluminium centres leads to a large initial decline from much higher adsorption heats. This initial fall is followed by a plateau and the final fall when micropores became full. Certainly, no second plateau at higher values of the adsorption heat shows up.

7.4.2 Grand Canonical Monte Carlo simulations

As a first attempt to provide a microscopic description of the origin of the substep at intermediate loads, we performed GCMC simulations. The simulated adsorption isotherm with the parameters proposed by Snurr *et al.* yield results that are in disagreement with the experimental data. The simulated curve is considerably shifted to higher pressures and has a plateau at 4 molec./u.c., too large as compared to the experimental results (see Supplementary Material). As first shown by Dubbledam *et al.* [152], the length of the plateau can be controlled by changing the size of the cross adsorbate-zeolite interactions. On the other hand, the adsorption isotherm can be displaced to lower pressures, by increasing the strength of the crossed interactions. Following this procedure, we obtained a new set of parameters (see Table 7.2) that give a closer agreement with the experiments, both for the adsorption isotherm and the isosteric heat (see Fig. 7.12).

However, the agreement is still not perfect. The step in the adsorption isotherm is more abrupt in experiments than in simulations. This might be due to the use of the rigid zeolite approximation, since it is likely that deformations of the zeolite framework might facilitate the upload of a larger number of adsorbate molecules without a further increase of pressure.

Regarding the isosteric heat, simulations underestimate the heat of adsorption by about 8% for all coverages. In particular, at low coverages, experiments predict a heat of adsorption of 68.62 kJ/mol, whereas simulations give a value of 63.14 kJ/mol in this region. Apart from that, simulations reproduce fairly well the shape of the isosteric heat, increasing abruptly at 4 molec./u.c., i.e., coincident with the step in the adsorption isotherm, followed by a plateau at higher loads. One of the advantages of simulations is that the two contributions to the isosteric heat, namely, the adsorbate-adsorbate and the adsorbate-zeolite terms, can be computed separately. As can be seen in Fig. 7.12, up to a load of 4 molec./u.c., both contributions remain practically constant. In this region, the toluene-toluene contribution is practically zero, indicating that the adsorbed molecules are loacted keeping large distances between them, so that their interactions are minimized. The fact that the toluene-zeolite contribution remains constant indicates that all the molecules occupy equally energetic regions within the porous network. Visual inspection of the configurations reveals that toluene molecules occupy first the intersections. As there are four intersections per unit cell, toluene molecules start to move into other regions only once all the intersections are occupied.

Above a load of 4 molec./u.c., the heat of adsorption increases. In this region, toluene-toluene and toluene-zeolite contributions show the opposite behaviour. Whereas the toluene-toluene contribution increases, indicating that toluene molecules

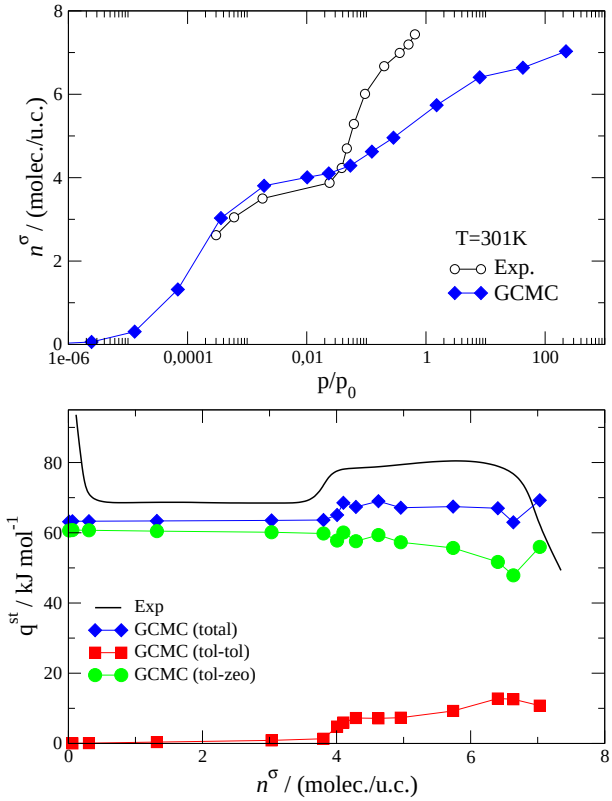

Figure 7.3: Comparison of the experimental and simulated adsoprtion isotherm (top panel) and the isosteric heat of adsorption (bottom panel) of toluene on pure silica MEL at T=301K.

are now closer and start to interact with each other, the toluene-zeolite decreases, which means that the new adsorbed molecules occupy higher energy positions within the porous network. As the increase of the toluene-toluene contribution is larger than the toluene-zeolite contribution decrease, the total isosteric heat undergoes a rather abrupt change at 4 molec./u.c. A look at a configuration snapshot reveals that molecules move into the channels once all the intersections are filled.

7.4.3 X-ray diffraction experiments

With the aim of getting further insight into the structure of the adsorbent/adsorbate, we next performed X-ray diffraction experiments. The distribution of the toluene molecules at different loads predicted by the simulations depends on the goodness of the potential models used to represent the interactions between the different species in the system. Diffraction patterns, on the other hand, provide experimental information on the atomic structure of the system, although, as we will see later, much care must be taken to correctly interpret these data. As mentioned before, diffractograms were collected at three different loads: empty, at a intermediate load (before the sub-step) and at a high load (after the sub-step). These data are shown in Fig. 7.4. The contribution of the empty capilar has already been subtracted from these data.

As can be seen in Fig. 7.4, the diffraction pattern of the zeolite empty and at half load are rather similar. The only appreciable difference between both spectra is that

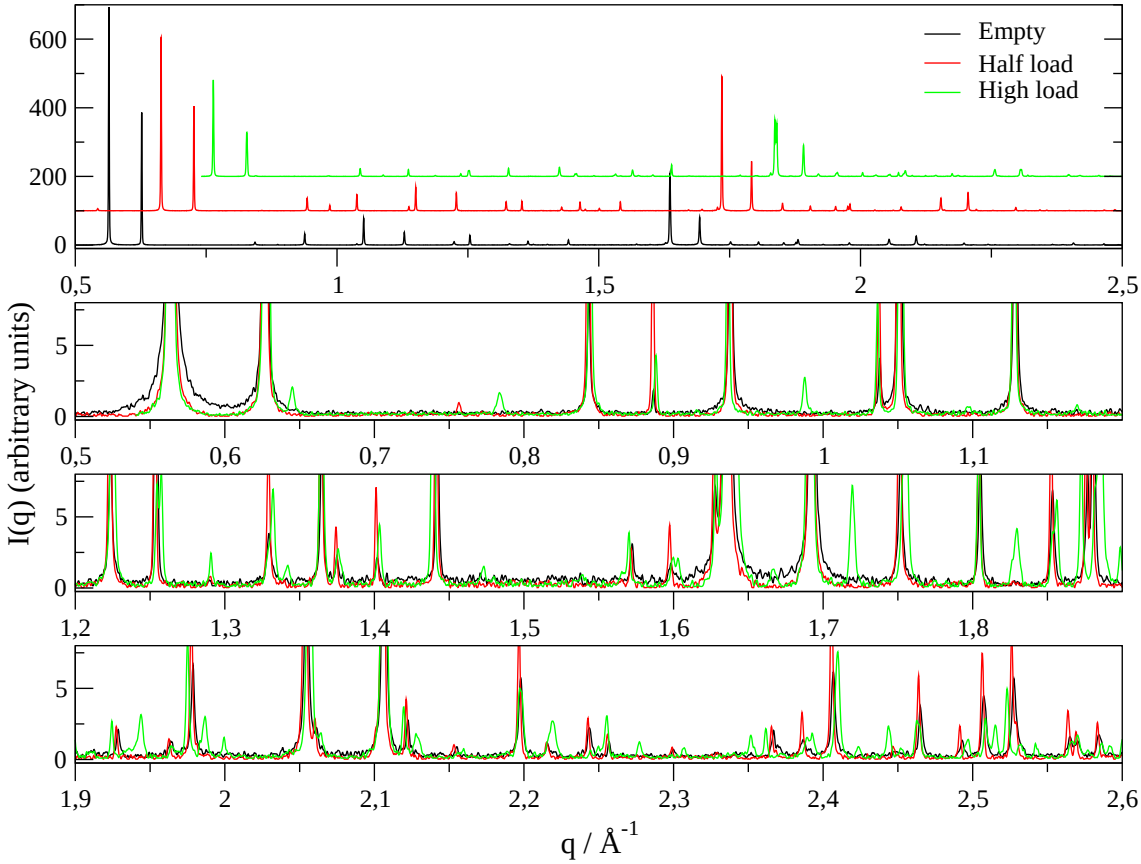

Figure 7.4: Experimental diffraction pattern of empty and loaded MEL at two different loads, before and after the sub-step in the adsorption isotherm. In the upper panel, the three diffractograms are displaced for visualization purposes. The three lower panels show enlarged views of those regions for which larger differences between the empty and high loaded zeolite.

Table 7.3: Pawley refinement of the zeolite unit cell for the three sets of experimental data.

Sample	symmetry	a (Å)	b (Å)	c (Å)
Empty	I4	20.0442	20.0442	13.3919
Half load	I4	20.0541	20.0541	13.3983
High load	I4	20.0125	20.0125	13.4165

the intensity of some peaks changes in the presence of the adsorbate. In general, the intensity increases upon the adsorption of toluene except for some reflections at low q ($\approx$ 0.55, 0.65 and 1.05 Å^{-1}) whose intensity decreases. This is due to a destructive interference between the zeolite and the zeolite-adsorbate contributions to the diffraction pattern [1, 5].

Larger differences appear at high load, after the sub-step in the adsorption isotherm. Besides changes in intensities, a few small new peaks appear at $q \approx$ 0.64, 0.79, 0.99 1.72, 1.83, 1.94, 2.21, 2.24 and 2.55 Å^{-1}. In addition to that, the splitting as well as the shift of some peaks in the range of q between 1.85 and 2 Å^{-1}, 2.4 and 2.6 Å^{-1} and 3.1 and 3.2 Å^{-1} can be observed. These new features in the diffractogram might be indicative of a subtle zeolite structural change involving a change of point group symmetry. Coincidentaly, in a previous study of adsorption of argon on MEL at liquid nitrogen temperature, we also observed changes in the diffraction pattern in the region 1.85 and 2 Å^{-1} at high load (after a similar sub-step in the adsorption isotherm as that observed here) [7].

7.4.4 N-RMC modelling

Prior to the N-RMC modelling, we performed a Pawley refinement of each of the three experimental diffraction patterns using Materials Studio package [153]. These refinements were started from the zeolite atomic structure reported by Terasaki *et al.* [11]. At high load, only those peaks present in the empty and half loaded zeolite were considered, as it is possible that the new peaks appear as a consequence of the ordering of the adsorbate. As a result of these refinements, we obtained the dimensions and the symmetry of the unit cell, the parameters of the peak shape functions and the instrumental zero offset $2\theta_0$. Table 7.4 shows the symmetry and the parameters of the unit cell, the remaining data are provided in the Supplementary Material. As can be seen, this initial refinement does not predict a change of symmetry of the zeolite upon the adsorption of toluene, even at high load. However, these results should be taken with caution as not all the peaks were considered in the refinement. The second observation is that there seems to be a slight change on the dimensions of the unit cell, specially at high load. The two equal sides, a and b, are slightly shortened, whereas the remaining side, c, is slightly enlarged. As the experimental data has very high resolution, we opted for scaling the atomic coordinates provided by Terasaki *et al.* in order to adopt the unit cell parameters obtained from the refinement for each sample. Otherwise, there would be a shift between the calculated and theoretical diffraction patterns that would prevent a proper fitting along the N-RMC simulation.

Let us start by comparing the experimental diffraction pattern of the empty zeolite to those obtained using the zeolite atomic coordinates provided by Terasaki

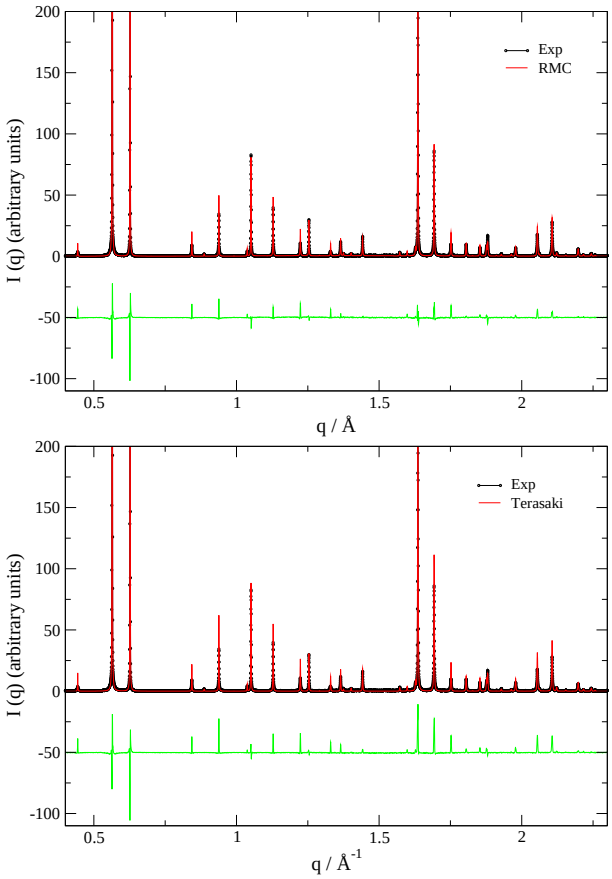

Figure 7.5: Comparison of the experimental diffraction pattern with those obtained from a RMC simulation (top panel) and using the atomic coordinates provided by Terasaki *et al.* [11] (bottom panel) for the empty zeolite. The green line at the bottom of each graph shows the difference between the experimental and theoretical diffraction patterns.

et al. [11] and from a RMC simulation. As can be seen in Fig. 7.5, the experimental diffraction pattern is reasonably well reproduced in both instances. There are only minor differences in the intensity of some peaks, that, in the region of q between 1.5 and 2 Å^{-1}, seem to be larger when using the atomic coordinates from the bibliography.

The experimental and N-RMC diffraction patterns at half load are compared in Fig. 7.6. Again, a fairly good agreement between both sets of data is obtained. As mentioned before, in this case, N-RMC simulations were conducted keeping the zeolite frozen. The good agreement between the experimental and simulated diffraction patterns corroborate that, at this coverage, this is a good approximation. As for the empty zeolite, the only discrepancy is that the intensity of some peaks is not properly reproduced. Although not shown, the calculated diffraction pattern from configurations of the GCMC simulations also reproduce fairly well the experimental diffraction pattern. An inspection of the configurations sampled along the N-RMC simulation reveals that molecules are sitting preferencially at the intersections, similarly to what is observed in GCMC simulations (see Fig. 7.7). The only difference lies in the fact that, in N-RMC, toluene molecules show a slightly higher tendency

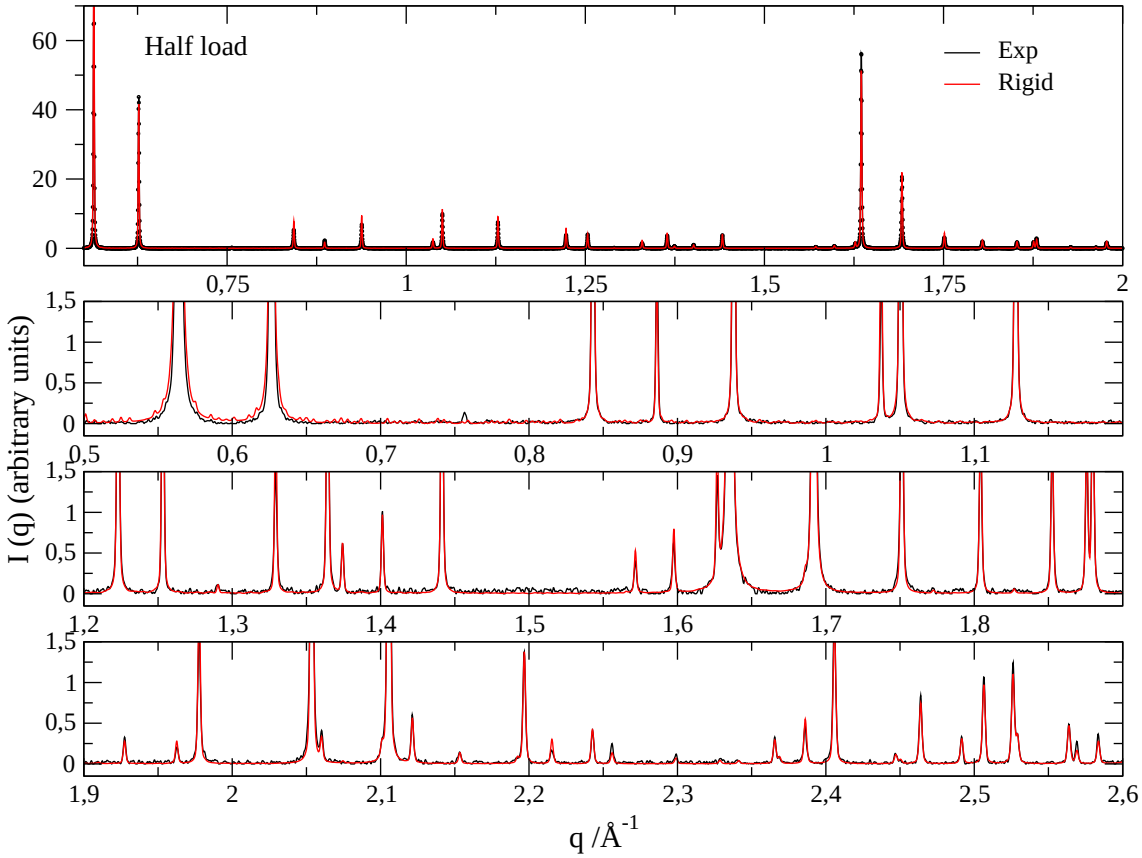

Figure 7.6: Comparison of the experimental and N-RMC diffraction patterns of the zeolite ZSM-11 at half load. The top panel shows an overall comparison of the two spectra, whereas the lower three panels show enlarged views to show the degree of agreement on low-intensity peaks.

to enter the channel edges near the intersections.

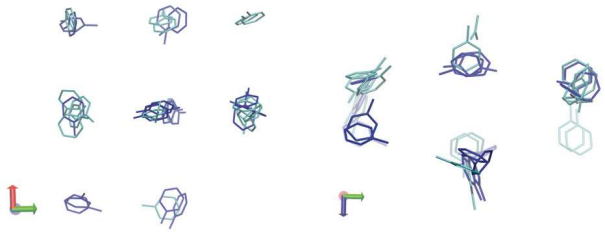

Figure 7.7: Comparison of the arrangement of toluene molecules within the zeolite porous network at half load, as predicted by N-RMC (light blue) and GCMC (dark blue) simulations. Two different views are shown, one along the z-axis (left figure) and another one along the x-axis (right figure).

At high load, N-RMC simulations using the rigid zeolite approximation were unable to provide a good fit of the experimental data. The same was true for spectra calculated from configurations obtained from the GCMC simulations described

above (data not shown). In order to keep the simulations as simple as possible, we repited the calculations but assigning a weight ten times higher in the RMC fit to the new peaks that appear in the diffraction pattern at high load. Even in this way, the calculated diffractogram reproduced only a few of those peaks (see Fig. 7.8). In general, *N*-RMC was able to fit the new reflections at q lower than 1.2 Å^{-1}, but failed to reproduce the new features at higher values of q. Therefore, the next step was to introduce the zeolite flexibility in the *N*-RMC modelling. As can be seen in Fig. 7.8, the agreement with the experimental data is now fairly good. *N*-RMC succeeds now to fit most of the new peaks in the whole range of q studied, except for the splitting of some peaks (at q≈2.39, 2.51Å^{-1} and others at higher values of q and that are not shown in Fig. 7.8).

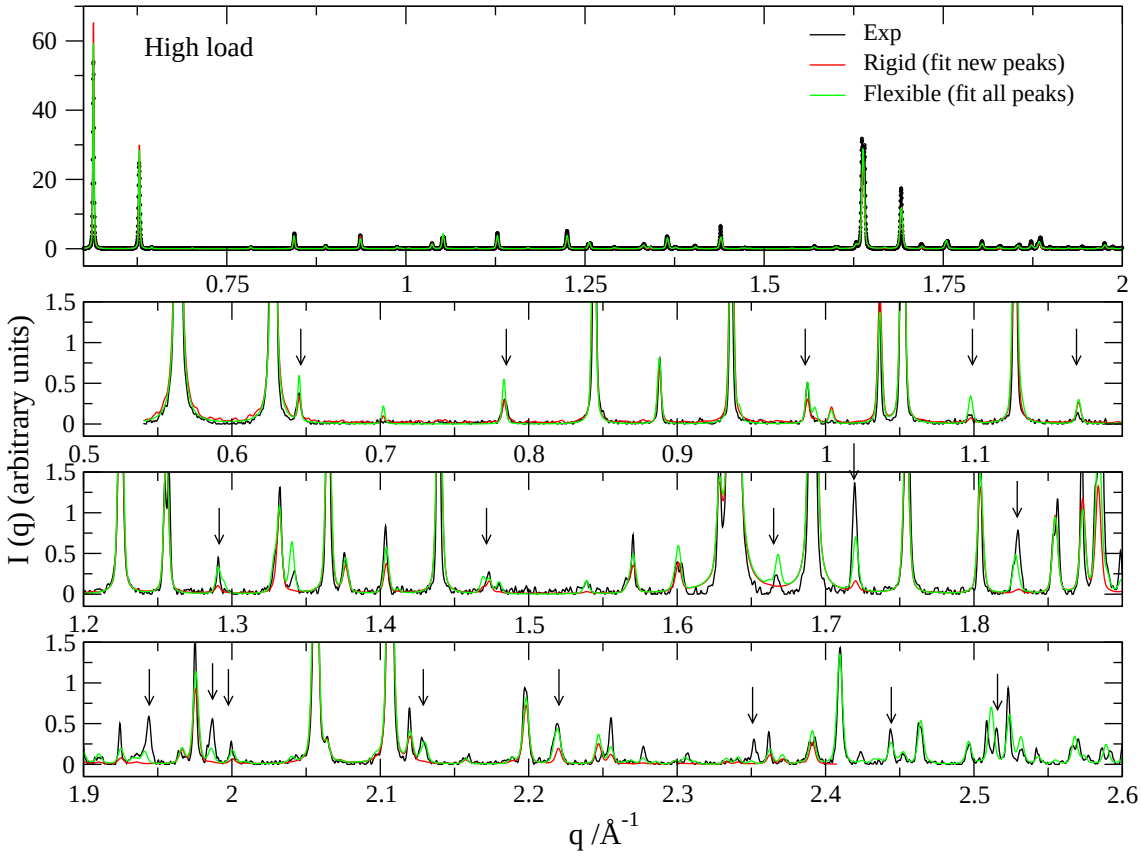

Figure 7.8: Comparison of the experimental and *N*-RMC diffraction patterns of the zeolite ZSM-11 at high load. The top panel shows an overall comparison of the two spectra, whereas the lower three panels show enlarged views to show the degree of agreement on low-intensity peaks. The arrows mark the peaks that emerge experimentally at high load, after the step in the adsorption isotherm.

The good fit obtained when incorporating the zeolite flexibility evidences the importance of introducing such effect at high load. This can be more clearly seen in Fig. 7.9, where the calculated spectra from *N*-RMC is split in its three components, the toluene-toluene, toluene-zeolite and zeolite-zeolite terms. As can be seen, the peaks reproduced with the rigid zeolite approximation arise mainly from the toluene-toluene and the toluene-zeolite contributions. However, most of the peaks at q beyond 1.2 Å^{-1}, and that are only reproduced when the zeolite flexibility is

incorporated, arise mainly from the zeolite-zeolite contribution.

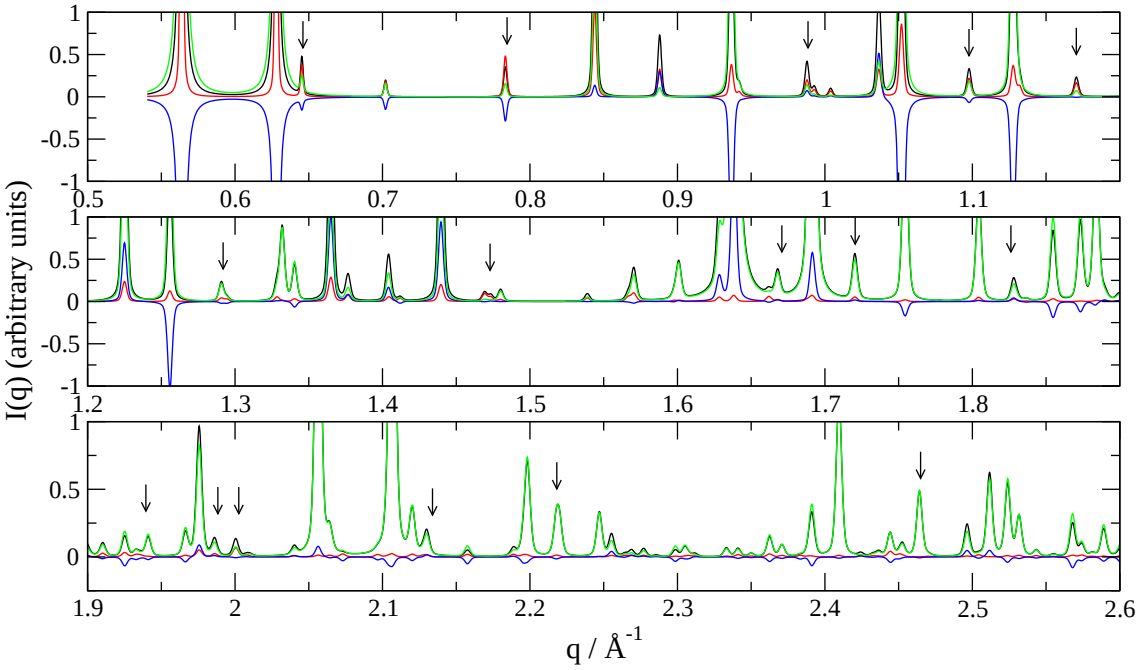

Figure 7.9: Contributions to the spectra of the loaded zeolite, as obtained from N-RMC with the flexible zeolite. Black line shows the total spectrum, the red line the adsorbate contribution, the blue line the crossed adsorbate-zeolite term and the green line the zeolite contribution.

Looking now at the arrangement of the toluene molecules in the zeolite pores (see Fig. 7.10), toluene molecules are located now both at the intersections and at the channels. Those toluene molecules at the channels show a preference to occupy channel edges (instead of the centers). They tend to be closer to the toluene molecule at the intersection, and thus form dimer-like structures. Comparison of this distribution of adsorbate molecules with that seen in GCMC simulations reveals that there is a higher probability of finding the toluene molecules in the channels in N-RMC than in GCMC simulations. Another interesting difference is that toluene molecules in the channels lie mainly on the xy plane in N-RMC configurations, whereas GCMC predicts that it is more favourable that they sit on the yz plane. We speculate that this different disposition of the toluene molecules in the channels might have its origin in the deformation of the zeolite. This deformation is accounted for in N-RMC but not in GCMC simulations.

Finally, a look at the configuration of the zeolite reveals that the deformation is indeed quite subtle (see Fig. 7.11). The main difference between the structure of the empty zeolite [11] and that of the high loaded zeolite is that the cross section of the channels that was almost spherical in the empty structure adopts now a more elliptical shape. A closer inspection reveals that the shape of the cross sections of all the channels is not equal, there is some dispersion across the simulation box. The distance between opposite oxygens on the 10-member rings of the channels ranges from 8.1 to 8.4 Å in the empty zeolite, against 7.4 to 8.5 Å in the loaded zeolite (measured from the center of the oxygen atomic positions). This deformation is similar to that found in ZSM-5 when loaded with p-xylene [80].

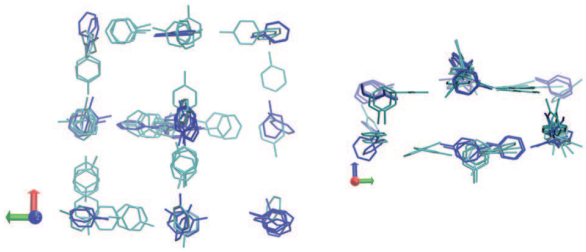

Figure 7.10: Comparison of the arrangement of toluene molecules within the zeolite porous network at high load, as predicted by N-RMC (light blue) and GCMC (dark blue) simulations. Two different views are shown, one along the z-axis (left figure) and another one along the x-axis (right figure).

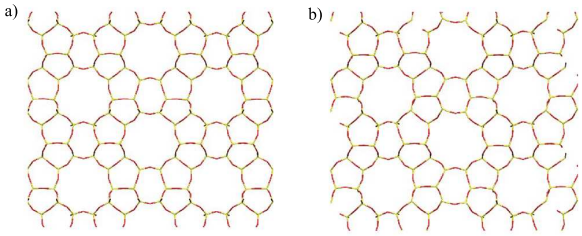

Figure 7.11: Comparison of the zeolite structure provided by Terasaki *et al.* (left figure) and that obtained from N-RMC modelling at high load (right figure).

7.5 Summary and conclusions

In this work, we have measured the volumetric and calorimetric curves of the adsorption of toluene on pure silica ZSM-11 at T=301 K and 315 K. The adsorption isotherm presents a sub-step at a loading of approximately 4 molec./u.c. that shifts to higher pressures at higher temperatures. This substep coincides with a sudden increase in the heat of adsorption. GCMC simulations modelling both the zeolite and toluene molecules as rigid entities give results in qualitative agreement with experiments. The sub-step in the adsorption isotherm is less pronounced than in experiments and the heat of adsorption is slightly underestimated at all coverages. Nevertheless, GCMC simulations allowed us to relate the step in the adsorption isotherm to the adsorption of toluene molecules on different sites of the porous network. According to GCMC simulations, toluene molecules occupy the intersections and only when all the intersections are filled (at a loading of 4 molec./u.c.), the adsorbate starts to populate also the channels. The sudden increase of the heat of adsorption at this coverage is due to an increase in the adsorbate-adsorbate interactions that is not completely compensated by the fact that toluene molecules are placed now at more energetic positions in the intersections.

The structure of the adsorbate/adsorbent system was further investigated by measuring the X-ray diffraction pattern of the zeolite at three different loads: empty, at half load (before the sub-step) and at high load (after the sub-step). Comparison of the three diffractogram reveals that there are numerous low intensity peaks that appear only at high load, including the splitting of some of the already existing peaks.

These splittings are often due to zeolite structural changes. Using as target these experimental diffractograms, structural models of the zeolite at half and high load have been obtained. At half load, the structure of the adsorbate/adsorbent system is rather similar to that obtained from GCMC simulations, except for perhaps a slightly higher probability of finding toluene molecules at the edges of channels in N-RMC. At high load, a good fit of the experimental diffraction pattern could only be obtained when incorporating the flexibility of the zeolite. In this case, toluene molecules show a much higher tendency to be located at the channels than in GCMC simulations. Interestingly, the orientation of toluene molecules also differs in N-RMC and GCMC modelling. Whereas in the case of N-RMC toluene molecules lie on the xy plane, they are oriented with the ring on the yz plane in GCMC simulations. We attribute the different orientation of the toluene molecules to the zeolite structural change observed in N-RMC, a change that is precluded in our GCMC simulations. This zeolite structural change consists in a deformation of the cross section of the channels, that become more elliptical when toluene molecules are adsorbed. A similar change was observed on the structurally similar ZSM-5 zeolite upon the adsorption of p-xylene [80].

In summary, we have shown that the steps in the volumetric and calorimetric adsorption isotherms are associated with the selective adsorption of toluene molecules in sites with different atomic environment (first intersections, then channels), and there is no evidence of an adsorbate transition. Changes in the diffractogram induced by the adsorbate can only be fully accounted for if the structure of the zeolite is flexible enough to allow for channel deformations upon adsorbate intake at high loads.

To finalize, we would like to stress the usefulness of the N-RMC method to extract structural models compatible with experimentally measured diffraction patterns of adsorbed fluids on zeolites. In a previous work, we have applied this method to the adsorption of a simple gas, such as argon, in pure silica ZSM-11 [7]. In this work, we show that the method is also applicable for more complex molecules, such as toluene. We hope that these two examples encourage the use of this approach to get further insight into the adsorption properties of different porous media and, in particular, concerning the structure of adsorbates.

Acknowledgment

This work was funded by Dirección General de Investigación Científica y Técnica under Grants No. FIS2013-47350-C5-4-R, MAT2012-38567-C02-01 and Severo Ochoa SEV-2012-0267. VSG also thanks the CSIC for support by means of a JAE program Ph.D. fellowship. We are thankful to Inma Peral for kindly helping us to prepare the experimental set up to perform the X-ray diffraction measurements at ALBA.

7.6 Supplementary material

7.6.1 Theoretical calculation of the X-ray powder diffraction structure factor

As experiments are performed over a powder sample, we are dealing with an orientationally averaged structure factor[35]:

$$S(q) = \frac{2\pi^2}{NV < f >^2} \sum_{\mathbf{q}'} |F(\mathbf{q}')|^2, \delta(q - q')/q'^2 \tag{7.1}$$

where N and V are, respectively, the number of atoms and the volume of system, $\mathbf{q}'$ are the allowed vectors in the reciprocal unit cell, and $< f >$ is the average of the form factors of the constituent atoms, f_i. The $1/q'^2$ factor stems from the angular integration over all the possible $\mathbf{q}'$ orientations in the powder sample[35]. $F(\mathbf{q})$ contains the correlations between the scattering nuclei and is given by:

$$F(\mathbf{q}) = \sum_{j=1}^{N} b_j \exp(i\mathbf{q}\mathbf{R}_j), \tag{7.2}$$

where $\mathbf{R}_j$ denotes the position of the atom j in the unit cell. The dependence of the atomic form factors on the scattering vector was taken into account using the analytical expression:

$$f(q) = \sum_{i=1}^{4} a_i \exp\left(-b_i \left(\frac{q}{4\pi}\right)^2\right) + c. \tag{7.3}$$

The values of the parameters a_i, b_i and c were taken from the International Tables of Crystallography[36].

As our purpose is to model the experimentally measured X-ray diffraction pattern, the δ-function in Eq. 7.1 is replaced by the experimental resolution function. The peak-shape was modeled using a pseudo-Voigt function[126]:

$$I(2\theta) = \eta L(2\theta - 2\theta_0) + (1 - \eta)G(2\theta - 2\theta_0), \tag{7.4}$$

where $L(2\theta - 2\theta_0)$ and $G(2\theta - 2\theta_0)$ are normalized Lorentz and Gaussian functions, respectively, and η is the mixing parameter that controls the weight of each function. Here we took η =0.5. Besides, the variation of the instrumental broadening of the peaks with the the scattering angle was estimated using an expression proposed by Caglioti *et al.*[**?**] that gives the half width at half maximum (HWHM):

$$HWHM^2 = U \tan^2\theta + V \tan\theta + W. \tag{7.5}$$

The effect of thermal disorder can be taken into account, within the harmonic approximation, through the Debye-Waller factors[154]:

$$DWF = \exp(-Bq^2/3) \tag{7.6}$$

where B is the Debye-Waller factor that measures the atomic mean squared displacement. This term was taken into account in the contribution of the zeolite to the structure factor whenever the rigid zeolite approximation was used in the RMC simulations.

The parameters of the empirical functions of the peak shape, the instrumental zero offset $2\theta_0$[126] and the Debye Waller factor B have been obtained from a Pawley refinement of each experimental diffractogram using Materials Studio Package[153]. The values obtained are given in Table 7.4.

Table 7.4: Pawley refinement of the zeolite unit cell for the three sets of experimental data.

Sample	symmetry	a (Å)	b (Å)	c (Å)	U	V	W	$2\theta_0$	B (Å^2)	R_{wp}
Empty	I4	20.0442	20.0442	13.3919	0.03959	-0.00324	0.00027	0.05332	6.08997	2.92
Half load	I4	20.0541	20.0541	13.3983	0.00901	-0.00085	0.00022	0.05351	—	2.44
High load	I4	20.0125	20.0125	13.4165	-0.071	0.025	-0.0007	0.05609	—	23.19

7.6.2 Effect of the cross toluene-zeolite interactions on the adsorption isotherm and isosteric heat of adsorption

As can be seen in Fig. 7.12, the parameters of the cross toluene-zeolite interactions proposed by Snurr *et al.*[23, 144] (see Table 7.5) do not reproduce properly neither the adsorption isotherm nor the isosteric heat of adsorption of toluene on pure silica ZSM-11. The adsorption isotherm is displaced to higher pressures, and the plateau at 4 molec./u.c. is too large compared to the experimental one. The isosteric heat is considerably underestimated and, besides, it predicts a slight decrease of heat (instead of an increase, as in experiments) coincident with the sub-step in the adsorption isotherm. This is somewhat surprising as those parameters had been shown to reproduce the adsorption at low pressures of toluene on pure silica ZSM-5. We speculate that the different performance of the cross parameters in the two zeolites might arise from the similarity between the size of the toluene molecule and the pores of these zeolites. Small differences on the atomic structure of the pores can lead to quite different energies and, thus, to quite different adsorption properties.

In view of this, we decided to reparameterize the cross interactions to the volumetric and experimental data provided in this work. Diminishing the value of the cross σ parameters, the plateau at 4 molec./u.c. shortens (model 2, see Fig. 7.12 and Table 7.5)[152], although the curve is still shifted to higher pressures with respect to the experimental data. Regarding the isosteric heat, it decreases at low coverages, but, at loading of 4 molec./u.c., it slightly increases. The same is observed in experiments, with the difference that the increase of heat is higher than in simulations. The reason for this change of trend upon the change of the cross parameters is that, whereas the heat due to toluene-toluene interactions increases, the toluene-zeolite contribution decreases because new adsorbed molecules necessaroly have to go to energetically less favourable positions at the channels. When the size of the cross toluene-zeolite interaction diminishes, the energetic penalty of the toluene-zeolite contribution decreases. As a consequence, the balance between both contributions leads now to an overall increase of heat.

Finally, the adsorption isotherm can be shifted to lower pressures, and bring it in agreement with the experimental data, by lowering the strength of the cross toluene-zeolite interactions[152] (model 3, see Fig. 7.12 and Table 7.5). This also leads to an overall increase of the heat of adsorption, the simulation data again approaching the experimental measurements. Even though there is still a slight underestimation of the heat of adsorption at all coverages, it can be concluded that the agreement between experiments and simulations is reasonable now.

Table 7.5: Values of the three sets of cross parameters for the oxygen-toluene LJ interactions tested in this work. In addition to the LJ interaction between toluene and oxygen atoms, the zeolite-adsorbate interactions also include electrostatic terms between toluene and zeolite oxygen and silicon atoms. We assigned oxygen atoms a charge of -1e and +2e to silicon atoms.

	Model 1 (from Ref. [23])		Model 2		Model 3	
	ϵ/k_B (K)	σ (Å)	ϵ/k_B (K)	σ (Å)	σ (Å)	ϵ/k_B (K)
C-O	73.553	3.007	73.553	3.280	97.3111	3.280
AH_3-O	80.317	3.364	80.317	2.932	106.259	2.932
H-O	49.056	2.604	49.056	2.539	64.901	2.539

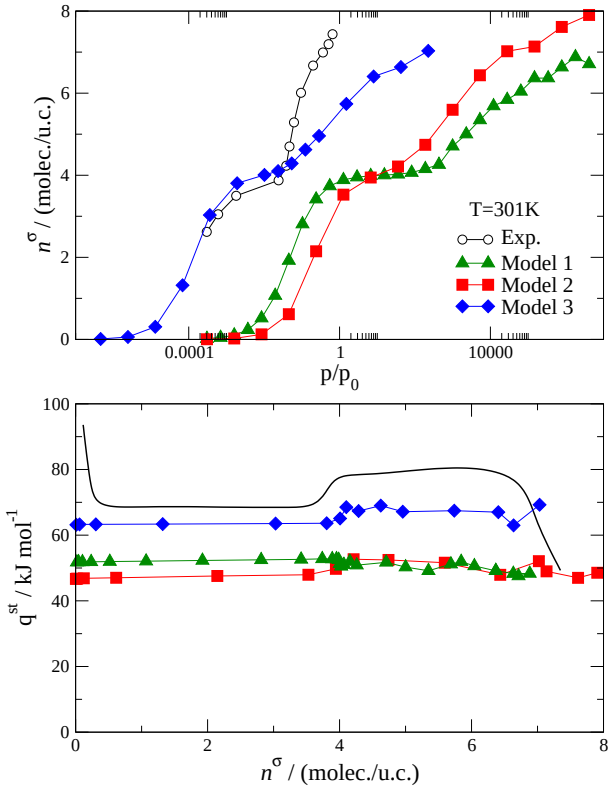

Figure 7.12: Comparison of the experimental and simulated adsorption isotherm (top panel) and the isosteric heat of adsorption (bottom panel) of toluene on pure silica MEL at T=301K, as calculated using the three sets of cross toluene-parameters given in Table 7.5.

Part IV

Conclusions

In this thesis, adsorption processes on pure silica MEL zeolite have been deeply investigated by means of a combination of experimental adsorption experiment (volumetric isotherms), diffraction measurements (neutrons and X-rays) and computer simulations (Monte Carlo and Reverse Monte Carlo). This work includes the adsorption study of both a monoatomic adsorbate without electrostatic charge (argon), as well as a polyatomic adsorbate with coulombic interactions (toluene).

Firstly, for calculating the measurable structure factor an substantial verification has been done for the so called 'crystallographic route'. It has been shown that this route can deal with system with order an disorder phases at the same time and, therefore, is the only choice for estimating the structure factor of fluids under confinement.

Secondly, an improvement to the standard RMC algorithm has been developed. This new algorithm, N-RMC, is better adapted to confined systems as the adsorbates in a zeolite framework. Using this new approach the computational time is considerably reduced as a consequence of a better sampling. Another significant efficient improvement has be done using GPU's. The evaluation of the structure factor is up to 100 times faster using the parallel code written in CUDA programming language.

Despite the apparently simplicity of the problem, GCMC simulations have revealed that none of different considered potential models, even considering a flexible zeolite framework, reproduce the abrupt experimental sub-step in the argon adsorption isotherm measured for the first time. This means that, potential energy functions are not able to mimic the real interactions involved in the adsorption process, revealing the difficulty of the problem that we are facing.

A remarkable discovery found in this thesis is that the MEL zeolite structure changes when highly confined atoms are adsorbed in its porous and cavities. In the case of argon adsorption, N-RMC simulations provide a different structural order when argon atoms are adsorbed in straight channels along different axes. Hence, the sub-step observed in the experimental isotherm can be attributed to a structural change in the zeolite framework that breaks the tetragonal symmetry of MEL zeolite.

Finally, N-RMC simulations performed for modeling the adsorption of toluene molecules on MEL zeolite, have evidenced the importance of considering the flexibility of zeolite framework to reproduce the observed changes in X-rays diffraction pattern. Moreover, as for argon adsorption, some details of the structural zeolite change have been also provided.

Conclusiones

En la presente tesis se ha profundizado en el conocimiento de los detalles que entraña la adsorción de moléculas en la zeolita pura silica MEL, combinando medidas experimentales de adsorción (isotermas volumétricas), difracción (neutrones y rayos-X) y simulaciones computacionales (Monte Carlo y Reverse Monte Carlo). Este trabajo incluye el estudio de adsorción de adsorbatos mono atomicos sin cargas electricas (argon), así como, de adsorbatos poliatómicos con interaccion de tipo Coulomb (tolueno).

En primer lugar, ha sido comprobada la validez de la 'ruta cristalográfica' para cuatro sistemas desordenados con un orden estructural creciente. Para cualquier simulación RMC consiguiente en esta tesis, ésta ha sido la ruta elegida al poder calcular el factor de estructura en sistemas con presencia de orden y desorden al mismo tiempo.

Por otro lado, hemos implementado un nuevo desarrollo metodológico del algoritmo RMC, denominado N-RMC, que mejora ostensiblemente la eficiencia en el muestreo en comparación con la clásica implementación del método. Al estar específicamente adaptado para sistemas confinados, el nuevo algoritmo reduce los tiempos de cálculo, ya de por sí, computacionalmente muy costosos. Otra importante mejora se ha conseguido al transcribir el código N-RMC al lenguaje de programación CUDA, hacieno que la evaluación del factor de estructura sea hasta 100 veces más rápida.

Las simulaciones GCMC tanto para el argon como para el tolueno, incluso consierando la flexibilidad de la zeolita, han revelado la limitación de los potenciales para describir la interacciones reales presentes en el proceso de adsorción. Pese a la aparente simplicidad del problema, los modelos no reproducen los abruptos saltos en las isotermas de adsorción, independientemente de la complejidad del potencial utilizado, resaltando así la dificultad el problema abordado.

Contrariamente a lo que cabría esperar, la zeolita MEL muestra una tendencia a adaptar su estructura cuando en sus poros se ordenan adsorbatos altamente confinados. En caso concreto del argon, las simulaciones N-RMC, para un llenado depues del salto observado en la isoterma de adsorción, muestran una ordenación diferencial de los adsorbatos en los canales rectos de una y otra dirección. Por lo tanto, los resultados parecen indicar que el salto en las isoterma de adsorción es fruto de un cambio estructural de la zeolita, evidenciando una posible ruptura de la simetría tetragonal de la zeolita.

Finalemente, en lo referente a la adsorción de moléculas de tolueno, las simulaciones N-RMC han revelado la necesidad de considerar la flexibilidad de la zeolita para reproducir los cambios observados en las medidas de difracción. Además, al igual que con el argon se han podido dar detalles cualitativos de los cambios estructurales de la zeolita.

Part V

Appendixes

Appendix A

Ewald summation

Ewald sums have been used for computing the long-range electrostatic interactions of the toluene-toluene and toluene-zeolite, as well as, Nicholas potential model for a flexible zeolite framework. First of all, we assume periodic boundary conditions and that the total system is electrically neutral. The energy of a system of charged point ions mutually interacting via the Coulomb potential, is given by

$$U_{Coulomb}(r) = \frac{1}{4\pi}\frac{q_i q_j}{\epsilon_r r} \tag{A.1}$$

Ewald summation method divides the long-range interaction in three different contributions. Firstly each ion is effectively neutralized (at long range) by the superposition of a spherical Gaussian cloud of opposite charge centered on the ion. The second modification is to superimpose a second set of Gaussian charges, this time with the same charges as the original point ions and again centered on the point ions (so nullifying the effect of the first set of Gaussians). The third one, is self energy correction, which arises from a Gaussian acting on its own site. According to this, the total electrostatic potential energy can be divided in three different terms [18]

$$U_{total} = U_{short-range} + U_{Fourier} - U_{self} \tag{A.2}$$

The combined assembly of point ions and Gaussian charges becomes the Real Space part of the Ewald sum, which is now short ranged. $U_{short-range}$ corresponds to the total contribution of the screened Coulomb interactions to the total potential energy and it is mathematically described as

$$U_{short-range} = \frac{1}{4\pi\epsilon_r}\sum_{i<j}^{N}\frac{q_i q_j}{r_{ij}} erfc(\alpha r_{ij}) \tag{A.3}$$

. The potential due to these Gaussians is obtained from Poisson's equation and is solved as a Fourier series in Reciprocal Space. The Fourier contribution to the total potential energy, $U_{Fourier}$, due to the electrostatic potential ϕ is defined as

$$U_{Fourier} = \frac{1}{2V\epsilon_r}\sum_{k\neq 0}^{\infty}\frac{e^{-k^2/4\alpha^2}}{k^2}\left|\sum_{j}^{N} q_j e^{-i\mathbf{k}\cdot\mathbf{r}_j}\right|^2 \tag{A.4}$$

Finally, the complete Ewald sum requires an additional correction, U_{self}, known as the self energy correction, which arises from a Gaussian acting on its own site, and is constant. Ewald's method therefore replaces a potentially infinite sum in real

space by two finite sums: one in real space and one in reciprocal space; and the self energy correction. This spurious self interaction must be subtracted according to

$$U_{self} = \frac{\alpha}{4\pi^{3/2}\epsilon_r} \sum_{i}^{N} q_i^2 \tag{A.5}$$

Appendix B

Synchrotron source

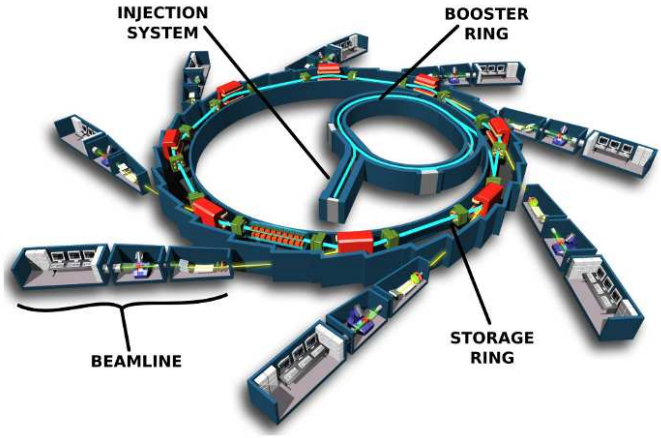

Figure B.1: General diagram of structural features of a Synchrotron (Copyright ©EPSIM 3D/JF Santarelli).

A synchrotron is a particular type of cyclic particle accelerator, in which magnetic and electric field are synchronized to focus and to accelerate a electron beam in a circular ring. Bending, beam focusing and acceleration are separated into different components in a synchrotron. Electrons are accelerated to extremely high energy and then make them change direction periodically. This way, they naturally emit a very brilliant, highly focused light at X-rays wavelengths when the moving electron beam changes direction. As can be seen in Fig. B.1, a synchrotron consists of four different parts: injection system, booster ring, storage ring and beamlines. In injection system, as synchrotrons are unable to accelerate particles from zero kinetic energy, pre-accelerated electrons are injected into the scheme. For this purpose, a linear particle accelerator (LINAC) is generally used. Electrons travel from the LINAC to the booster ring where, as they circulate in the ring, they are accelerated to nearly the speed of light by using powerful electro-magnets. The high energy electrons are transferred from the booster ring to circulate the storage ring, where the electrons emit synchrotron light every time their path is bent by the magnets inside the storage ring. Finally, the highly focused X-rays are used to study the sample structure from its diffraction pattern in a beamline.

Appendix C

Spallation source

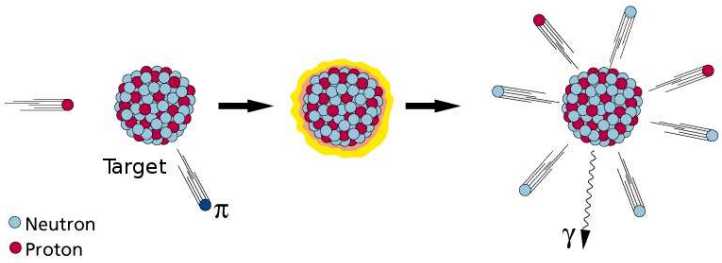

Figure C.1: Schematic illustration of a spallation process.

Spallation source is an accelerator-based neutron source that provides intense pulsed neutron beams. Neutrons are produced in the target by a process called spallation that is illustrated in Fig. C.1. At ISIS the neutrons are created by accelerating protons in a synchrotron, then colliding these with a heavy tungsten metal target. The tungsten target is bombarded with these pulses of high energy protons which drives neutrons from the nuclei of the target atoms. This gives an extremely intense neutron pulse, with only modest heat production in the neutron target. The neutrons are slowed to speeds useful for condensed matter research by an array of of hydrogenous moderators around the target. They are then directed to a suite of neutron instruments, each optimized to explore different properties of materials.

Bibliography

[1] P. L. Llewellyn, J.-P. Coulomb, Y. Grillet, J. Patarin, H. Lauter, H. Reichert, and J. Rouquerol. Adsorption by mfi-type zeolites examined by isothermal microcalorimetry and neurtron diffraction. 1. argon, krypton and methane. *Langmuir*, 9:1846, 1998.

[2] P. L. Llewellyn, J.-P. Coulomb, Y. Grillet, J. Patarin, H. Lauter, H. Reichert, and J. Rouquerol. Adsorption by mfi-type zeolites examined by isothermal microcalorimetry and neurtron diffraction. 1. nitrogen and carbon monoxide. *Langmuir*, 9:1852, 1998.

[3] V. Sánchez-Gil, Eva G. Noya, José María Guil, Enrique Lomba, and Susana Valencia. Adsorption of argon on pure silica mel. volumetric experiments and grand canonical monte carlo simulations. *Micropor. Mesopor. Mat.*, 222:218–225, 2016.

[4] Vicente Sánchez-Gil, Eva G. Noya, Alejandro Sanz, Sheima J. Khatib, José María Guil, Enrique Lomba, Ramona Marguta, and Susana Valencia. Stepped adsorption of toluene on pure silica mel zeolite. *J. Phys. Chem. C (submitted)*, 2015.

[5] V. Sánchez-Gil, E. G. Noya, and E. Lomba. Reverse monte carlo modeling in confined systems. *J. Chem. Phys.*, 140:024504, 2014.

[6] V. Sánchez-Gil, E. G. Noya, L. Temleitner, and L. Pusztai. Reverse monte carlo modeling: the two distinct routes to calculating the experimental structure factor. *J. Mol. Liq.*, 207:211, 2015.

[7] V. Sánchez-Gil, E. G. Noya, , José María Guil, Enrique Lomba, Susana Valencia, Iván da Silva, Laszlo Pusztai, and Laszlo Temleitner. Evidences of a structural change in pure-silica MEL upon the adsorption of argon. *J. Phys. Chem. C (submitted)*, 2015.

[8] Jiři Čejka, Avelino Corma, and Stacey Zones. *Zeolites and Catalysis: Synthesis, Reactions and Applications*. Wiley online library.

[9] Lev Sarkisov and Alex Harrison. Computational structure characterisation tools in application to ordered and disordered porous materials. *Molecular Simulation*, 37(15):1248–1257, 2011.

[10] D. H. Olson, G. T. Kokotailo, and S. L. Lawton. Crystal structure and structure-related properties of zsm-5. *J. Phys. Chem.*, 85:2238–2243, 1981.

[11] O. Terasaki, T. Ohsuna, H. Sakuma, D. Watanabe, Y. Nakagawa, and R. C. Medrud. Direct observation of pure mel type zeolite. *Chem. Mater.*, 8:463, 1996.

[12] C. Baelocher, L. McCusker, and D. H. Olson. *Atlas of Zeolite Framework types*. Elsevier, 2007.

[13] García-Pérez E., Parra J. B., Ania C., García-Sánchez A., van Baten J. M., Krishna R., Dubbeldam D., and S. Calero. A computational study of co2, n2, and ch4 adsorption in zeolites. *Adsorption*, 13:469–476, 2007.

[14] H. van Koningsveld, H. van Bekkum, and J. C. Jansen. On the location and disorder of the tetrapropylammonium (tpa) ion in zeolite zsm-5 with improved framework accuracy. *Acta Cryst.*, B43:127, 1987.

[15] H. van Koningsveld, J. C. Jansen, and H. van Bekkum. The monoclinic framework structure of zeolite h-zsm-5. comparison with the orthorhombic framework of as-synthesized zsm-5. *Zeolites*, 10:235, 1990.

[16] H. van Koningsveld, F. Tuinstra, H. van Bekkum, and J. C. Jansen. The location of p-xylene in a single crystal of zeolite h-zsm-5 with a new, sorbate-induced, orthorhombic framework symmetry. *Acta Cryst.*, B45:423 – 431, 1989.

[17] Nicholas Metropolis, Arianna W. Rosenbluth, Marshall N. Rosenbluth, Augusta H. Teller, and Edward Teller. Equation of state calculations by fast computing machines. *J. Chem. Phys.*, 21:1087, 1953.

[18] D. Frenkel and B. Smit. *Understanding Molecular Simulation. From Algorithms to Applications*. Academic Press, Boston, 1996.

[19] M.P. Allen and D.J. Tildesley. *Computer Simulation of Liquids*. Clarendon, Oxford, 1987.

[20] Randall Q. Snurr, Alexis T. Bell, and Doros N. Theodorou. Prediction of adsorption of aromatic hydrocarbons in silicalite from grand canonical monte carlo simulations with biased insertions. *J. Phys. Chem.*, 97:13742–13752, 1993.

[21] E. García-Pérez, J.B. Parra, C.O. Ania, D. Dubbeldam, T. Vlugt, J.M. Castillo, P.J. Merkling, and S. Calero. Unraveling the argon adsorption processes in mfi-type zeolite. *J.Phys. Chem. C*, 112:9976–9979, 2008.

[22] W. L. Jorgensen, E. R. Laird, T. B. Nguyen, and J. Tirado-Rives. Monte carlo simulations of pure liquid substitured benzenes with opls potential functions. *J. Comp. Chem*, 14:206, 1993.

[23] R. Q. Snurr, A. T. Bell, and D. N. Theodorou. Prediction of adsorption of aromatic hydrocarbons in silicalite from grand canonical monte carlo simulations with biased insertions. *J. Phys. Chem*, 97:13742, 1993.

[24] E. García-Pérez, J. B. Parra, C. O. Ania, D. Dubbeldam, T. J. H. Vlugt, J. M. Castillo, P. J. Merkling, and S. Calero. Unraveling the argon adsorption processes in mfi-type zeolite. *J. Phys. Chem. C*, 112:9976, 2008.

[25] P. Demontis, G. B. Suffritti, S. Quartieri, E. S. Fois, and A. Gamba. Molecular dynamics studies on zeolites. 3. dehydrated zeolite a. *J. Phys. Chem.*, 92:867–871, 1988.

[26] J. B. Nicholas, A. J. Hopfinger, F. R. Trouw, and L. E. Iton. Molecular modeling of zeolite structure. 2. structure and dynamics of silica sodalite and silicalite force field. *J. Am. Chem. Soc.*, 113:4792–4800, 1991.

[27] Ding-Yu Peng and Donald B. Robinson. A new two-constant equation of state. *Ind. Eng. Chem. Fundamen.*, 15:59–64, 1976.

[28] Otto Redlich and J. N. S. Kwong. On the thermodynamics of solutions. v. an equation of state. fugacities of gaseous solutions. *Chemical Reviews*, 44:233–244, 1949.

[29] K.A.M Gasem, W. Gao, Z. Pan, and R.L. Robinson Jr. A modified temperature dependence for the peng–robinson equation of state. *Fluid Phase Equilibria*, 181:113–125, 2001.

[30] Giorgio Soave. Equilibrium constants from a modified redkh-kwong equation of state. *Chemical Engineering Science*, 27:1197–1203., 1972.

[31] Fokion Karavias and Alan L. Myers. Isosteric heats of multicomponent adsorption: thermodynamics and computer simulations. *Langmuir*, 7:3118 – 3126, 1991.

[32] D. Nicholson and N. G. Parsonage. Computer simulation and the statistical mechanics of adsorption. *Academic Press*, 1982.

[33] N. W. Ashkroft and N. D. Mermin. *Solid State Physics*. Holt, Rinehart and Winston, 1976.

[34] Laszlo Mihaly and Michael C. Martin. *Solid State Physics*. Wiley, 2008.

[35] A. Mellergård and R. L. McGreevy. Reverse monte carlo modelling of neutron powder diffraction data. *Acta Crystallogr.*, A55:783, 1999.

[36] P. J. Brown, A. G. Fox, E. N. Maslen, M. A. O'Keefe, and B. T. M. Willis. Intensity of diffracted intensities. *International Tables for Crystallography*, C:554–595, 2006.

[37] Izabela M. Sosnowska. The birth of time-of-flight (tof) neutron powder diffraction at pulsed neutron source. *Cryst. Res. Technol.*, 50(9–10):705–715, 2015.

[38] Alex C. Hannon. Results on disordered materials from the general materials diffractometer, gem, at isis. *Nucl. Instrum. Methods Phys. Res. A*, 551:88–107, 2005.

[39] R. L. McGreevy and L. Pusztai. Reverse monte carlo simulation: A new technique for the determination of disordered structures. *Mol. Simul.*, 1:359, 1988.

[40] M. A. Howe, R.L. McGreevy, L. Pusztai, and I. Borzsák. Determination of 3 body correlations in simple liquids by rmc modelling of diffraction data. *Phys. Chem. Liq.*, 25:205–241, 1993.

[41] P. Jóvári, I. Kaban, J. Steiner, B. Beuneu, A. Schöps, and M. A. Webb. Local order in amorphous $Ge_2Sb_2Te_5$ and $GeSbTe_4$. *Phys. Rev. B*, 77:035202, 2008.

[42] D. A. Keen, S. Hull, W. Hayes, and N. J. G. Gardner. Structural evidence for a fast-ion transition in the high-pressure rocksalt phase of silver iodide. *Phys. Rev. Lett.*, 77:4914–17, 1996.

[43] O. Gereben. *RMC_POT user guide.*

[44] J.J. Olivero and R.L. Longbothum. Empirical fits to the voigt line width: A brief review. *Journal of. Journal of Quantitative Spectroscopy and Radiative Transfer*, 17:233–236, 1977.

[45] G. Caglioti, A. Paoletti, and F.P. Ricci. Choice of collimators for a crystal spectrometer for neutron diffraction. *Nuclear Instruments*, 3(4):223–228, 1958.

[46] R. B. Von Dreele, J. D. Jorgensen, and C. G. Windsor. Rietveld refinement with spallation neutron powder diffraction data. *J. Appl. Cryst.*, 15:581–589, 1982.

[47] R. L. McGreevy and L. Pusztai. Reverse monte carlo simulation: A new technique for the determination of disordered structures. *Mol. Simul.*, 1:359, 1988.

[48] R.L. McGreevy and L. Pusztai. The structure of molten salts. *Proc. Roy. Soc. London A*, 430:241–260, 1990.

[49] N. Veglio, F. J. Bermejo, L. C. Pardo, J. Ll. Tamarit, and G. J. Cuello. Direct experimental assessment of the strength of orientational correlations in polar liquids. *Phys. Rev. B*, 72:031502, 2005.

[50] Sz. Pothoczki, A. Ottochian, M. Rovira-Esteva, L. C. Pardo, J. Ll. Tamarit, and G. J. Cuello. Role of steric and electrostatic effects in the short-range order of quasitetrahedral molecular liquids. *Physical Review B*, 85:014202, 2012.

[51] L. Temleitner. Structure determination of liquid carbon tetrabromide via a combination of x-ray and neutron diffraction data and reverse monte carlo modeling. *Journal of Molecular Liquids*, 197:204–210, 2014.

[52] K. T. Wikfeldt, M. Leetmaa, M. P. Ljungberg, A. Nilsson, and L. G. M. Pettersson. On the range of water structure models compatible with x-ray and neutron diffraction data. *J. Phys. Chem. B*, 113:6246–6255, 2009.

[53] I. Harsányi and L. Pusztai. Hydration structure in concentrated aqueous lithium chloride solutions: A reverse monte carlo based combination of molecular dynamics simulations and diffraction data. *J. Chem. Phys.*, 137:204503, 2012.

[54] Ivan Kaban, Pál Jóvári, Mihai Stoica, Jürgen Eckert, Walter Hoyer, and Brigitte Beuneu. Topological and chemical ordering in $Co_{43}Fe_{20}Ta_{5.5}B_{31.5}$ metallic glass. *Phys. Rev. B*, 79:212201, 2009.

[55] P. Jóvári, I. Kaban, J. Steiner, B. Beuneu, A. Schöps, and A. Webb. 'wrong bonds' in sputtered amorphous $Ge_2Sb_2Te_5$. *J. Phys. Condens. Matter*, 19:335212, 2007.

[56] D. A. Keen, S. Hull, A. C. Barnes, P. Berastegui, W. A. Crichton, P. A. Madden, M. G. Tucker, and M. Wilson. The nature of the superionic transition in ag+ and cu+ halides. *Phys. Rev. B*, 68:014117, 2003.

[57] Sz. Pothoczki, L. Temleitner, L. C. Pardo, G. J. Cuello, M. Rovira-Esteva, and J. Ll. Tamarit. Comparison of the atomic level structure of the plastic crystalline and liquid phases of CBr_2Cl_2 : neutron diffraction and reverse Monte Carlo modelling. *Journal of Physics: Condensed Matter*, 25:454216, 2013.

[58] M. G. Tucker, M. T. Dove, and D. Keen. Application of the reverse monte carlo method to crystalline materials. *J. Appl. Crystallogr.*, 34:630–8, 2001.

[59] C. L. Farrow, P. Juhás, J. W. Liu, D. Bryndin, E. S. Božin, J. Bloch, Th. Proffen, and S. J. L. Billinge. Pdffit2 and pdfgui: computer programs for studying nanostructure in crystals. *J. Phys.: Condens. Matter*, 19:335219, 2007.

[60] O. Gereben, P. Jóvári, L. Temleitner, and L. Pusztai. A new version of the RMC++ Reverse Monte Carlo programme, aimed at investigating the structure of covalent glasses. *Journal of Optoelectronics and Advanced Materials*, 9:3021–3027, 2007.

[61] O. Gereben and L. Pusztai. Rmcpot: A computer code for reverse Monte Carlo modeling the structure of disordered systems containing molecules of arbitrary complexity. *J. Comp. Chem.*, 2285:33, 2012.

[62] M. T. Dove, M. G. Tucker, and D. A. Keen. Neutron total scattering method: simultaneous determination of long-range and short-range order in disordered materials. *Eur. J. Mineral.*, 14:331–348, 2002.

[63] P. L. Llewellyn, J. P. Coulomb, Y. Grillet, J. Patarin, H. Lauter, H. Reichert, and J. Rouquerol. Adsorption by mfi-type zeolites examined by isothermal microcalorimetry and neutron diffraction. 1. argon, krypton, and methane. *Langmuir*, 9:1846 – 1851, 1993.

[64] Berend Smit and Theo L. M. Maesen. Molecular simulations of zeolites: Adsorption, diffusion, and shape selectivity. *Chem. Rev.*, 108:4125–4184, 2008.

[65] A. Rahman. Correlations in the motion of atoms in liquid argon. *Phys. Rev.*, 136:A405, 1964.

[66] Bellisent-Funel, Chieux M. C., D. P., Levesque, and J. Weis, J. Structure factor and effective two-body potential for liquid gallium. *Phys. Rev. A*, 39:6310, 1989.

[67] P. Jóvári and L. Pusztai. Structure of disordered forms of selenium close to the melting point. *Phys. Rev. B*, 64:014205, 2001.

[68] O. Gereben and L. Pusztai. Structure of amorphous semiconductors: Reverse Monte Carlo studies on a-C, a-Si and a-Ge. *Phys. Rev. B*, 50:14136, 1994.

[69] Kenji Suzuki. Structural study of liquids with strong short-range correlation in the atomic distribution. *Berichte der Bunsen-Gesellschaft*, 80(8):689–694, 1976.

[70] S. Kugler, L. Pusztai, L. Rosta, R. Bellisent, and P. Chieux. The structure of evaporated pure amorphous silicon: Neutron diffraction and reverse monte carlo investigations. *Phys. Rev. B*, 48:7685, 1993.

[71] John A. White. Lennard-jones as a model for argon and test of extended renormalization group calculations. *J. Chem. Phys.*, 111:9352, 1999.

[72] J. L. Yarnell, M. J. Katz, R. G. Wenzel, and S. H. Koenig. Structure factor and radial distribution function for liquid argon at 85^{o}K. *Phys. Rev. A*, 7:2130, 1973.

[73] R. L. McGreevy. Reverse monte carlo modelling. *J. Phys.: Condens. Matter*, 13:R877–R913, 2001.

[74] G. Evrard and L. Pusztai. Reverse Monte Carlo modelling of the structure of disordered materials with RMC++ : a new implementation of the algorithm in C++ . *Journal of Physics: Condensed Matter*, 17:S1–S13, 2005.

[75] F. Sears. Neutron scattering llength and cross sections. *Neutron News*, 3(3):26–37, 1992.

[76] P. L. Llewellyn, J. P. Coulomb, Y. Grillet, J. Patarin, G. Andre, and J. Rouquerol. Adsorption by mfi-type zeolites examined by isothermal microcalorimetry and neutron diffraction. 2. nitrogen and carbon monoxide. *Langmuir*, 9:1852 – 1856, 1993.

[77] J. P. Coulomb, P. Llewellyn, Y. Grillet, and J. Rouquerol. Crystalline structure analysis by neutron diffraction of argon sorbed phases observed in the high loading regime of silicalite i and zsm-5 (si/al=23) zeolites. *Stud. Surf. Sci. Catal*, 87:535, 1994.

[78] N. Floquet, J. P. Coulomb, G. Weber, O. Bertrand, and J. P. Bellat. Structural signatures of type IV isotherm steps: Sorption of trichloroethene, tetrachloroethene and benzene in silicalite-I. *J. Phys. Chem. B*, 107:685, 2003.

[79] N. Floquet, J. P. Coulomb, J. P. Bellat, J. M. Simon, G. Weber, and G. Andre. Heptane adsorption in silicalite-1: neutron scattering investigation. *J. Phys. Chem. C*, 111:18182–18188, 2007.

[80] H. van Koningsveld, F. Tuinstra, H. van Bekkum, and J. C. Jansen. The location of the p-xylene in a single crystal of zeolite h-zsm-5 with a new sorbate-induced, orthorhombic framework symmetry. *Acta Cryst.*, B45:423, 1989.

[81] A. Mellergaard and R.L. McGreevy. Recent developments of the rmcpow method for structural modelling. *Chemical Physics*, 261:267 – 274, 2000.

[82] A Mellergård, R L McGreevy, A Wannberg, and B Trostell. Modelling of lattice and magnetic thermal disorder in manganese oxide. *J. Phys.: Condens. Matter*, 10:9401, 1998.

[83] S.J. Gregg and K.S. Sing. *Adsorption, Surface Area and Porosity*. Academic, London, 1982.

[84] Roland J.M. Pellenq and David Nicholson. Grand ensemble monte carlo simulation of simple molecules adsorbed in silicalite-1 zeolite. *Langmuir*, 11:1626 – 1635, 1995.

[85] R. L. McGreevy and L. Pusztai. Reverse monte carlo simulation: A new technique for the determination of disordered structures. *Mol. Simul.*, 1:359, 1988.

[86] Daan Frenkel and Berend Smit. *Undesrtanding Molecular Simulation*. Academic, London, 2002.

[87] R. L. McGreevy. Reverse monte carlo modelling. *J. Phys.: Condens. Matter*, 13:R887, 2001.

[88] M. D. Macedonia, D. D. Moore, E. J. Maginn, and M. M. Olken. *Langmuir*, 16:3823, 2000.

[89] R. Marguta, S.J. Khatib, J.M. Guil, E. Lomba, E.G. Noya, J.A. Perdigón-Melón, and S. Valencia. Molecular simulation and adsorption studies of n-hexane in zsm-11 zeolites. *Microporous and Mesoporous Materials*, 142:258 – 267, 2011.

[90] Per Zetterström, Sigita Urbonaite, Fredrik Lindberg, Robert G Delaplane, Jaan Leis, and Gunnar Svensson. Reverse monte carlo studies of nanoporous carbon from tic. *J. Phys.: Condens. Matter*, 17:3509–3524, 2005.

[91] N. A. Katcho, P. Zetterström, E. Lomba, J. F. Marco, E. Urones-Garrote, D. Avila-Brande, A. Gómez-Herrero, L. C. Otero-Díaz, and A. R. Landa-Cánovas. Structure of carbon nanospheres prepared by chlorination of cobaltocene: Experiment and modeling. *Phys. Rev. B*, 77:195402, 2008.

[92] U. Müller, H. Reichert, E. Robens, K. K. Unger, Y. Grillet, F. Rouquerol, J. Rouquerol, D. Pan, and A. Mermann. High-resolution sorption studies of argon and nitrogen on large crystals of microporous zeolite zsm-5. *Fresenius Z. Anal. Chem.*, 333:433, 1989.

[93] R. J.-M. Pellenq and D. Nicholson. Grand ensemble monte carlo simulation of simple molecules adsorbed in silicalite-1 zeolite. *Langmuir*, 95:1626, 1995.

[94] J. P. Coulomb, P. Llewellyn, Y. Grillet, and J. Rouquerol. Crystalline structure analysis by neutron diffraction of argon sorbed phases observed in the high loading regime of silicalite i and zsm-5 (si/al=23) zeolites. *Stud. Surf. Sci. Catal*, 87:535, 1994.

[95] D. Douguet, R. J.-M. Pellenq, A. Boutin, A. H. Fuchs, and D. Nicholson. The adsorption of argon and nitrogen in silicalite-1 zeolite: a grand canonical monte carlo study. *Mol. Sim.*, 17:1255, 1996.

[96] R. J.-M. Pellenq and D. Nicholson. Intermolecular potential function for the physical adsorption of rare gases in silicalite. *J. Phys. Chem.*, 98:13339, 1994.

[97] D. Nicholson and R. J.-M. Pellenq. Adsorption in zeolites: intermolecular interactions and computer simulation. *Adv. Coll. Inter. Sc.*, 76:179, 1998.

[98] C. A. Fyfe, H. Gies, G. T. Kokotailo, C. Pasztor, H. Strobl, and D. E. Cox. Detailed investigation of the lattice structure of zeolite zsm-11 by a combination of solid-state nmr and synchrotron x-ray diffraction techniques. *J. Am. Chem. Soc.*, 111:2470, 1989.

[99] C. A. Fyfe, Y. Feng, H. Grondey, G. T. Kokotailo, and A. Mar. Natural abudance, two-dimensional 29si mas nmr investigation of the three-dimensional bonding connectivities in the high and low tempèrature forms of zeolite zsm-11. *J. Phys. Chem.*, 95:3747, 1991.

[100] H. Gies, B. Marler, C. Fyfe, G. Kokotailo, Y. Feng, and D. E. Cox. The combination of synchrotron powder diffraction and high-resolution solid state nmr experiments. *J. Phys. Chem. Solids*, 52:1235, 1991.

[101] R. Marguta, S. J. Khatib, J. M. Guil, E. Lomba, E. G. Noya, J. A. Perdigón-Melón, and S. Valencia. Molecular simulation and adsorption studies of n-hexane in zsm-11 zeolites. *Micropor. Mesopor. Mat.*, 142:258, 2011.

[102] D. Dubbeldam, S. Calero, T. J. H. Vlugt, R. Krishna, T. L. M. Maesen, E. Beerdsen, and B. Smit. Force field parametrization through fitting of inflection points in isotherms. *Phys. Rev. Lett.*, 93:088302, 2004.

[103] G. J. Kramer, N. P. Farragher, B. W. van Beest, and R. A. van Santen. Interatomic force fields for silicas, aluminophosphates and zeolites: Derivation based on ab initio calculations. *Phys. Rev. B*, 43:5068, 1991.

[104] J. R. Hill and J. Sauer. Molecular mechanics potential for silica and zeolite catalysts based on ab-initio calculations. 2. aluminosilicates. *J. Phys. Chem.*, 99:9536, 1995.

[105] N. A. Ramsahye and R. G. Bell. Cation mobility and the sorption of chloroform in zeolite nay: molecular dynamics study. *J. Phys. Chem. B*, 109:4738–4747, 2005.

[106] A. Gabrieli, M. Sant, P. Demontis, and G. B. Suffritti. Development and optimization of a new force field for flexible aluminosilicates, enabling fast molecular dynamics simulations on parallel architectures. *J. Phys. Chem. C*, 117:503, 2013.

[107] M. Jeffroy, C. Nieto-Draghi, and A. Boutin. Molecular simulation of zeolite flexibility. *Mol. Sim.*, 40:6–15, 2014.

[108] R. Bueno-Pérez, S. Calero, D. Dubbeldam, C. O. Ania, J. B. Parra, A. P. Zaderenko, and P. J. Merkling. Zeolite force fields and experimental siliceous frameworks in a comparative infrared study. *J. Phys. Chem. C*, 116:25707–25805, 2012.

[109] P. Demontis, G. B. Suffritti, S. Quartieri, A. Gamba, and E. S. Fois. Molecular dynamics studies on zeolites. *J. Chem. Soc. Faraday Trans.*, 87:1657–1663, 1991.

[110] T. J. H. Vlugt and M. Schenk. Influence of framework flexibility on the adsorption properties of hydrocarbons in the zeolite silicalite. *J. Phys. Chem. B*, 106:12757–12763, 2002.

[111] A. García Sánchez, D. Dubbeldam, and S. Calero. Modeling adsorption and self-diffusion of methane in lta zeolites: The influence of framework flexibility. *J. Phys. Chem. C*, 114:15068, 2010.

[112] T. J. H. Vlugt, E. García-Pérez, D. Dubbeldam, S. Bam, and S. Calero. Computing the heat of adsorption using molecular simulations: The effect of strong coulombic interactions. *J. Chem. Theor. Comp.*, 4:1107, 2008.

[113] E. Maglara, A. Pullen, D. Sullivan, and W. C. Conner. Characterization of microporous solids by adsorption: measurement of high-resolution adsorption isotherms. *Langmuir*, 10:4167, 1994.

[114] L. E. First, C. E. Gounaris, J. Wei, and C. A. Floudas. Computational characterization of zeolite porous networks: an automated approach. *Phys. Chem. Chem. Phys.*, 13:17339, 2011.

[115] N. G. Almarza and E. Lomba. Determination of the interaction potential from the pair distribution function: an inverse monte carlo technique. *Phys. Rev. E*, 68:011202, 2003.

[116] J. P. Bellat, E. Lemaire, J. M. Simon, G. Weber, and A.-C. Dubreuil. Adsorption and coadsorption of 2-methylpentane and 2,2-dimethylbutane in a ZSM-5 zeolite. *Adsorption*, 11:109, 2005.

[117] R. Goyal, A. N. Fitch, and H. Jobic. Powder neutron and X-ray diffraction studies of benzene adsorbed in zeolite ZSM-5. *J. Phys. Chem. B*, 104:2878, 2000.

[118] H. M. Rietveld. A profile refinement method for nuclear and magnetic structures. *J. Appl. Crystallogr.*, 2:65, 1965.

[119] D. A. Keen, M. G. Tucker, and M. T. Dove. Reverse Monte Carlo modelling of crystalline disorder. *J. Phys.: Condens. Matter*, 17:S15, 2005.

[120] Matthew G. Tucker, David A. Keen, Martin T. Dove, Andrew L. Goodwin, and Qun Hui. Rmcprofile: reverse monte carlo for polycrystalline materials. *J. Phys.: Condens. Matter*, 19:335218, 2007.

[121] E. Lomba, C. Bores, V. Sánchez-Gil, and E. G. Noya. A three dimensional integral equation approach for fluids under confinement: Argon in zeolites. *J. Chem. Phys.*, 143:164703, 2015.

[122] L. Pusztai and R. L. McGreevy. Mcgr: An inverse method for deriving the pair correlation function. *J. Neutron Res.*, 8:17, 1999.

[123] Matthew G. Tucker, Martin T. Dove, and David A. Keen. Mcgrfot: Monte carlo g(r) with resolution corrections for time-of-flight neutron diffractometers. *J. Appl. Crystallogr.*, 34:780, 2001.

[124] J. D. Weeks, D. Chandler, and H. C. Andersen. Role of repulsive forces in determining the equilibrium structure of simple liquids. *J. Chem. Phys.*, 54:5237, 1971.

[125] B. Smit and T. L. M. Maesen. Molecular simulations of zeolites: Adsorption, diffusion, and shape selectivity. *Chem. Rev.*, 108:4125, 2008.

[126] L. B. McCusker, R. B. Von Dreele, D. E. Cox, D. Louër, and P. Scardi. Rietveld refinement guidelines. *J. Appl. Cryst.*, 32:36–50, 1999.

[127] David E. Clark. *Evolutionary Algorithms in Molecular Design*. John Wiley & Sons, Weinheim, Germany, 2000.

[128] B. H. Toby. R factors in Rietveld analysis: How good is good enough? *Powder Diffr.*, 21:67, 2006.

[129] D. Breck. *Zeolites Molecular Sieves*. John Wiley and Sons, Inc., New York, 1974.

[130] S. Kulprathipanja. *Zeolites in Industrial Separation and Catalysis*. Wiley-VCH, Weinheim, 2010.

[131] G. Paparatto, E. Moretti, G. Leofanti, and F. Gatti. Toluene ethylation on zsm zeolites. *J. Catal.*, 105:227–232, 1987.

[132] O. Talu, C.-J. Guo, and D. T. Hayhurst. Heterogeneous adsorption equilibria with comparable molecule and pore sizes. *J. Phys. Chem.*, 93:7294–7298, 1989.

[133] C. E. Webster, R. S. Drago, and M. C. Zerner. A method for characterizing effective pore sizes of catalysts. *J. Phys. Chem. B*, 103:1142–1249, 1999.

[134] J. M. Guil, R. Guil-López, J. A. Perdigón-Melón, and A. Corma. Determining the topology of zeolites by adsorption microcalorimetry of organic molecules. *Micropor. Mesopor. Mat.*, 22:269–279, 1998.

[135] D. H. Olson, G. T. Kokotailo, and S. L. Lawton. Crystal structure and structure-related properties of zsm-5. *J. Phys. Chem.*, 85:2238, 1981.

[136] B. F. Mentzen. Structural correlations between the framework symmetry of highly siliceous MFI zeolitic materials (silicalite, ZSM-5 for si/al¿75) and the location or the geometry ob sorbed molecules. *Mater. Res. Bull.*, 27:831, 1992.

[137] R. L. Portsmouth, M. J. Duer, and L. J. Gladden. ^{2}H NMR studies of single-component adsorption in silicalite: a comparative study of benzene and p-xylene. *J. Chem. Soc. Faraday Trans.*, 91:559–567, 1995.

[138] N. Floquet, J. P. Coulomb, G. Weber, O. Bertrand, and J. P. Bellat. Structural signatures of type IV isotherm steps: Sorption of trichloroethene, tetrachloroethene and benzene in silicalite-I. *J. Phys. Chem. B*, 107:685, 2003.

[139] C.-K. Lee and A. S. T. Chiang. Adsorption of aromatic compounds in large MFI zeolite crystals. *J. Chem. Soc.; Faraday Trans.*, 92:3445–3451, 1996.

[140] H. Thamm. Calorimetric study on the state of aromatic molecules sorbed on silicalite. *J. Phys. Chem.*, 91:8–11, 1987.

[141] R. Goyal, A. N. Fitch, and H. Jobic. Powder neutron and x-ray diffraction studies of benzene adsorbed in zeolite zsm-5. *J. Phys. Chem. B*, 104:2878–2884, 2000.

[142] F. Bosselet, M. Sacerdote, J. Bouix, and B. F. Mentzen. The MFI(ZSM-5)/sorbate systems. comparison between structural, theoretical and calorimetric reults. part i. the MFI/p-xylene system. *Mater. Res. Bull.*, 25:443, 1990.

[143] M. Sacerdote, F. Bosselet, and B. F. Mentzen. The MFI(ZSM-5)/sorbate systems. comparison between structural, theoretical and calorimetric reults. part ii. the MFI/benzene system. *Mater. Res. Bull.*, 25:593, 1990.

[144] R. Q. Snurr, A. T. Bell, and D. N. Theodorou. Molecular simulations of low occupancy adsorption of aromatics in silicalite. In R. van Ballmoos, J. B. Higgins, and M. M. J. Butterworth-Heinemann, editors, *Proceedings from the Ninth International Zeolite Conference, Montreal 1992*, volume II, pages 71–78, Boston, 1993.

[145] R. Q. Snurr, A. T. Bell, and D. N. Theodorou. A hierarchical atomistic/lattice simulation approach for the prediction of adsorption thermodynamics of benzene in silicalite. *J. Phys. Chem.*, 98:5111–5119, 1994.

[146] R. E. Richards and L. V. C. Rees. The sroption of p-xylene in zsm-5. *Zeolites*, 8:35, 1988.

[147] C. G. Pope. Sorption of benzene, toluene and p-xylene on silicalite and H-ZSM-5. *J. Phys. Chem.*, 90:835–837, 1986.

[148] R. L. McGreevy. Reverse monte carlo modelling. *J. Phys.: Condens. Matter*, 13:R887, 2001.

[149] J. M. Guil, A. Pérez Masiá, A. Ruiz Paniego, and J. M. Trejo Menayo. Energetics of H_2 and O_2 adsorption on Irγ-Al_2O_3 and Ir/SiO_2 catalysts. dependence on support and on metal particle size. *Thermochim. Acta*, 312:115, 1998.

[150] J. M. Guil, A. Pérez Masiá, A. Ruiz Paniego, and J. M. Trejo Menayo. Enthalpies of adsorption and hydrocarbons on discandium trioxide determined by calorimetrically and from adsorption isotherms. *J. Chem. Thermodyn.*, 26:5, 1994.

[151] P. D. Kolokathis, E. Pantatosaki, C.-A. Gatsiou, H. Jobic, G. K. Papadopoulos, and D. N. Theodorou. Dimensionality reduction of free energy profiles of benzene in silicalite-1: calculation of diffusion coefficients using transition state theory. *Mol. Sim.*, 40:80–100, 2014.

[152] D. Dubbeldam, D. Calero, T. J. H. Vlugt, R. Krishna, T. L. M. Maesen, E. Beerdsen, and B. Smit. Force field parametrization through fitting on inflection points in isotherms. *Phys. Rev. Lett.*, 93:088302, 2004.

[153] *Materials Studio, version 5.0.0.0.* Accelrys Software Inc.: San Diego, CA, 2009.

[154] W. S. Lovesey, editor. *Theory of Neutron Scattering from Condensed Matter.* Oxford science publications, 1987.